TECHNICAL MEMORANDUM

638

ECMWF study on the impact of future developments of the space-based observing system on Numerical Weather Prediction

Gábor Radnóti, Peter Bauer, Anthony McNally, Carla Cardinali, Sean Healy and Patricia de Rosnay

Research Department

December 2, 2010

European Centre for Medium-Range Weather Forecasts
Europäisches Zentrum für mittelfristige Wettervorhersage
Centre européen pour les prévisions météorologiques à moyen terme

Series: ECMWF Technical Memoranda

A full list of ECMWF Publications can be found on our web site under:
http://www.ecmwf.int/publications/

Contact: library@ecmwf.int

European Centre for Medium-Range Weather Forecasts
Shinfield Park, Reading, RG2 9AX, England

Abstract

The subject of this study is the evaluation of the impact of the key components of the space-based observing system on the skill of numerical weather prediction. The main emphasis is put on temperature and humidity sounding from advanced sounders of the AIRS/IASI-type and conventional sounders of the HIRS/AMSU-A/MHS-type, humidity imaging in clear skies and in areas affected by clouds and precipitation, radio-occultation observations to support the estimation of the observation requirements of a radio-occultation observation constellation for the next decade, indirect wind observations (through AMVs) with special focus on polar AMVs and finally new observation types, in particular soil moisture derived from scatterometry (ASCAT). Observations related to clouds and precipitation, in support of radio-occultation constellation definition, and related to soil moisture have never been evaluated in a comparable framework before. The new diagnostic tools of observational influence in the analysis (OIA) and forecast error contribution (FEC) are also applied in this study to complete the findings deriving from the OSEs.

Contents

1 Executive summary

The subject of this study is the evaluation of the impact of the key components of the space-based observing system on the skill of numerical weather prediction. The skill of NWP depends to a large extent on the quality of the analysis state that serves to initialize the forecast model. At ECMWF and most operational centres this analysis is performed via a four-dimensional variational assimilation (4D-Var) scheme that produces a physically consistent estimate of the state of surface and atmosphere. This estimate is constrained by both the forecast model and observations. The large improvement of NWP skill obtained over the past two decades can be attributed to model developments and the increased capability of the space-based observation component along with sophisticated data assimilation systems that derive the analysis state from model forecasts and data.

The specific objectives of the present study are thus to estimate the impact of the key components of the current space-based observing system with a special focus on (1) temperature and humidity sounding from advanced sounders of the AIRS/IASI-type and conventional sounders of the HIRS/AMSU-A/MHS-type, (2) humidity imaging in clear skies and in areas affected by clouds and precipitation, (3) radio-occultation observations to support the estimation of the observation requirements of a radio-occultation observation constellation for the next decade, (4) indirect wind observations (through AMVs) with special focus on polar AMVs and (5) new observation types, in particular soil moisture derived from scatterometry (ASCAT).

Observations related to clouds and precipitation, in support of radio-occultation constellation definition, and related to soil moisture have never been evaluated in a comparable framework before. Another evaluation of the value of advanced infrared sounders is due given the recent improvements of their data usage in NWP (water vapour channels, cloud detection, usage over land).

Sounders in clear skies

The impact of *conventional sounders*, namely AMSU-A, HIRS and MHS is strong and significantly positive when evaluated by the fit of model analyses and short-range forecasts to all observations contained in the system and when analyzing forecast scores. The individual impact of HIRS is much smaller compared to that of the two microwave sounders given that the background observing system contains two advanced sounders, namely AIRS and IASI. The positive impact of microwave sounders on temperature and geopotential forecast skill is especially evident in the Southern hemisphere and visible throughout the entire atmosphere. The positive impact is significant up to 4 days in the Southern hemisphere and up to 2 days in the Northern hemisphere. One area of seemingly negative impact (over South America) requires further investigation but could be the result of insufficient cloud detection or inaccurate surface emissivity modeling.

The situation is similar for humidity scores. Over oceans the presence of AMSU-A/MHS data seems to slightly but systematically moisten the analysis, while over land the opposite effect is observed. This is mainly caused by the MHS radiance assimilation. This impact is in agreement with what has been observed from the radiosonde humidity departures in the analyses, that are mostly located over land surfaces, and the comparison of model analyses and short-range forecasts with IASI radiances (water vapour channels) that are only used over oceans.

The impact of *advanced sounders* (AIRS and IASI) used either separately or together is significant and has been tested over an extended one year test period. The benefit of adding these instruments to a baseline can be seen in the improved fit of the analysis to conventional observations and a reduction of

forecast errors out to the medium-range. Degraded forecasts result when the instruments are withheld, although the presence of one sounder is partially able to compensate for the loss of the other. These studies confirm and consolidate other impact experiments (performed at ECMWF and other centres) which collectively demonstrate that the information brought by advanced infrared sounders is crucial.

The one anomalous result that requires further investigation is the poor impact of IASI upon medium-range forecasts over the European region. In experiments where IASI was added to a background observing system the performance was only neutral whiles the removal of IASI from the full system actually reduced forecast errors. In contrast, results for AIRS over Europe were positive in both contexts. From the analysis diagnostics the only obvious difference between AIRS and IASI is in low-level temperatures (and humidity) at high northern latitudes and the enhanced large-scale north-south gradient (possibly responsible for the degraded fit to high latitude radiosonde wind data). However, investigations performed so far have been unable to confirm that this is in any way responsible for the degraded European forecasts. It should be noted that a poor performance over Europe was not evident in any of the pre-operational tests that were carried out on IASI in the past (indeed European scores were significantly improved when IASI was first used). The understanding of this problem remains a priority. The contradicting results from adding and removing IASI indicate the non-linear response of the system to the presence/absence of data and the importance of the verifying analysis.

Sounders/imagers in clouds and precipitation

The assimilation of *all-sky radiances from microwave imagers* over oceans is found to systematically change the mean state of moisture over oceans. This change produces a better fit of analyses and short-range forecasts with other moisture sensitive radiances over oceans and also causes less general radiance data rejection. The impact of SSM/I data on boundary layer temperature and humidity is stronger than that of AMSU-A/MHS or HIRS, especially over the Tropics. Forecast verification of moisture instrument impacts strongly depends on the verifying analysis. In this case, the operational analysis that is used as a reference also contains all-sky microwave imager data and may thus produce favourable results. However, a positive impact was found for temperature, moisture and wind that lasts for a few days but dissipates faster than the forecast impact obtained from temperature sensitive data that affect larger scale structures. The assimilation of *cloud-affected infrared radiances* was shown to systematically affect temperatures in areas of overcast cloud regimes. While the impact of this on forecasts is small, the regional temperature analysis has been improved. This result is quite significant because, generally, much less radiance data is used in the presence of clouds, and this impact is caused by adding only 5% of sounder data.

Adjoint diagnostic techniques demonstrate that a substantial fraction of the observational influence in the analysis is driven by the variability of the model background error distribution as well as the model's sensitivity to perturbations of the particular observation. This is, for example, evident when infrared channels sensitive to both surface and clouds are evaluated where the contribution of large skin temperature background errors over sea-ice produce significant contributions to the observational influence in the analysis as does the model's sensitivity to radiance perturbations in the presence of clouds in the ITCZ. Due to the small number of infrared radiance observations actively used in clouds the forecast impact, as obtained from the forecast sensitivity calculations, is small which is consistent with the results of the observing system experiments. The analysis and forecast impact of microwave all-sky radiances is stronger as indicated by the adjoint measures. Interestingly, the impact on the analysis is mostly driven by clear-sky observations while the forecast impact is dominated by cloud-affected observations. This demonstrates the strong impact of the model and its sensitivity to information in areas where background

errors are large and the model is rather sensitive to temperature and moisture information.

Atmospheric Motion Vectors

The impact of *AMV observations* has been tested in a more fundamental way than that of the other observation types because the main objective has been to evaluate the impact of AMVs on the wind analysis in comparison to that of radiance observations in polar areas. The latter produce an impact on the wind analysis through the coupling of observation operator, balance constraints and the NWP model in 4D-Var. This study complements a previous effort performed for both AMV and CSR data usage at mid and lower latitudes derived from geostationary satellites. The experiments in the present study demonstrate that AMVs in polar areas produce a similar impact to infrared radiance observations (HIRS) if only water vapour channels are used while adding temperature sensitive radiances produces a stronger impact than AMVs. The experiments showed a significant difference of the results between North and South Poles, mainly caused by the largely different quality control applied to radiance data over the Antarctic continent due to high surface elevations.

In contrast to the experiments with geostationary data the heights of largest impact were quite similar over the poles while over lower latitudes the radiance impact was strongest at mid-levels and the CSRs acted most efficiently at low and high levels at which usually more data is assimilated. Adding radiance data and AMVs together showed an additional improvement that was more pronounced at Northern high latitudes. It must be kept in mind that, among all employed observations, both AMVs and HIRS-type radiance data do not represent the strongest information contribution in the analysis so that the above described results may be insignificant if a full satellite observing system is available.

Radio occultation

GPSRO data represent a substantial part of the observing system since they do not require bias correction and produce accurate observations of (mainly) temperature with very good vertical resolution in the upper atmosphere where radiance data is more sparse and NWP model errors are large. For the experiments in this study, data in addition to the currently assimilated receivers onboard METOP GRAS and the Formosat-COSMIC constellation have been acquired to make available as many GPSRO observations as possible. All data have been assimilated and three denial experiments have been run using only 5, 33 and 67% of the GPSRO data, respectively. The 5% experiment (i.e. about 150 profiles) is representative of the data numbers from a single receiving instrument.

The results from the 5% experiment indicate that the impact on temperature analysis is significant but not yet sufficient to remove the entire upper atmospheric temperature bias. Gradually increasing the number of observations further corrects the problem but the analysis fits to radiosonde observations clearly indicate that more observations will produce benefit. The radiosonde fits also suggest that the impact has a vertical structure, namely that GPSRO data warm the analysis in the stratosphere and cool it in the troposphere.

Due to the hydrostatic relationship GPSRO data do not only constrain the temperature profile of the analysis, but simultaneously the surface pressure as well. This has been tested by removing conventional surface pressure observations but assimilating GPSRO data. The presence of GPSRO data removes half of the surface pressure bias originating from removing surface pressure observations when verified against both buoy and SYNOP surface pressure observations. The error standard deviations are also 2-10% smaller when GPSRO data are present both in the first-guess and the analysis.

RMS temperature forecast errors and geopotential height anomaly correlations are positively affected by GPSRO data, especially in the higher atmosphere. Above 200 hPa the impact remains visible even for 7 days. A surprising negative effect is found, however, at 1000 hPa, especially over the Tropics for temperature. This degradation is very likely a model bias issue and is in agreement with what has been seen in boundary layer radiosonde statistics.

Finally, experiments have been run to compare the impact of IASI radiance data with that of GPSRO observations. Up to 500 hPa the IASI impact is clearly stronger, At 200 hPa over the Southern hemisphere IASI and GPSRO seem to be of equal impact. Over the Tropics GPSRO appears to bring slightly more improvement than IASI. Over the Northern hemisphere and in the first two days GPSRO data improves the forecast slightly more, but afterwards the IASI impact becomes much stronger. These results have to be viewed keeping in mind that about one order of magnitude more radiances than bending angles are assimilated at ECMWF.

Soil moisture

ASCAT soil moisture impact experiments have been run for an entire year over the period 01/12/2008 to 30/11/2009 at reduced model resolution. The experiments employed the recently developed Simplified Extended Kalman Filter scheme for the point-wise analysis of soil moisture. Mean low level humidity and temperature analysis fields are affected by ASCAT soil moisture data over continental areas. The biggest systematic impact can be found near the Amazon basin, but the African continent and the Northern parts of Asia and North-America also show large changes of the mean analysis state.

Forecast scores have been calculated verifying the ASCAT assimilation experiment and its control with the respective own analyses. From this, slightly positive forecast impact is derived over most continental areas. If near surface temperature forecasts are verified against radiosonde observations, a small negative impact of the ASCAT soil moisture assimilation can be identified over some continental areas that needs to be further investigated. Verification against SYNOP data and in situ soil moisture measurements show no significant impact.

Additional diagnostics

The new diagnostic tools of observational influence in the analysis (OIA) and forecast error contribution (FEC) have been applied for the control experiment of the OSE and to some denial experiments. The so obtained information is supplementary to what can be found by comparing different denial experiments. According to the diagnostics, in total IASI, AIRS and AMSU-A radiances contribute the most to the forecast quality improvement measured by the energy norm difference of forecast and verifying analysis (= forecast error) and these are followed by the conventional radio-sonde and aircraft observations. To visualize the geographical distribution of analysis and forecast impact of different sensors of sounders, three channels (one mid-tropospheric, one lower stratospheric temperature channel and one upper tropospheric humidity channel for each sensor) have been selected. The mean FEC and OIA show maximum areas of impact near the South-Pole and especially over the Inter-Tropical Convergence Zone. The high mean OIA values are accompanied with large spatial variability and they can be interpreted only in an average sense. The comparison of observation influence with background and analysis departure statistics indicates that systematic differences between model and observations result in high sensitivity values at the same location.

Acronyms

AIRS	Atmospheric Infrared Sounder
AMSR-E	Advanced Scanning Microwave Radiometer - E
AMSU	Advanced Microwave Sounding Unit
AMV	Atmospheric Motion Vector
ASCAT	Advanced SCATterometer
AVHRR	Advanced Very High Resolution Radiometer
CHAMP	Challenging Minisatellite Payload for Geophysical Research and Application
COSMIC	Constellation Observing System for Meteorology, Ionosphere and Climate
CSR	Clear-sky radiance
CrIS	Cross-track Infrared Sounder
DMSP	Defense Meteorological Satellite Program
ECMWF	European Centre for Medium-Range Weather Forecasts
EOS	Earth Observing System
EPS	EUMETSAT Polar System
EUCOS	EUMETNET Composite Observing System
EUMETNET	Network of European Meteorological Services
EUMETSAT	European Organisation for the Exploitation of Meteorological Satellites
FEC	Forecast Sensitivity to Observations
GNSS	Global Navigation Satellite Systems
GOME-2	Global Ozone Monitoring Experiment - 2
GPS	Global Positioning System
GPSRO	GPS Radio Occultation
GRACE-A	Gravity Recovery And Climate Experiment - A
GRAS	GNSS Receiver for Atmospheric Sounding
HIES	High Resolution Infrared Radiation Sounder
IASI	Infrared Atmospheric Sounding Interferometer
MHS	Microwave Humidity Sounder
MODIS	Moderate Resolution Imaging Spectroradiometer
NASA	National Aeronautics and Space Administration
NOAA	National Oceanic and Atmospheric Administration
NPOESS	National Polar-orbiting Operational Environmental Satellite System
NPP	NPOESS Preparatory Project
NWP	Numerical Weather Prediction
OMI	Ozone Monitoring Instrument
OSE	Observing System Experiment
OSSE	Observing System Simulation Experiment
RTTOV	Radiative Transfer for TOVS
SBUV	Solar Backscattered Ultra-Violet radiometer
SCIAMACHY	SCanning Imaging Absorption SpectroMeter for Atmospheric CHartographY
SSM/I	Special Sensor Microwave / Imager
OIA	Self-sensitivity to Observations
TOVS	TIROS Operational Vertical Sounder
TRMM	Tropical Rainfall Measuring Mission

2 Background

The subject of this study is the evaluation of the impact of the key components of the space-based observing system on the skill of numerical weather prediction. The skill of NWP depends to a large extent on the quality of the analysis state that serves to initialize the forecast model. At ECMWF and most operational centres this is performed via a four-dimensional variational assimilation (4D-Var) scheme that produces a physically consistent estimate of the state of surface and atmosphere. This estimate is constrained by both the forecast model and observations. The large improvement of NWP skill obtained over the past two decades can be attributed to model developments and the increased capability of the space-based observation component along with sophisticated data assimilation systems that derive the analysis state from model forecasts and data.

Previous space-based observation impact studies estimated the contribution of satellite data to NWP skill as 2-3 days in the Southern and 1/2 days in the Northern hemisphere (Kelly and Thépaut 2007). This estimation was based on Observing System Experiments (OSE) in which all space-based observations were withdrawn from the currently existing observing system and the detrimental effect on bulk forecast scores was quantified.

Apart from general impact studies, OSEs are well suited for estimating the impact of the loss of individual satellite mission (components). This is crucial for future mission planning and re-launch scenario definition in case of instrument failures or the total loss of a satellite. A study of this type has been recently performed by ECMWF (Bauer and Radnóti 2009, hereafter BR09) in the context of the EPS whose first satellite, Metop-A, has been successfully launched in 2006 and is fully operable until today.

OSE studies require continuous updating for several reasons: Both the modeling/data assimilation system and the actively used satellite observations develop over time and produce more skilful analyses and better forecasts. The relative value of individual components of the observing system therefore changes and must be re-evaluated. Secondly, new observation types are introduced either due to the launch of new instruments or due to the better handling of satellite data in the NWP systems that, for example, allows introducing a previously unused observation. Examples for the latter are the assimilation of cloud and precipitation affected infrared and microwave radiance observations or the availability of soil moisture products from satellite data. Thirdly, the OSE framework allows testing alternative satellite products in an operational environment for obtaining guidance for product development performed by space agencies. Lastly, the experimentation experience also teaches valuable lessons that require updating the future experimentation and evaluation approach.

3 Study objectives and approach

ECMWF has a rather comprehensive history of observing system experimentation since all new developments are usually tested along these lines prior to their operational implementation. More systematic studies have been performed in the past to support community-wide research and development. The present study, however, does not aim at a plain repetition of the previous exercise with a more modern analysis system but rather at the identification of specific areas where recent improvements have been achieved, where new, and so far less tested observations have become available and where dedicated support for future mission planning is required.

The specific objectives of the present study are thus to estimate the impact of the key components of the current space-based observing system with a special focus on:

1. Temperature and humidity soundings from (a) advanced sounders of the AIRS/IASI-type as they constitute a major part of the observations that are crucial for NWP; (b) conventional sounders of the HIRS/AMSU-A/MHS-type as they prove to provide observing systems that are complementary to advanced sounders.

2. Humidity imaging in (a) clear skies and (b) in areas affected by clouds and precipitation.

3. Radio-occultation observations to support the estimation of the observation requirements of a radio-occultation observation constellation for the next decade.

4. Indirect wind observations (through AMVs) with special focus on polar AMVs obtained from AVHRR data with AMV height assignment upgrades provided by advanced sounder data.

5. New observation types and products, in particular soil moisture derived from scatterometry (ASCAT).

Observations related to clouds and precipitation in item (2), in support of radio-occultation constellation definition in item (3), related to polar-orbiting AMV with alternative height assignment (4) and related to soil moisture in item (5) have never been evaluated in a comparable OSE framework before. Item (1) represents a further evaluation of the value of advanced infrared sounders given the recent improvements of their data usage in NWP (water vapour channels, cloud detection, usage over land) as well as of the basic satellite sounder system. Here, a special focus will be set on advanced diagnostics that have not been available in previous studies and that are expected to provide more detailed and complementary information on individual instrument impact. The radio-occultation mission constellation aspect covered in item (3) represents a special case because the experiments provides crucial information on the required number of occultation observations in support of future mission planning.

The analysis/forecast impact has been evaluated with standard metrics used in NWP as well as, for selected cases, with advanced diagnostics based on adjoint modeling. The latter are part of recent developments in data assimilation at ECMWF and have not been used in a systematic fashion before. Details of the proposed work and the study planning are described in the following sections.

4 Configuration

4.1 Model set-up

The experiments have been run with model cycles CY35R3 and CY36R1 of the Integrated Forecasting System (IFS) that became operational at ECMWF on 2009/09/08 and 2010/01/26, respectively. This choice ensured that the latest upgrades to model physics, data assimilation and observation treatment were incorporated in the OSEs. The experiments have been run at reduced horizontal resolution, namely for the forecast model with a T511 wavenumber truncation (40 km, compared to operational resolution of T799 i.e. 25 km and most recently T1279 i.e. 16 km). Based on the findings of BR09 the vertical resolution of the experiments has been kept at 91 levels with model top level pressure at 0.01 hPa, just like in operations. From previous OSEs, this reduced resolution was shown to produce sufficiently accurate results.

The system has been run in the global 4D-Var configuration that produces two analyses per day (00 and 12 UTC) with 12-hour assimilation windows (delayed cut-off data assimilation, DCDA; Haseler 2004). Only one medium-range forecast has been run per day as opposed to two forecasts in the operational

configuration. Despite different data coverage in the 00 and 12 UTC window, this is not expected to have affected the results and it provides sufficient statistical significance from the results.

The main experimentation periods for the sounder and microwave imager data are May-December 2009, for AMV data July-September 2009, for radio-occultation data July-September 2008, the latter having been chosen because of the additional experimental GPSRO data available for this period. For ASCAT soil moisture data the whole year of 2009 is used at a further reduced T255 (80 km) horizontal resolution. The latter avoids small-scale noise and permitted to run the experiment for an entire year.

All experiments have been initialized with the operational suite on the first day of the respective period. A 14-day spin-up phase was included allowing for the system to adjust to the modified observing system that was activated on day-1 in each case. It is expected that by the end of the spin-up period, the system has lost memory of the full system used to initialize the analysis on day-1. The experiment evaluation has been restricted to the remaining part of each period. The evaluation has been performed based on standard observation consistency statistics and standard forecast skill scores for key parameters (geopotential heights, temperatures, vector wind at 1000, 500, 200 hPa; global and regional) including tests of statistical significance. Additional evaluation has been performed using the diagnostic tools of analysis sensitivity to observations (Cardinali et al. 2004) and forecast error sensitivity to observations (Cardinali, 2009).

The variational bias-correction (Dee 2005, Auligné et al. 2007) for the experimentation period was initialized with the operational system output on the initial date and left active throughout the experimentation periods. This ensured that, as in the operational system, a trade-off between analysis and bias increments as a function of model state is performed.

4.2 Definition of impact evaluation

The evaluation of analyses is usually performed with all used observations assuming that better analyses will produce a generally and consistently better fit of the model fields when compared to observations. This comparison is performed for both analysis and first-guess, i.e. the short-range forecast that produces a first estimate of the actual state and that has been initialized from the previous analysis. The comparison is performed against all conventional and satellite observations and therefore uses the same observation operators (interpolation scheme, radiative transfer model) as the data assimilation scheme. This method is very stable and generally considered unambiguous.

Forecast evaluation is more difficult because different reference standards can produce rather different results. BR09 have shown that the evaluation with the experiment's own analysis or the operational analysis could produce inconsistent results, in some cases with opposite signs. The argument for using the experiment's own analyses for evaluation is that if an additional observation is expected to change the mean analysis state, only the own analysis provides a fair reference while any other would represent a poorer analysis state. This, however, can also produce problems in case of a sub-optimal observing system and simply due to the fact that additional observations can add systematically larger increments to the analysis and therefore increase the root-mean-square difference between (short-range) forecasts and analyses. Standard forecast evaluation in this study is performed with the operational analyses. The operational observing system contains more data in the above experimentation periods since the background system in the experiments was designed to represent conditions expected in the forthcoming ten years. Additionally, the operational system is run at higher spatial resolution. Wherever possible, forecast verification using radiosonde observations has been added.

Forecast scores or analysis statistics are often evaluated in this study as difference curves or difference

fields. The standard for all these difference plots is Experiment - Reference, unless stated otherwise.

A significant additional feature with respect to the BR09 study is the extension of the experiment evaluation by two other tools: observational influence in the analysis (OIA; Cardinali et al, 2004) and forecast error contribution of the observations (FEC; Cardinali, 2009). Both employ the model and observation operator adjoint models and are often referred to as adjoint-based diagnostic tools.

OIA is a quantity that allows the assessment of each observation contribution to the analysis and it measures the observational influence in the data assimilation scheme as a function of observation and background errors as well as the observation/model operator sensitivity. The quantity represented by OIA is the change of analysis value projected into observation space by the operator due to a unit change of the given observation. It is a square matrix in observation space and its diagonal contains the OIA that quantifies the impact of the unit change of an observation on its own analysis counterpart.

The value of OIA is expected to be between 0 and 1, where OIA=0 means that the observation has no influence and OIA=1 means that the analysis at the given point is fully driven by that observation. The actual calculation is performed by a numerical approximation so that values outside this range can occur. It has to be noted that OIA is only a sensitivity measure and that it does not quantify the impact of the observation on the quality of the analysis or forecast.

FEC is the forecast error sensitivity with respect to observations. Here, forecast error is defined by a scalar function (dry total energy norm) that measures the ”distance” of a forecast from our best knowledge of the truth, assumed to be the operational analysis. The function’s derivatives with respect to analysis variables and, through the Kalman gain matrix, with respect to observations can be mathematically derived. This forecast error sensitivity vector is multiplied by the actual background departures and provides an estimate of the forecast error reduction given the actual analysis due to the all used observations. Negative FEC indicate an observation’s contribution to forecast error reduction and vice versa.

Obviously, OIA and FEC can provide complementary information to an OSE-type analysis/forecast impact assessment. There are, however, fundamental differences:

- The adjoint-based observation sensitivity techniques measure the impact of observations when the entire observation set is present in the assimilation system, while the observing system is, in the context of OSE, modified. In fact, each OSE experiment differs from the others in terms of assimilated observations.
- The adjoint-based observation sensitivity techniques measure the response of a single forecast metric to all perturbations of the observing system, while the OSE measures the effect of a single perturbation (i.e. withdrawn observations) on all forecast metrics.
- The adjoint-based techniques are restricted by the tangent linear assumption, valid up to approximately 3 days. Furthermore, a simplified adjoint model is usually used to trace the forecast error information backwards towards the analysis. This further limits the validity of the linearity assumption, and therefore restricts the use of the diagnostics to a typical forecast range of 24-48 hours. One consequence of using a simplified adjoint model is that the analysis uncertainties obtained through the adjoint integration can be incorrect if the back-propagated signal is small. The OSE on the other hand can measure data impact on the long-range forecast but always suffers from the relativity of forecast verification with analyses (see BR09).
- The adjoint-based observation sensitivity techniques measure the impact of all observations assimilated at a single analysis time while the OSE also includes the effect of observations assimilated

Table 1: Current satellite radiance observing system used at ECMWF (status March 2009, monitored instruments in italic. Comments: [1] unstable, [2] except channels 6, 11, 14, [3] insufficient data quality, [4] except channels 5-7, 8, [5] instrument failed, [6] except channel 7, [7] except channel 3, [8] except channels 1-4, 11-12).

Sounders	HIRS	AMSU-A	AMSU-B/MHS	Advanced Sounders
NOAA-15 (am)	No [1]	Yes [2]	No [3]	N/A
NOAA-16 (pm)	No [1]	Yes [4]	Yes	N/A
NOAA-17 (am)	Yes	No [5]	Yes	N/A
NOAA-18 (pm)	No [1]	Yes	Yes	N/A
NOAA-19 (pm)	*Yes*	*Yes*	*Yes*	N/A
AQUA (pm)	N/A	Yes [6]	N/A	Yes (AIRS)
METOP-A (am)	Yes	Yes [6]	Yes	Yes (IASI)

Imagers	SSM/I	SSMIS	AMSR-E	TMI	Windsat
DMSP F-13 (am)	Yes	N/A	N/A	N/A	N/A
DMSP F-14 (am)	No [5]	N/A	N/A	N/A	N/A
DMSP F-15 (am)	Yes [7]	N/A	N/A	N/A	N/A
DMSP F-16 (am)	N/A	*Yes*	N/A	N/A	N/A
DMSP F-17 (am)	N/A	*Yes*	N/A	N/A	N/A
AQUA (pm)	N/A	N/A	Yes [8]	N/A	N/A
TRMM	N/A	N/A	N/A	*Yes*	N/A
Coriolis (am)	N/A	N/A	N/A	N/A	*Yes*

in previous cycles.

4.3 Background observing system

Since in this study the individual experiments target very specific components, both experiment set-up and evaluation tools are expected to vary. In most cases, however, it is expected to assume a background observing system that mimics the system to be available for the next ten years. A similar assumption has been made by BR09 but, given the fact that experiment periods changed, individual components of this study's background system have changed as well.

Examples for recent ECMWF observing system upgrades are the recent launch of NOAA-19 making available another set of conventional sounders (HIRS, AMSU-A, MHS), the failure of METOP AMSU-A channel 7, the additional use of METOP-A IASI water vapour channels and a revised cloud detection, the introduction of overcast cloud-affected data from infrared sounders, the introduction of the all-sky system for microwave imagers, large improvements to the HIRS cloud detection, the more accurate usage of AMSU-A observations over land surfaces, the extension of radio-occultation data usage up to 50 km, and the employment of a new radiative transfer model (RTTOV-9) that produces significantly improved radiance simulations. This had to be seen in view of other modifications related to model physics, numerics and data assimilation.

The present radiance observing system is compiled in Table 1. In addition to radiances, CSR and AMV products are assimilated from Meteosat-7, 9, GOES-11, 12 and MTSAT-1R as well as AMVs from Aqua and Terra MODIS, GPS radio occultation observations from COSMIC 1-6 and METOP-A GRAS as well as scatterometer wind vectors from METOP-A ASCAT, the ERS-2 scatterometer and Quikscat

SeaWinds, total column ozone products from NOAA-17 and 18 SBUV, Aura OMI while METOP-A GOME-2, Envisat SCIAMACHY, MSG SEVIRI, Envisat GOMOS/MIPAS data is only monitored.

As before, we expect to have available the following set of operational satellites and instruments over the next 10 years: 1 sounder system (HIRS[1], AMSU-A, MHS, IASI) onboard the prime METOP satellite in the mid-morning orbit, 2 conventional sounder systems (HIRS, AMSU-A, MHS) and 1 advanced sounder (CrIS) from NOAA satellites (NOAA-19, NPP, JPSS-1) in the afternoon orbit, 2 microwave imaging systems in morning orbits (DMSP F-17 or 18 SSMIS and future DoD satellites), 2 scatterometers onboard METOP and Oceansat-2 (and follow-on), 3-5 GPS receivers (COSMIC, COSMIC-2, GRAS) and 3 total column ozone sensing instruments (SBUV onboard NOAA-18 or 19, GOME-2 onboard METOP and OMPS onboard NPP, JPSS-1). This set is expected to be complemented by at least five satellites in geosynchronous orbits (2 European, 2 US and 1 Japanese satellite), and altimetry data from research satellites. The number of HIRS instruments may be revised given the fact that this series will be discontinued in the future since its observing capabilities are fully covered by advanced sounders. Chinese instruments are not accounted for in this context because the expected observation quality and data availability is not sufficiently known. This constellation has been reproduced with existing instruments as closely as possible (See Section 5).

4.4 Observing system experiments

4.4.1 Temperature/moisture sounders

In this work package, the main observing system in NWP is evaluated - the system of atmospheric temperature and moisture sounders that consists of (1) infrared radiometers, namely HIRS onboard NOAA-17, 19 and METOP, AIRS onboard AQUA and IASI onboard METOP-A; (2) microwave radiometers, namely AMSU-A and B onboard NOAA-18, 19, AQUA and METOP and MHS onboard NOAA-18, 19 and METOP. The first stage re-evaluates the sounder radiance assimilation framework as it is run in the ECMWF operational system and is based on the standard analysis and forecast scoring metrics. AMSU-A/MHS sounder denial experiments have been run to assess their impact compared to a full system. In the denial experiment, only a single AMSU-A (AQUA) remained to constrain basic temperature structures in concert with infrared sounders.

New aspects to be covered in this work package since the experiments performed by BR09 are that 10 IASI water vapour channels have been added in the operational system and that the cirrus cloud detection that produced a detrimental impact of IASI temperature sounding channels on the humidity analysis has been refined. Most information on the IASI assimilation system can be found in Collard and McNally (2009a, b). Further, the experimentation period covers an entire year producing the statistical significance that was identified to be crucial for impact interpretation by BR09.

Due to the complex information contribution of IASI to the analysis, the second part of this work package involves the advanced analysis and forecast diagnostics described before.

4.4.2 Cloud and precipitation imagers/sounders

This work package covers a new aspect of NWP observing systems: the assimilation of cloud and precipitation affected data. While a first implementation of precipitation affected microwave radiance data

[1] HIRS being discontinued after METOP-B

assimilation has been carried out at ECMWF already in 2005 (Bauer et al. 2006a, b; Kelly et al. 2007), the system has been recently extended to the full 4D-Var framework (Bauer et al. 2009, Geer et al. 2009). Here as well the advanced diagnostics provides important information on the individual channel's contribution to both analysis and forecast quality in clear, cloud and precipitation affected areas.

A system for the assimilation of overcast cloud-affected infrared radiance data has been added by McNally (2009) that is evaluated in this context. Again, the advanced diagnostics is important to separate between clear and cloud-affected observation influence.

4.4.3 Atmospheric Motion Vectors

Atmospheric Motion Vectors (AMV) derived from geostationary and polar-orbiting imagery represent the focus of the sixth work package. The impact of this data on the wind analysis is considered complementary to radiance data (Peubey and McNally 2009) with respect to the magnitude of wind increments and the altitude range at which each observation type has maximum impact. The baseline-type experiments performed by Peubey and McNally (2009) have been reiterated with respect to the EPS-period framework and with special focus on AMVs from polar-orbiting satellites (here the Moderate Resolution Imaging Spectroradiometer, MODIS onboard Aqua and Terra). Here, the impact on polar wind analysis of AMVs derived from MODIS imagery has been compared to radiances measured by HIRS.

A work package on AVHRR AMV impact estimation has been deleted from the original proposal because only very short periods of AVHRR data have been available at the time of this study and the envisaged introduction of height assignment upgrades from IASI retrievals has been evaluated elsewhere.

4.4.4 GNSS radio occultation

Occultation measurements of Global Navigation Satellite Systems have proven to be a very valuable contribution to the NWP observing system due to their absolute calibration and strong sensitivity to upper atmospheric temperature structures, an area that is otherwise only weakly constrained by other observations in the analysis and that is prone to large model uncertainties.

The objective of this work package is the estimation of the level of saturation of radio occultation observation impact on both analyses and forecasts. The estimation aims at supporting future mission planning, for example in the framework of Post-EPS. OSEs have been performed with increasing numbers of observations employing both operational (COSMIC, GRAS) and experimental missions (CHAMP, GRACE-A, Terrasar-X, etc.). Given all available observations future operational receiver constellations can be simulated and minimum vs. optimal observation numbers can be derived. These experiments also aim to provide guidelines for possible future studies employing OSSEs by verifying the estimated impact of future constellations from OSSEs with real impact results from OSEs.

4.4.5 ASCAT soil moisture

The last work package covers a new observation type that has been made available from scatterometer data (here from ASCAT), namely derived land surface soil moisture. The suitable surface analysis based on Extended Kalman Filter (EKF) technique was implemented in the ECMWF operational system in 2010 (de Rosnay et al., 2009). Compared to the previous Optimum Interpolation soil moisture analysis, the EKF soil moisture analysis significantly improved soil moisture analysis scores and 2-meter tempera-

ture forecast performances. Using ASCAT soil moisture data in addition to the screen level conventional temperature and relative humidity measurements is expected to improve further lower tropospheric analysis. A first impact demonstration of ERS scatterometer soil moisture data assimilation using a nudging scheme has been performed already by Scipal et al. (2008). They showed however that compared to the Optimum Interpolation system, using ASCAT data was slightly degrading the forecast scores. They recommended to use ASCAT data in an Extended Kalman Filter analysis to account for observation errors and to combine ASCAT data with screen level proxy information. The work package in this study investigated the impact of these observations when assimilated in the Extended Kalman Filter. Particular focus was put on lower-level atmospheric moisture analyses and precipitation.

5 Results

5.1 Temperature/moisture sounders

The reference observing system for this work package has been defined as a subset of the operationally used set of observations described before and the data selection following the recommendations of BR09. Thus the main differences with respect to the operational satellite observation usage can be summarized as:

- for conventional and advanced soundings only those from NOAA-18, AQUA and METOP;
- for microwave imager radiances only SSM/I data from DMSP-13;
- for total column ozone products only those from SBUV instruments on board NOAA-17 and NOAA-18;
- for scatterometry only ERS-2, QuikSCAT and METOP ASCAT data;
- for SATOB winds only AMVs from geostationary satellites;
- for GPSRO data only radio occultations from the COSMIC-1, 4, and 5 satellites

have been kept in the reference (denoted 'Reference' hereafter) system.

To understand the impact of conventional sounders two denial experiments have been performed, one in which AMSU-A and MHS sounder data have been denied (except for AMSU-A on AQUA) and another one in which HIRS data have been denied. Keeping AQUA AMSU-A radiances was desirable to ensure that the denial experiment still produces reasonable results, especially over the large, data sparse areas of the Southern hemisphere. Previous experiments have shown that this can be accomplished by a single microwave sounder with 4D-Var system over an assimilation window of 12 hours.

In contrast to the BR09 study, where the impact of a single instrument or a group of instruments from METOP has been studied keeping all other types of data un-touched, the intention of the present study is to understand the more general impact of an individual instrument type. The experiments have been run for more than 7 months over the second half of 2009 to ensure statistical significance of the results.

5.1.1 Conventional infrared/microwave sounders

Analyses and short range forecasts (also called first-guess since it is used as an a priori constraint in the analyses) have been compared to observations in observation space. They provide statistics on the fit of

model analysis and first-guess to all available types of observation. In the context of OSEs the statistics provide useful information on the impact of a given data type on the fits when experiments with and without the data are compared.

Figure 1a shows the analysis and first-guess fit to radiosonde temperature observations for the AMSU-A/MHS denial experiment as compared to the Reference. It is clearly seen that AMSU-A/MHS is reducing the analysis and even more the first-guess bias for stratospheric radiosonde temperatures. This impact is strongest above 10 hPa. Generally, upper stratospheric temperatures are most strongly constrained by microwave sounders and GPSRO data while at lower levels infrared sounder data becomes increasingly effective in the temperature analysis.

For the same denial experiment, Figure 1b shows the influence of AMSU-A/MHS data on the analysis and short range forecast fits to COSMIC GPSRO bending angle biases at 38-40 km altitudes. Obviously, AMSU-A data are in better agreement with higher stratospheric radiosonde temperature observations while both radiances and radiosonde observations disagree with GPSRO data at those altitudes.

As seen on Figure 2, the assimilation of NOAA-18 and METOP AMSU-A radiances slightly improves the fit to AQUA AMSU-A radiances in terms of standard deviations. At the same time the AQUA AMSU-A bias correction is reduced for channels 10-13. These changes are small but given the length of experimentation they seem to be significant.

The influence of humidity sounding on the analysis has been examined by investigating the impact of data denial on the consistency with other moisture sensitive radiances and radiosonde humidity profiles. Comparison with water vapour channel data of Meteosat and GOES indicates positive or neutral impact for both first-guess and analysis. This impact is summarized in Table 2, which contains the reduction of root-mean-square (RMS) difference between model (analysis or first-guess) and water vapour channel radiance data from geostationary satellites.

The numbers generally indicate an error reduction due to the presence of AMSU-A/MHS (or HIRS) data measured in 1/100 or 1/1000 of degree Kelvin (brightness temperature). Positive numbers mean that the presence of AMSU-A/MHS (or HIRS) reduces the RMS error and the analysis and first-guess are more consistent with water vapour channel data from the geostationary imagers. The strongest impact can be seen with respect to GOES-12 water vapour channel-2 over the Southern hemisphere for which the analysis and first-guess error histograms of the AMSU-A/MHS denial and control experiments can also be seen in Figure 3. These histograms confirm that the assimilation of humidity sounders narrows the error distribution, especially in the analysis, but to some extent also for the first-guess. Figure 4 shows the same type of error histogram for ENVISAT MERIS total column water vapour contents over the Tropics and Southern hemisphere (land only). This comparison also indicates some moderate improvement due to the presence of AMSU-A/MHS data with an RMS error reduction of 0.02-0.04 kg/m^2.

The comparison of the analysis impact on the fit to advanced sounders shows that the assimilation of AMSU-A/MHS also results in assimilating slightly more AIRS data and this increase varies between 0.5 and 1% depending on the AIRS channel. In terms of analysis and first-guess model fits to AIRS data no change can be detected. For IASI, bigger differences can be identified. Figure 5 shows the analysis and first-guess fits to three bands of assimilated channels (top: temperature sensitive channels, middle and bottom: two sets from a total of 10 assimilated humidity sensitive channels), left panel a) shows the Northern hemisphere, right panel b) shows the Southern hemisphere. Interestingly, while for the analyses no differences can be identified (blue and green curves) between the experiments, both standard deviation and bias of the first-guess has changed with the assimilation of AMSU-A/MHS (red and black curves). In terms of error standard deviation there is a clear improvement with the assimilation of AMSU-A/MHS in the humidity band of IASI, especially for channels 2889-3110.

Southern Hemispheric temperature channel biases increase and become larger with increasing altitude. Also in the humidity bands in both hemispheres a systematic change of bias can be observed, indicating that the model produces systematically lower brightness temperatures when AMSU-A/MHS are present. This corresponds to a moistening since an increase of water vapour pushes the sounding channel weighting functions to higher altitudes. This systematic difference is clearly seen in Figure 5 where it is present for the entire assimilated humidity channel spectrum. However, note that these shifts of model vs observation differences amount to only 0.02-0.04 K.

Some systematic differences with respect to radiosonde humidity profiles can be also identified over the Southern hemisphere in Figure 6a. In this case it shows that the model (both analysis and first-guess) is systematically drier when AMSU-A/MHS data are assimilated. A similar effect can be obtained when SSM/I data is denied (Fig. 6b). This data is only assimilated over oceans and affects the total column water vapour more strongly than MHS data, which also explains why the discrepancy of the radiosonde humidity observations between data denial and Reference experiments is larger.

Apart from observation statistics, it is worth verifying the systematic impact of moisture-sensitive data denials on the mean total column water vapour state. Figure 7 shows mean analysis difference maps between AMSU-A/MHS denial and Reference experiments where the average has been computed for summer (a) and for autumn (b) separately. It can be seen that the summer and autumn distributions are rather similar. Over oceans (land) the presence of AMSU-A/MHS data seems to slightly moisten (dry) the analysis. This is in agreement with what has been observed from the radiosonde humidity departures. The shift of systematic differences between IASI radiances (Fig. 5) reflects the moistening over oceans since this data is not used over land surfaces.

The denial of HIRS data has a small but noticeable impact on the analysis and short-range forecast fit to water vapour channel data from geostationary satellites as seen in Table 2. When HIRS data are present, the number of assimilated AIRS and geostationary satellite radiances also slightly increases, but this change is of the order of 0.1%. More impact of a HIRS data denial can not be seen in the analysis.

The evaluation of the forecast performance for the AMSU-A/MHS/HIRS denial experiments has been performed by analyzing the normalized differences of RMS forecast errors from verification against the operational analyses. Figure 8 shows the zonal cross-sections of normalized root-mean square temperature forecast error differences between the AMSU-A/MHS denial experiment and the Reference. Positive values indicate a positive impact of the AMSU-A/MHS instruments and the hatching denotes areas where the differences are statistically significant at the 95% level.

The impact of the sounders is strong and significantly positive, especially over the Southern hemisphere and through the entire atmosphere. The positive impact is significant up to 4 days in the Southern hemisphere and up to 2 days in the Northern hemisphere. The situation is similar for humidity scores as shown in Figure 9. The geographical distribution of normalized geopotential height and relative humidity RMS error differences for the same experiments at the 500 hPa level is shown in Figure 10 and Figure 11, respectively. Both maps confirm the generally strong positive impact of AMSU-A/MHS assimilation and illustrate that the impact is stronger and lasts twice as long over the Southern hemisphere compared to the Northern hemisphere.

However, the geopotential scores show some seemingly negative impact, especially over South-America for the 24-hour forecast range. The magnitude of the RMS error difference is shown in Figure 12 in *m* without normalization. The plot suggests that the error difference is between 1-5m, which is comparable in size to the generally positive impact in all other areas at low and mid latitudes. While the error amounts are not large, this features still deserves attention since it appears over a well defined area suggesting the possibility of insufficient quality control or surface emissivity modeling.

Figure 13 and Figure 14 show a comparison of the normalized RMS forecast error differences for three denial experiments (AMSU-A/MHS, HIRS and SSM/I) with respect to the Reference for temperature and humidity, respectively. Positive values indicate that the given instrument has a positive impact on the scores when compared against the operational analysis. The comparison shows that the impact of AMSU-A/MHS data is the strongest, except for the lower boundary layer in the Tropics, where SSM/I improves the scores more effectively than AMSU-A/MHS, both for temperature and humidity. Everywhere else the AMSU-A/MHS data impact is the most positive and over the Southern hemisphere it lasts well into the medium range, occasionally up to 8 days. The impact of SSM/I data in this context will be further discussed in Section 5.2.

Summary

The impact of the conventional sounders, namely AMSU-A, HIRS and MHS is strong and significantly positive when evaluated by the fit of model analyses and short-range forecasts to all observations contained in the system and when analyzing forecast scores. The individual impact of HIRS is fairly small compared to that of the microwave sounders given that the background observing system contains two advanced sounders, namely AIRS and IASI. The positive impact of microwave sounders on temperature and geopotential forecast skill is especially evident in the Southern hemisphere and throughout the entire atmosphere. The positive impact is significant up to 4 days in the Southern hemisphere and up to 2 days in the Northern hemisphere. One area of seemingly negative impact (over South America) requires further investigation but could be the result of insufficient quality control or inaccurate surface emissivity modeling. The situation is similar for humidity scores. Over oceans the presence of AMSU-A/MHS data seems to slightly but systematically moisten the analysis, while over land the opposite effect is observed. This is mainly caused by the MHS radiance assimilation. This impact is in agreement with what has been observed from the radiosonde humidity departures in the analyses, that are mostly located over land surfaces, and the comparison of model analyses and short-range forecasts with IASI radiances (water vapour channels) that are only used over oceans.

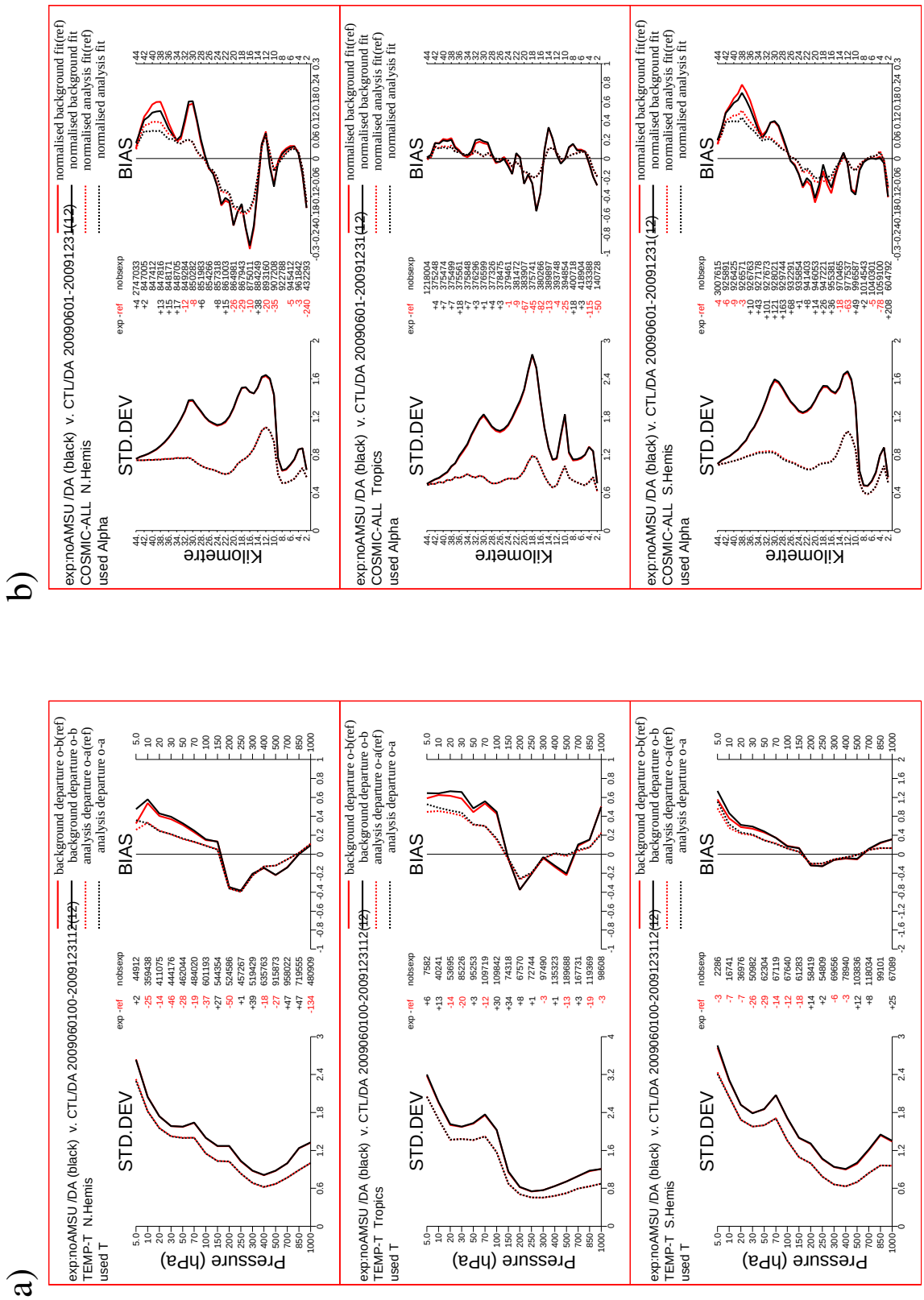

Figure 1: a): Fit of model first-guess (solid) and analysis (dashed) to radiosonde temperatures in the Northern hemisphere (top), Tropics (middle) and Southern hemisphere (bottom) from AMSU-A/MHS denial (black) and Reference (red) experiments. Left panels show standard deviations, right panels show biases. Numbers in central columns denote the data sample from the denial (right, black) experiment and the difference between denial experiment and Reference (left, black or red). Statistics were generated from period 01/06-31/12/2009. b): Same as a), but statistics for COSMIC GPSRO bending angles.

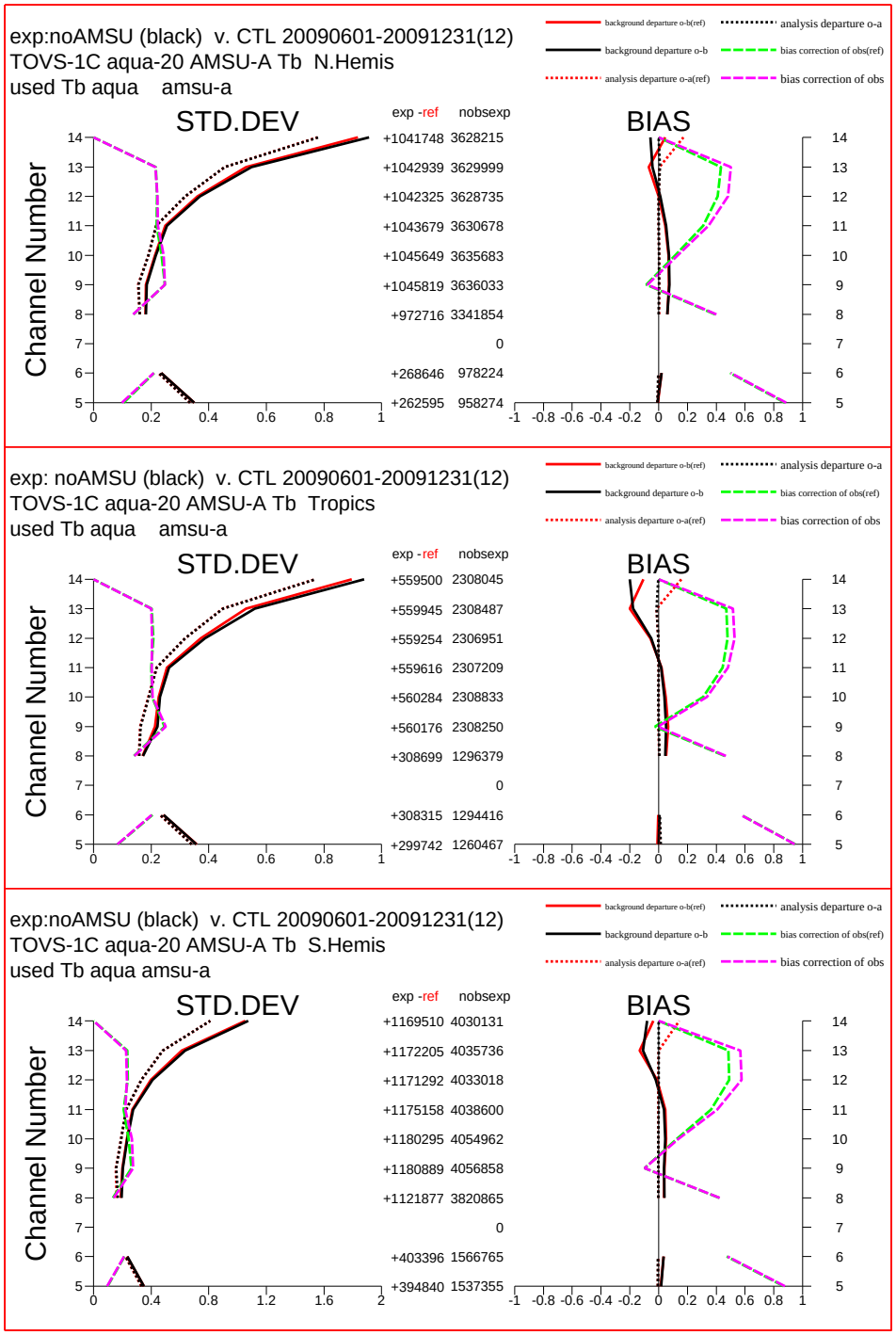

Figure 2: Fit of model first-guess (solid) and analysis (dashed) to AQUA AMSU-A radiances in the Northern hemisphere (top), Tropics (middle) and Southern hemisphere (bottom) from AMSU-A/MHS denial (black) and Reference (red) experiments. Left panels show standard deviations, right panels show biases. Numbers in central columns denote the data sample from the denial (right, black) experiment and the difference between denial experiment and Reference (left,red or black). Statistics were generated from period 01/06-31/12/2009. Green and pink curves denote bias correction from Reference and denial experiment, respectively.

Table 2: Change of RMS error differences between model analysis and first-guess and GOES/METEOSAT water vapour channel brightness temperatures. Change is defined as RMS error of AMSU-A/MHS (or HIRS) denial experiment minus RMS error of Reference in 1/100 degree Kelvin of brightness temperatures for first guess and 1/1000 degree Kelvin of brightness temperatures for analysis departures.

Satellite, Area	AMSU-A/MHS denial first-guess	AMSU-A/MHS denial analysis	HIRS denial first-guess	HIRS denial analysis
Meteosat-7 6.4 µm:				
Northern hemisphere	+3	+23	0	+5
Tropics	+4	+11	+3	+3
Southern hemisphere	+3	+12	-1	+3
Meteosat-9 6.2 µm:				
Northern hemisphere	0	+13	0	+4
Tropics	+1	+2	+1	+1
Southern hemisphere	+3	+2	-2	0
Meteosat-9 7.3 µm:				
Northern hemisphere	+4	+15	+1	+0
Tropics	+4	+18	+2	+1
Southern hemisphere	0	+23	-2	+3
GOES-11 WV 6.7 µm:				
Northern hemisphere	+1	+12	+1	+4
Tropics	-1	+16	0	+6
Southern hemisphere	+2	+22	0	+8
GOES-12 WV 6.7 µm:				
Northern hemisphere	+3	+4	0	+4
Tropics	+3	+22	0	+5
Southern hemisphere	+6	+24	+1	+5

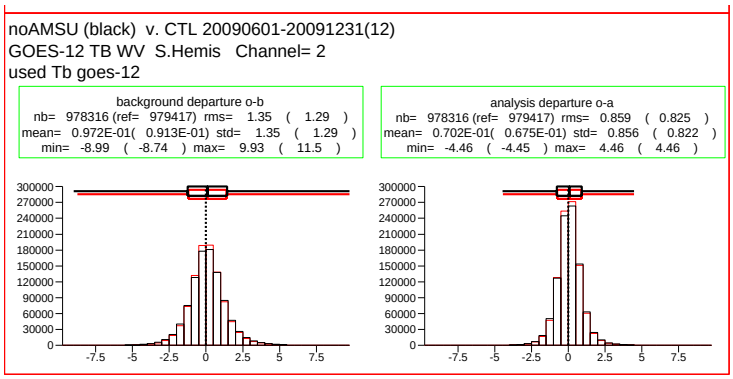

Figure 3: Fit of model first-guess (left) and analysis (right) to GOES-12 channel 2 radiances comparing AMSU-A/MHS denial (black) and Reference experiments (red) over the Southern hemisphere. Statistics were generated from period 01/06-31/12/2009.

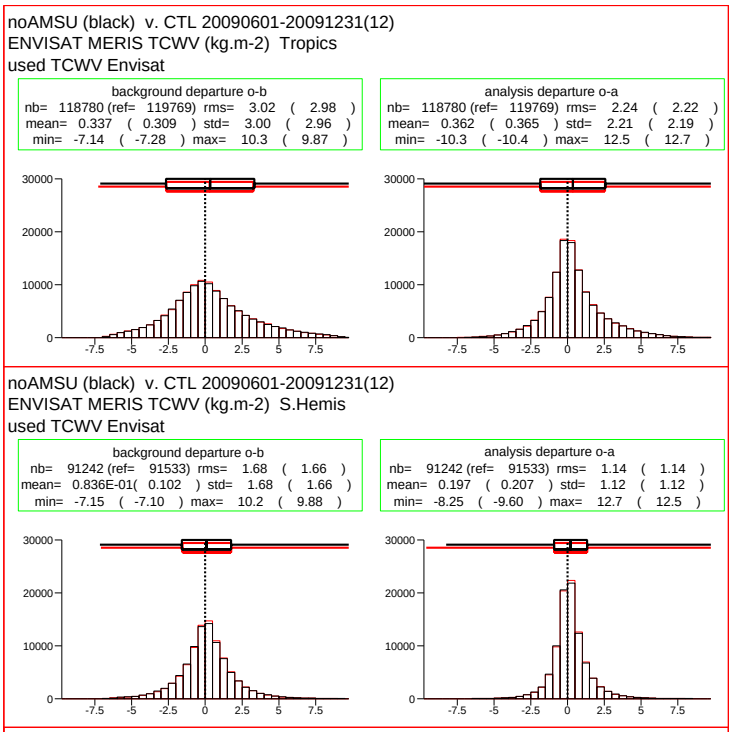

Figure 4: Fit of model first-guess (left) and analysis (right) to ENVISAT MERIS total column water vapour content comparing AMSU-A/MHS denial (black) and Reference experiments (red) over the Tropics (top) Southern hemisphere (bottom). Statistics were generated from period 01/06-31/12/2009.

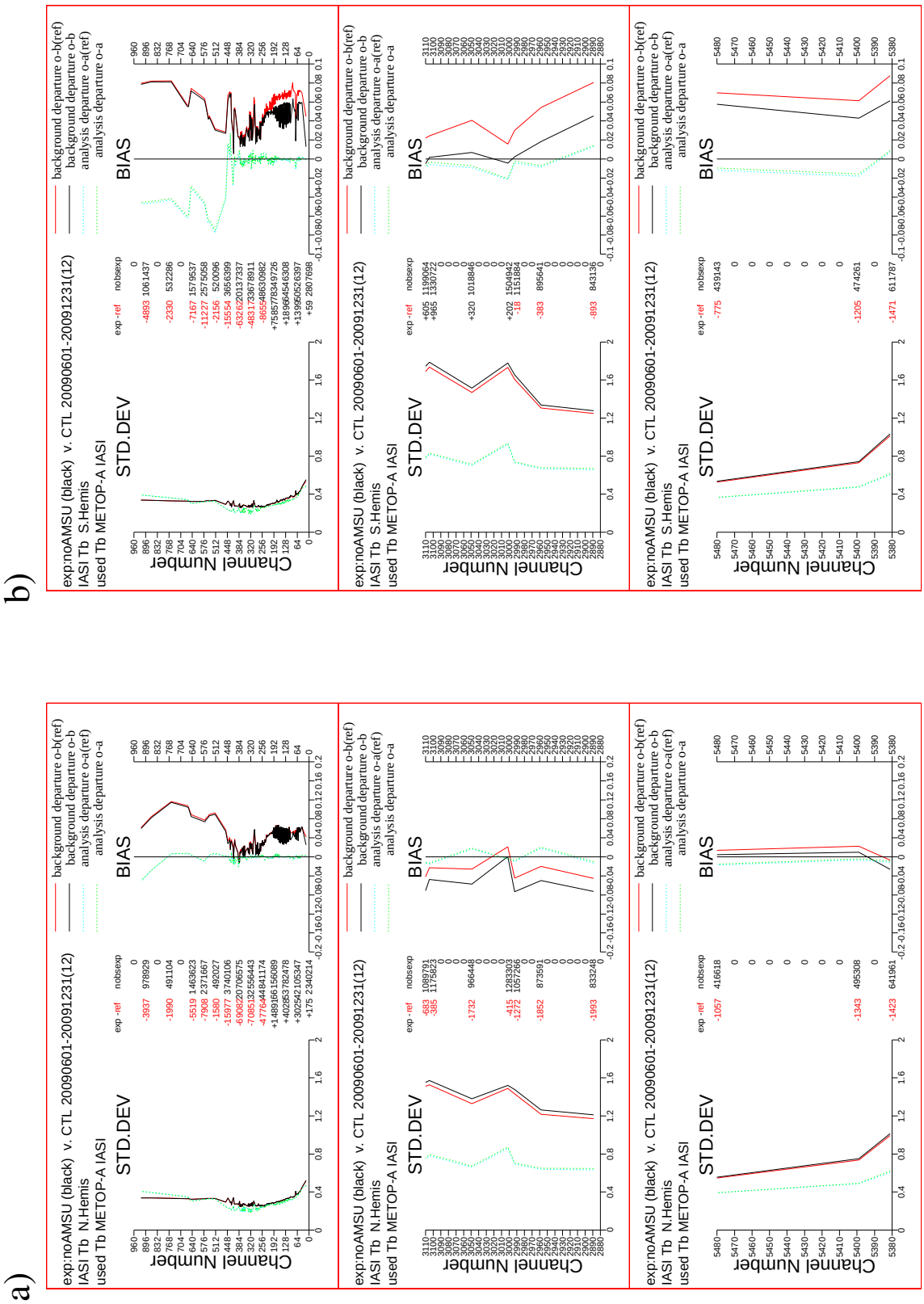

Figure 5: Fit of model first-guess (solid) and analysis (dashed) to IASI brightness temperatures for temperature channels (top), humidity channels (middle and bottom) from AMSU-A/MHS denial (black) and Reference (red) experiments. Left panels show standard deviations, right panels show biases. Numbers in central columns denote the data sample from the denial (right, black) experiment and the difference between denial experiment and Reference (left, black or red). Statistics were generated from period 01/06-31/12/2009. a) shows Northern hemisphere and b) Southern hemisphere.

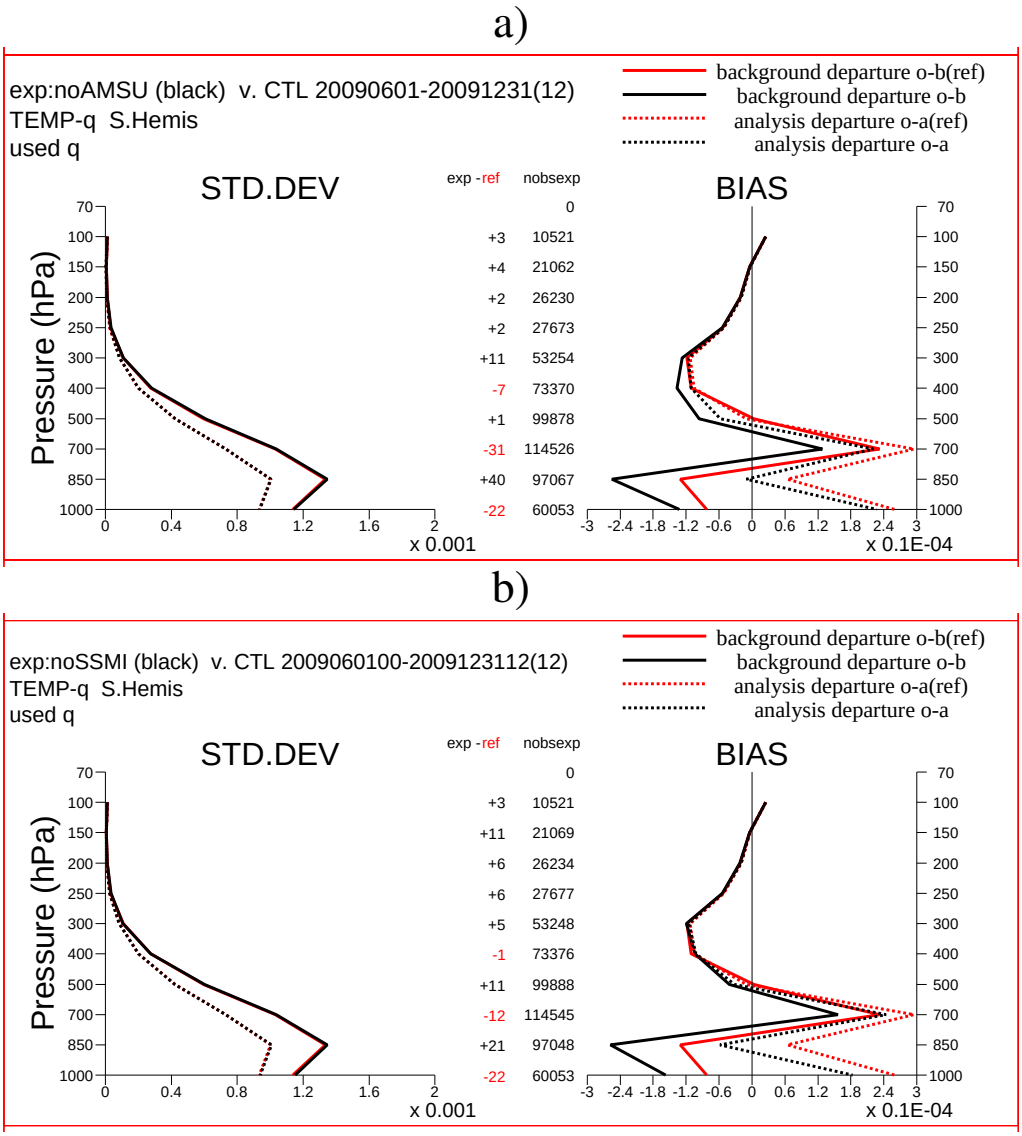

Figure 6: Fit of model first-guess (solid) and analysis (dashed) to radiosonde specific humidity between a) AMSU-A/MHS denial (black) and Reference (red) experiments, b) SSM/I denial (black) and control (red) experiments. Left panels show standard deviations, right panels show biases. Numbers in central columns denote the data sample from the denial (right, black) experiment and the difference between denial experiment and Reference (left, black or red). Statistics were generated from period 01/06-31/12/2009. Both figures show statistics from Southern hemisphere.

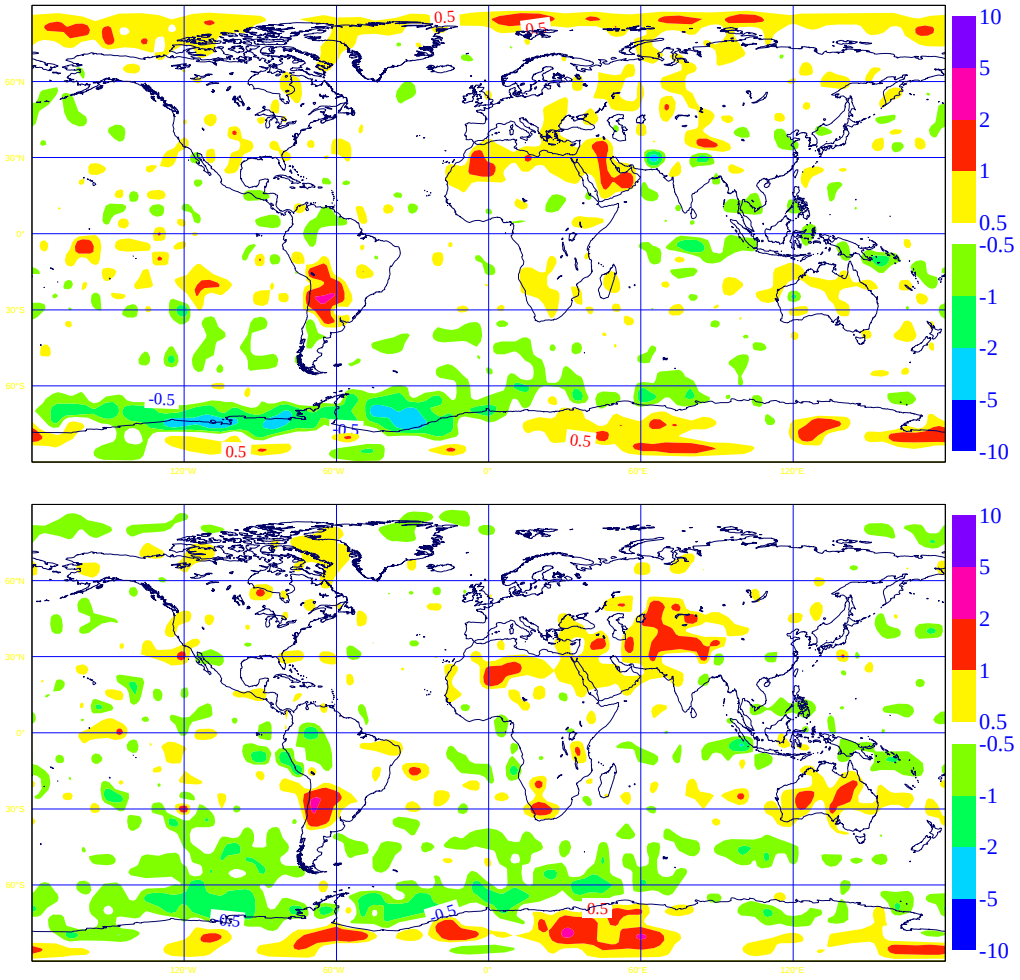

Figure 7: Normalized mean analysis difference maps of total column water vapour content between AMSU-A/MHS denial experiment and Reference, where the average has been counted for the 3 months in summer (top) and for autumn (bottom) separately. Yellow to red (green to blue) colours indicate that the denial experiment is more (less) humid than the Reference.

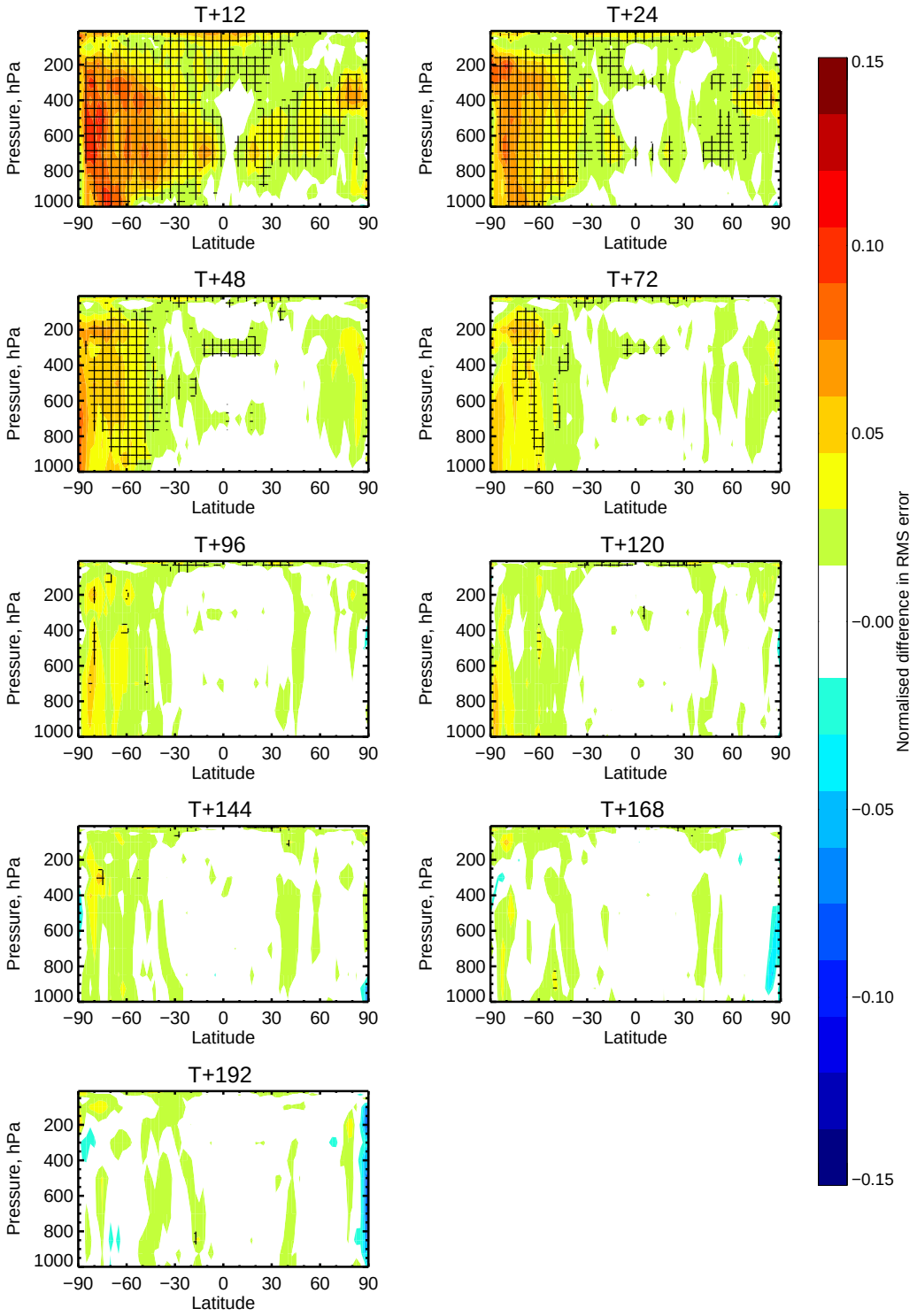

Figure 8: Zonal cross-sections of normalized RMS forecast error difference between AMSU-A/MHS denial and Reference experiments for temperature. Positive values indicate a positive impact of the assimilated AMSU-A/MHS radiances. Panels show forecast range of 12, 24, 48, 72, 96, 120, 144, 168 and 192 hours. Crosses indicate where cores are statistically significant to the 95% level. Forecast verification is against operational analyses; verification period is 20/05-31/12/2009.

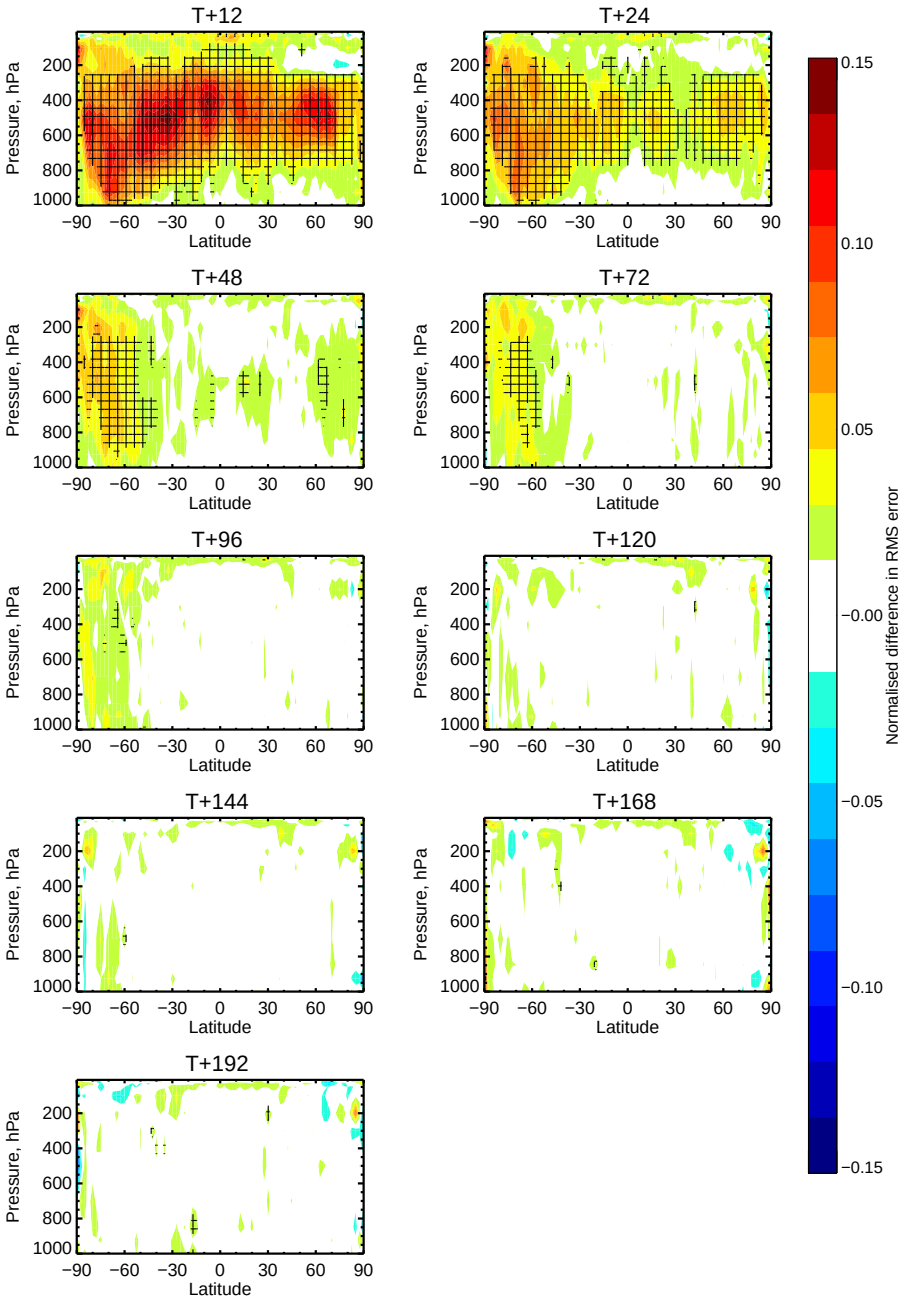

Figure 9: As Figure 8 for relative humidity.

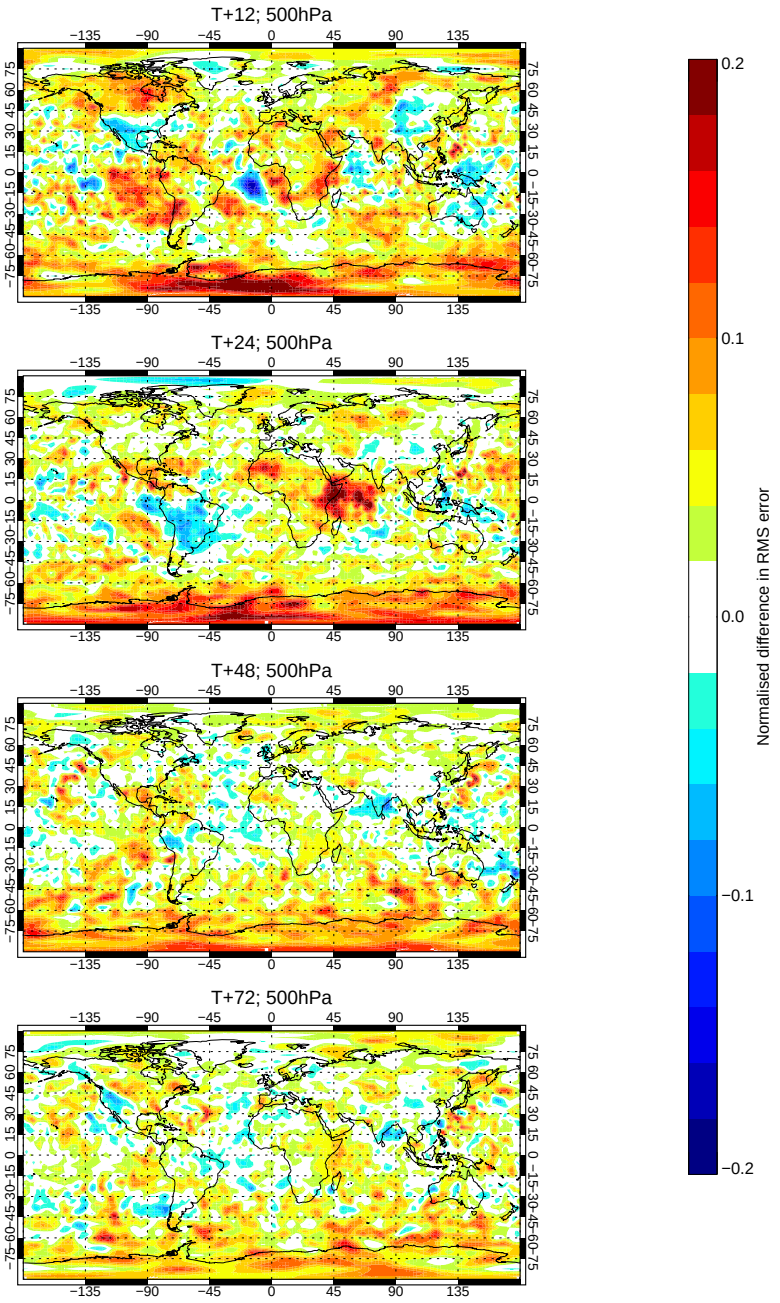

Figure 10: Normalized RMS forecast error difference between AMSU-A/MHS denial and Reference experiments for 500 hPa geopotential height. Positive values indicate positive impact of the assimilated AMSU-A/MHS radiances. Panels show forecast range of 12, 24, 48 and 72 hours (from top to bottom). Forecast verification is against operational analyses; verification period is 20/05-31/12/2009.

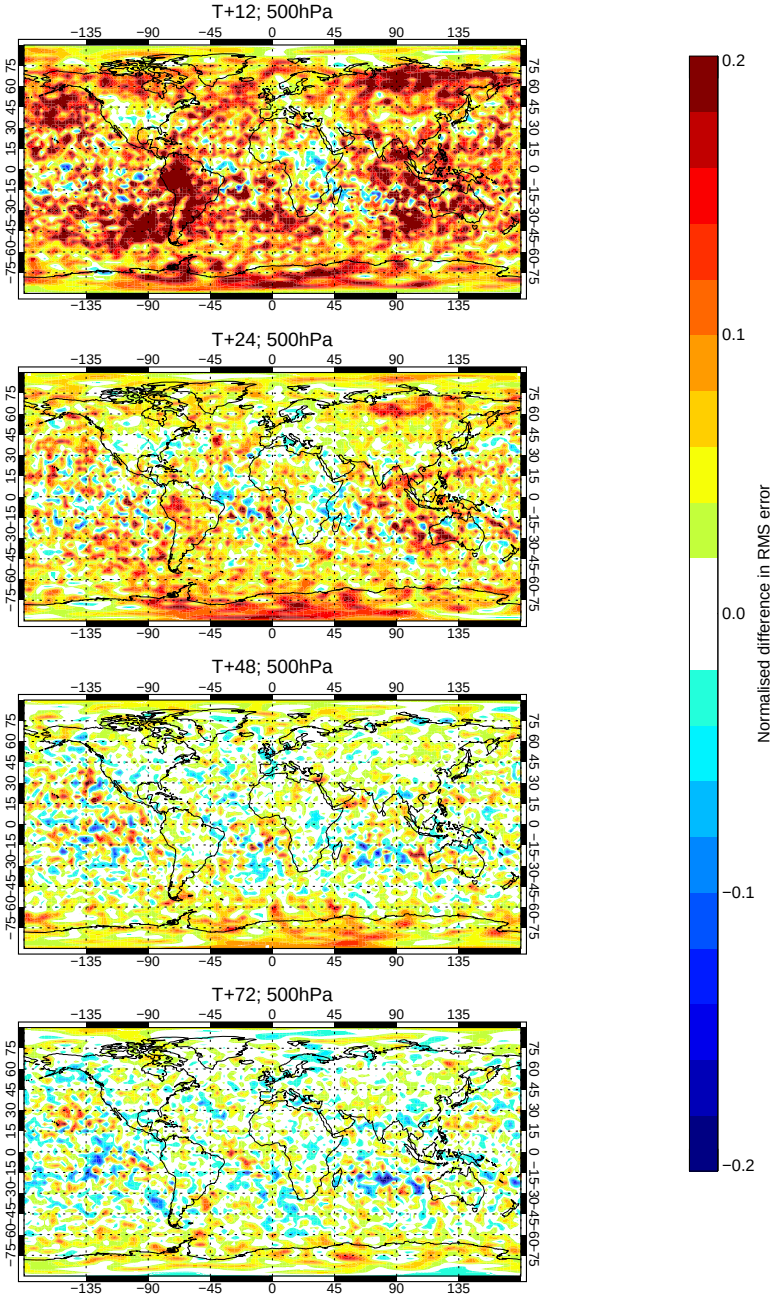

Figure 11: As Figure 10 for relative humidity.

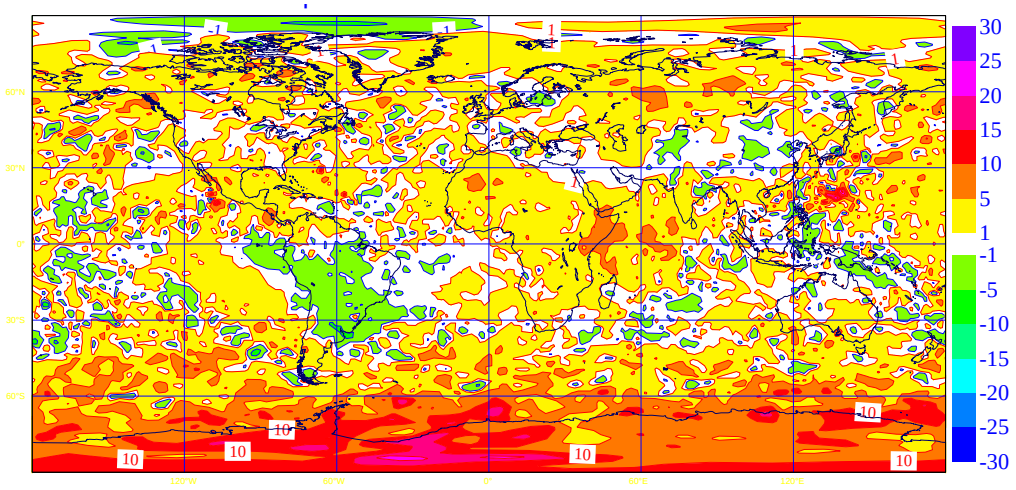

Figure 12: RMS forecast error difference between AMSU-A/MHS denial and Reference experiments for 500 hPa geopotential height in m for the 24-hour forecast range. Positive values indicate positive impact of the assimilated AMSU-A/MHS radiances. Forecast verification is against operational analyses; verification period is 20/05-31/12/2009.

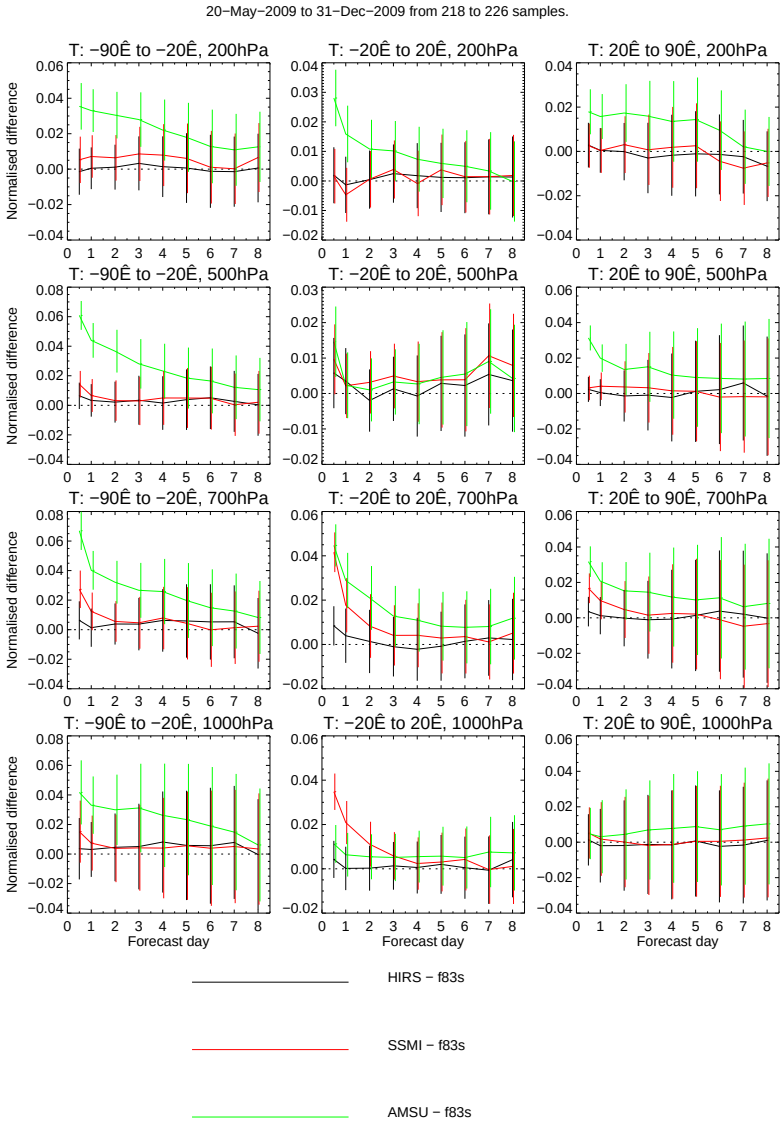

Figure 13: Normalized RMS forecast error difference between AMSU-A/MHS, HIRS and SSM/I denial and Reference experiments for temperature. Positive values indicate positive impact of the given instrument. Left, middle and right columns refer to Southern hemisphere, Tropics and Northern hemisphere. Rows correspond to 200, 500, 700 and 1000 hPa (from top to bottom). Forecast verification is against operational analyses; verification period is 20/05-31/12/2009.

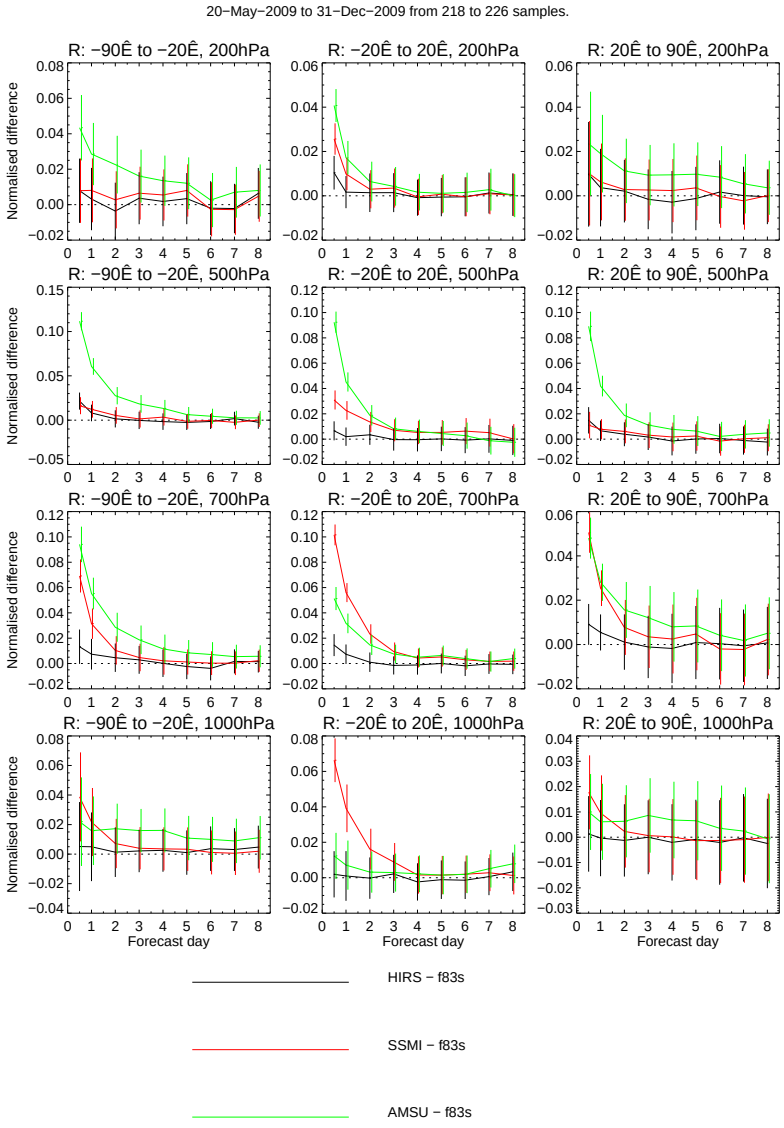

Figure 14: Normalized RMS forecast error difference between AMSU-A/MHS, HIRS and SSM/I denial and Reference experiments for humidity. Positive values indicate positive impact of the given instrument. Left, middle and right columns refer to Southern hemisphere, Tropics and Northern hemisphere. Rows correspond to 200, 500, 700 and 1000 hPa (from top to bottom). Forecast verification is against operational analyses; verification period is 20/05-31/12/2009.

5.1.2 Advanced infrared sounders

The AIRS instrument onboard the NASA AQUA satellite and the IASI instrument onboard the EUMETSAT METOP satellite are arguably the two most sophisticated atmospheric sounders ever flown. Due to their very high resolution sampling of the infrared spectrum they have the potential to provide more detailed and accurate information about atmospheric temperature and composition than has been possible with previous satellite sensors.

ECMWF together with other NWP centres assigned a very high priority (and devoted significant resources) to the successful exploitation of data from AIRS and IASI. Results quickly emerged that clearly demonstrated that the new information brought by these instruments was beneficial to NWP systems and improved forecast skill. On the basis of these results, first AIRS (in 2003) and subsequently IASI (in 2007) became important elements of the operational observing system.

The results of pre-operational trials of AIRS and IASI from a number of NWP centres have been published in the open literature, but more recent evaluations of their impact have been rather limited. In view of the prominent position occupied by these instruments and the fact that the planning process for the next generation infrared sounders is now under way, it was considered timely to perform an extensive and consolidated review of the NWP impact of advanced IR sounders.

In this OSE the model has been run at T511 horizontal resolution, just like for the conventional sounder OSEs described in Section 5.1.1, and with version CY35R2 of the ECMWF IFS. While this is not the most recent version of the analysis system, it was operational at the time the study began. Between the model cycle used in this study and the current operational version (36R1) there has only been one significant change directly relevant to the usage of advanced IR sounders namely the assimilation of overcast (cloudy) scenes. While the overcast data are thus not included in this part of the study, their impact upon the analysis and forecasting system is quantified in Section 5.2.

The use of radiance observations from advanced IR sounders for this study broadly follows the descriptions in McNally et al. (2006) for AIRS and Collard and McNally (2009a and b) for IASI, but is summarised here for completeness: Most of the assimilated channels come from the long-wave temperature sounding band (153 IASI, 83 AIRS). Short-wave temperature sounding channels that are unaffected by solar radiation / non-local thermodynamic equilibrium (LTE) are assimilated from AIRS, but none are used from the IASI short-wave band due to the very high instrument noise. A very modest selection of water vapour sounding channels (10) are used from both AIRS and IASI. No channels from the ozone band of AIRS or IASI are assimilated. Only data that are identified as being free from clouds are assimilated, although these generally include observations in cloudy situations when most of the emission in a particular channel comes from far above the cloud top. Except for a small selection of AIRS stratospheric channels, no advanced IR sounder data are assimilated over land surfaces.

Experimental setup

The period considered in these experiments is 07/08/2008 to 06/08/2009 and thus covers an unprecedented full continuous calendar year. Two different types of impact experiment have been run: Firstly addition experiments where AIRS and IASI are added separately and in tandem to a Baseline that contains no advanced IR sounder data (but does contain all other satellite and conventional observations and therefore more data than Reference). The primary aim of this is to quantify the benefits brought by the additional assimilation of these data. Secondly, denial experiments have been run where AIRS and IASI are removed individually and together from a control system that otherwise exploits the full

global observing system. The primary aim of this is to quantify the cost of losing data from one or both sounders.

Two basic metrics are used to quantify the impact of AIRS and IASI: Firstly the impact upon the analyses in terms of mean changes to important fields and the effect of these on the fit to other observations. Secondly the impact upon forecast skill verified using analysis fields and observations.

Results of data addition experiments

Changes to the analyzed temperature field when AIRS and IASI are added are shown in Figure 15. It can be seen that both instruments cause very similar modest adjustments to the large scale annual mean. There is a warming at lower levels in the Tropics and a cooling at higher latitudes, with the opposite signal observed in the upper troposphere. The only obvious differences between the impact of AIRS and that of IASI is near the surface in the northern polar region (where AIRS causes a stronger warming) and the Tropics (where IASI produces a stronger low-level warming). Mean changes to the analysis can, to some extent, be verified by how they result in a change of the fit of the analysis to other observations. Figure 17 shows some examples of the mean fit of radiosonde temperature and wind observations with IASI (red lines) and without IASI (black lines). While hemispheric averages over the full year of radiosonde fitting statistics are unchanged (and thus not shown), the agreement with temperature data at both poles and in the Tropics is generally improved when IASI is assimilated.

The fit to low-level wind data at the southern pole is better, but wind data at the northern pole show a degradation. This suggests that the enhanced large scale north-south temperature gradient forced by the assimilation of IASI (resulting from the warming in the Tropics and cooling at the pole) may be too strong resulting in an excessive westerly wind flow at high latitudes. Analysis changes caused by the addition of AIRS data produce very similar changes to the radiosonde fitting statistics (and are thus not shown). However, the degradation of northern polar radiosonde wind statistics is not seen from the addition of AIRS data.

There are also changes to the mean analyzed humidity when AIRS and IASI are used. Again the impact of AIRS is very similar to that of IASI as shown in Figure 16. They both cause a drying in the Tropics (typically less than 2 %) and a moistening of the Southern Hemisphere mid-latitudes (typically less than 1 %). The mean fit to tropical and Southern Hemisphere radiosonde humidity data is marginally improved with these analysis changes (Figure 18).

Forecast scores for geopotential height from the experiments where AIRS and IASI are added compared to the baseline system (that contains neither) are shown in Figures 19, 20 and 21. In each case the quantity plotted is the reduction in RMS error, normalized by the RMS error of the baseline system. The forecasts are verified against operational analyses and error bars superimposed represent 95 % confidence intervals. Hemispheric scores are shown, but also results for two specific regions. The continental United States (US) and Europe (EU) are obviously important areas where we require the forecast to perform well. However, they are also interesting in this context as the verifying analyses in these regions are highly constrained by conventional observations (i.e. radiosondes and aircraft) and are therefore more independent of the satellite data changes than the analyses over ocean.

It can be seen that the addition of AIRS or IASI to the baseline has a clear positive impact and reduces RMS forecast errors. The hemispheric impact of AIRS is very similar to that of IASI. Both instruments show the largest reduction in the short-range forecast error, but there is a statistically significant signal out as far as day 6. In the US and EU regions the short-range forecast error impact from AIRS and IASI is smaller, but this is because conventional observations determine the local initial conditions very strongly

in these areas and the influence of satellite data is weaker. In the medium-range forecast errors (where the initial conditions from remote ocean areas are important) we again see a statistically significant benefit of adding either instrument. One exception is that the addition of IASI appears to have only a very small medium-range impact over the EU region. In Figure 21 we see that the addition of AIRS and IASI together generally produce a larger impact than that of either instrument alone. This is an important result as it suggests that there is a measurable benefit to forecast skill from flying two advanced IR sounders.

Forecast scores for relative humidity also show a clear reduction in RMS error when either AIRS or IASI (or both) are added to the baseline system (Figure 22, 23, 24 and 25). Averaged over the extra-tropical hemispheres and the Tropics the positive signal is strong and statistically significant (more so than observed for the geopotential forecast errors). There is again a potential concern over the choice of verifying analyses which in previous studies for humidity, has been found to be particularly important. However, we can again have more confidence in the signals obtained over the EU and US limited areas where the verifying operational analysis is highly constrained by conventional data. In these regions we see smaller, but still positive and statistically significant reductions in RMS forecast error. Again, one exception is (as was seen for geopotential forecasts) that the addition of IASI appears to have only a very small medium-range impact over the EU region.

Results of data denial experiments

Forecast scores for the experiments where AIRS and IASI are denied from a control system (that contains all available observations) are shown in Figures 26, 27 and 28. In each case the quantity plotted is the increase RMS error, normalized by the RMS error of the control system. As previously, the forecasts are verified against operational analyses. For the hemispheric scores shown in Figures 26 and 27 it can be seen that the removal of either AIRS or IASI data degrades the skill and results in larger RMS forecast errors. The increase in error from removing a single instrument is clearly smaller than the corresponding reduction in forecast that was seen from adding the same instrument to the baseline system (see above). This suggests that one advanced IR sounder is able to partially compensate for the loss of the other. The impact of losing AIRS is visible in the short-range forecast scores for the EU and US regions, but in the medium-range there is no measurable loss of skill. The impact of losing IASI is visible only in the short-range forecast scores for the US region. For the EU region there is no loss of skill in the short-range forecasts and in the medium-range the skill actually improves when IASI is removed. That is to say that European forecasts from analyses based only on AIRS data are better than those run from analyses based on AIRS plus IASI. This anomaly is consistent with the results of the data addition experiments that showed IASI having only a weak impact over Europe.

Forecast scores for relative humidity from the denial experiments largely reflect those of the geopotential forecasts and are thus not shown. In summary, the signals are similar, but smaller than for the addition experiments demonstrating the ability for one sounder to partially compensate for the loss of another. Crucially, the anomalous result of geopotential forecasts that removing IASI improves medium-range forecasts over the EU region is also seen in the humidity scores.

Forecast verification against radiosonde observations

All the forecast scores presented so far have used the ECMWF operational analyses for verification. During this test period AIRS and IASI data were both assimilated and there is a potential issue that this may influence the results. To test this all the geopotential forecasts have been additionally verified against radiosonde observations. In the short-range there is a reduced impact of adding or removing AIRS and

IASI (either separately or together) compared to the scores from analyses based verifications. There is no contradiction - this is again due to the radiosonde data strongly constraining the initial conditions in their vicinity making short-range forecasts errors insensitive to changes in satellite data usage. In the medium-range forecast scores against radiosondes there is, without exception, a near exact correspondence with the results obtained from analysis based verification. For this reason the scores verified against radiosondes are not shown. It is not currently possible at ECMWF to verify humidity forecasts against radiosonde humidity observations.

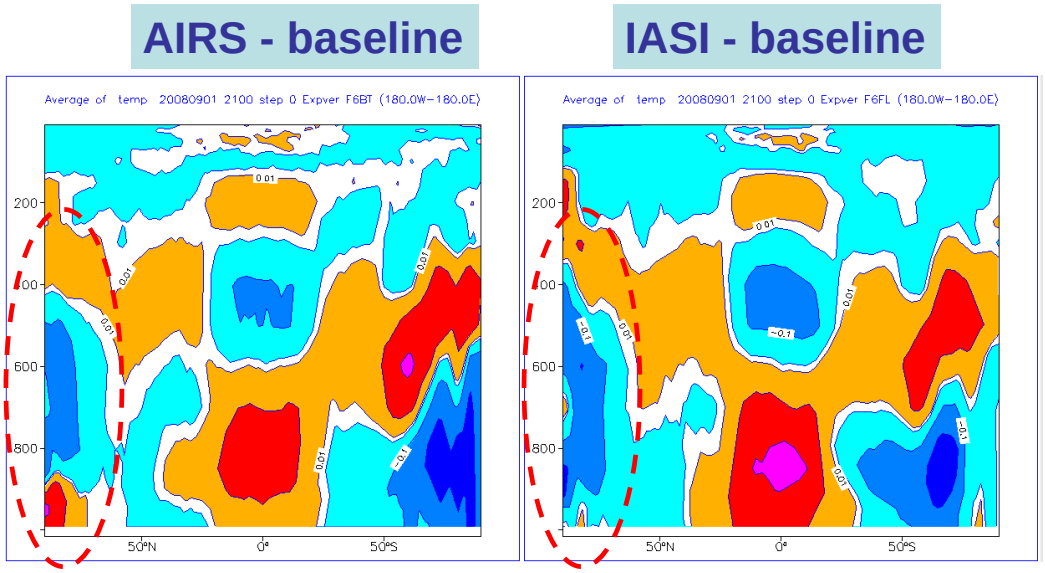

Figure 15: Zonally averaged mean analyzed temperature differences when AIRS (left) and IASI (right) are added to the baseline system. Contours are at 0.01,0.05,0.1 and 0.25 K. Positive values (red and yellow) mean that adding the instruments makes the analyses warmer.

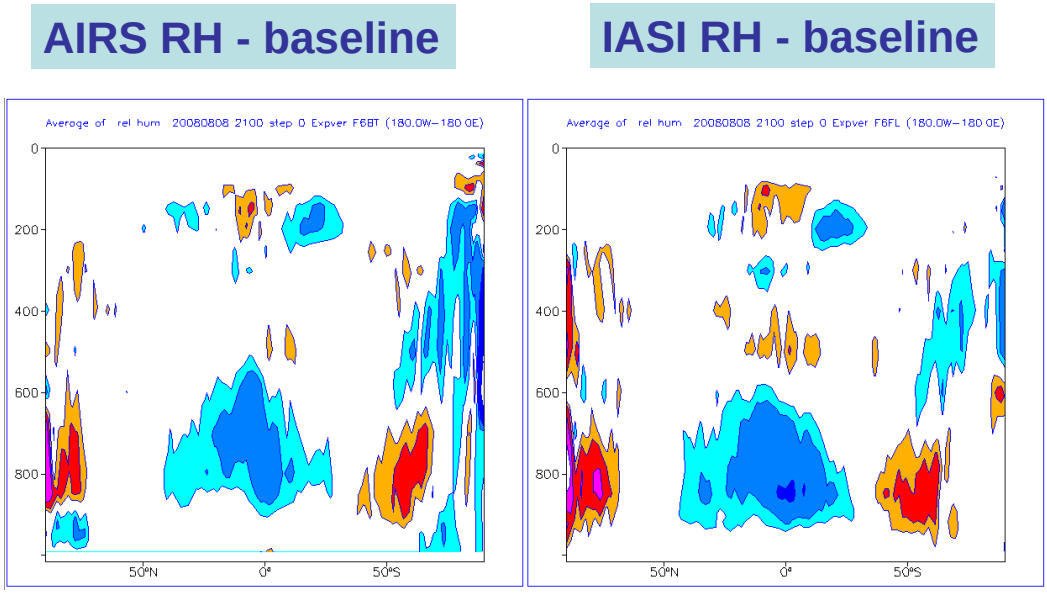

Figure 16: Zonally averaged mean analyzed relative humidity differences when AIRS (left) and IASI (right) are added to the baseline system. Contours are at 0.5,1.0,2.0 and 5.0 %. Positive values (red and yellow) mean that adding the instruments makes the analyses wetter.

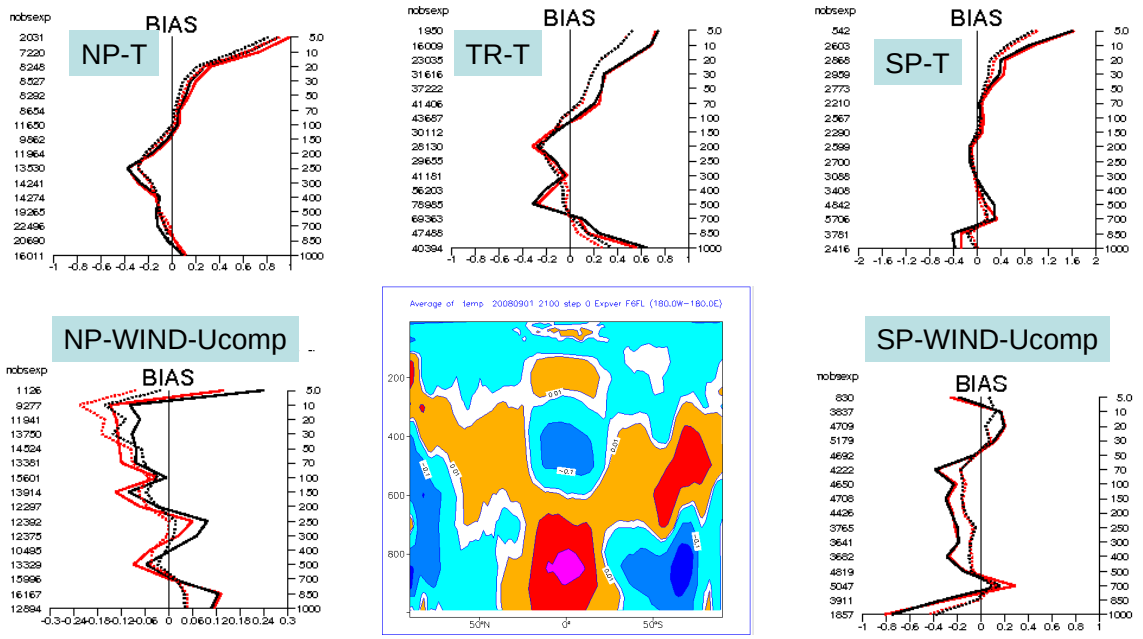

Figure 17: Zonally averaged mean analyzed temperature when IASI is added to the baseline system. Contours are at 0.01,0.05,0.1 and 0.25 K. Positive values (red and yellow) mean that adding the instruments makes the analyses warmer. Fit to radiosonde temperature iand wind data for the baseline (black) and the IASI system (red).

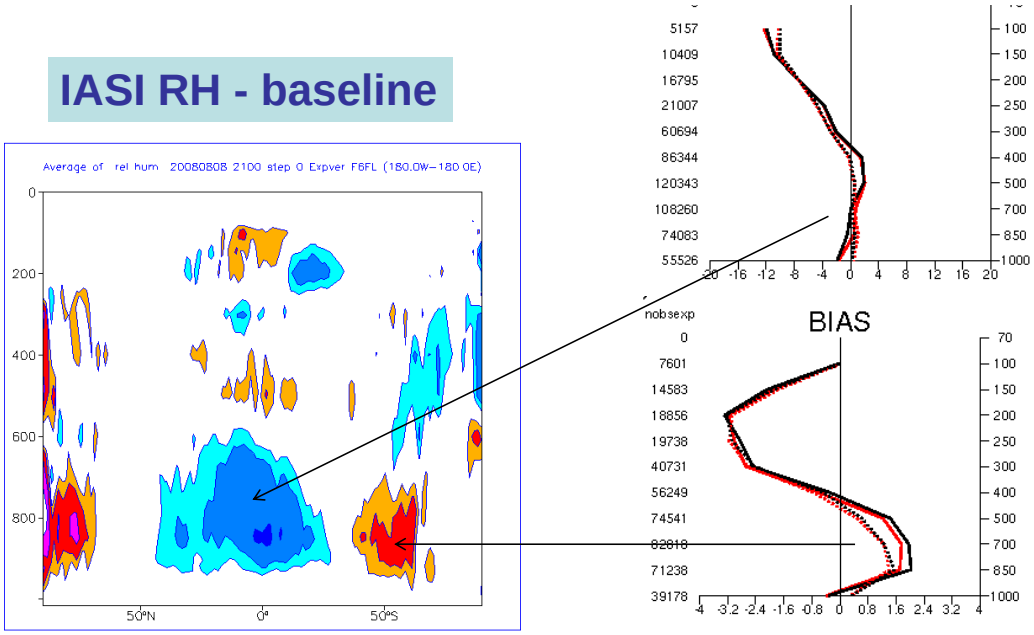

Figure 18: Zonally averaged mean analyzed relative humidity differences when IASI is added to the baseline system. Contours are at 0.5,1.0,2.0 and 5.0 %. Positive values (red and yellow) mean that adding the instruments makes the analyses wetter. Fit to radiosonde relative humidity data for the baseline (black) and the IASI system (red).

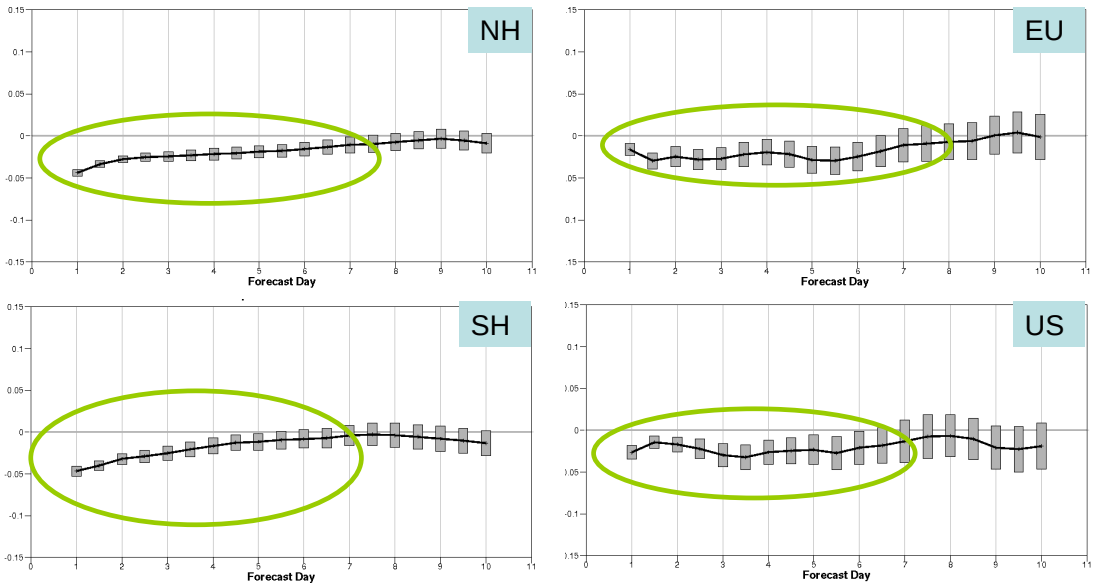

Figure 19: Annually averaged reduction in normalized RMS error for 500 hPa geopotential forecasts when AIRS data are added to the baseline system for the Northern Hemisphere (NH), the Southern Hemisphere (SH), the European region (EU) and the North American region (US). Vertical error bars indicate 95 % confidence intervals.

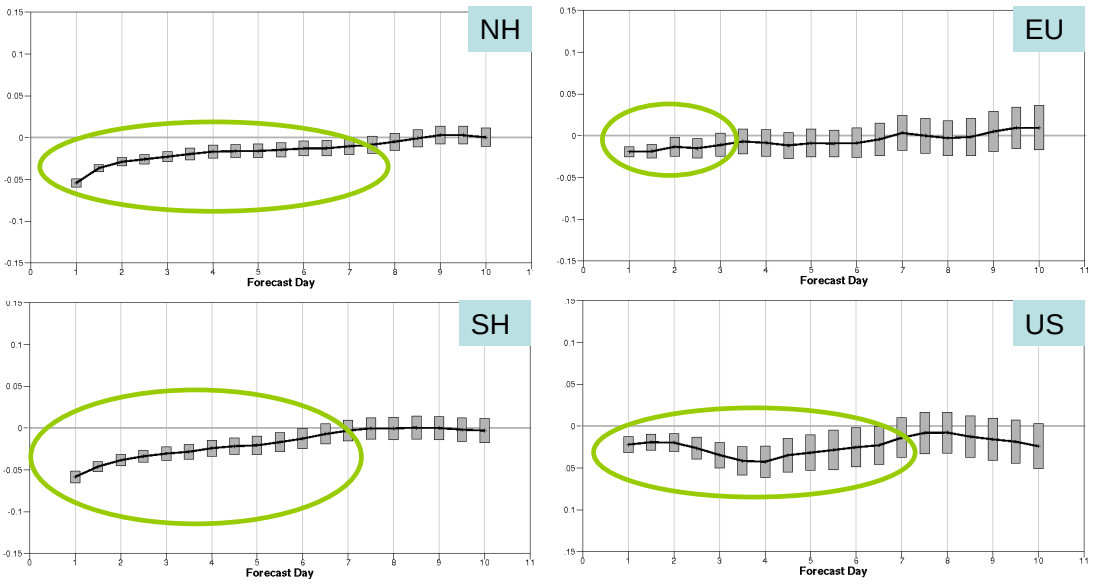

Figure 20: Annually averaged reduction in normalized RMS error for 500 hPa geopotential forecasts when IASI data are added to the baseline system for the Northern Hemisphere (NH), the Southern Hemisphere (SH), the European region (EU) and the North American region (US). Vertical error bars indicate 95 % confidence intervals.

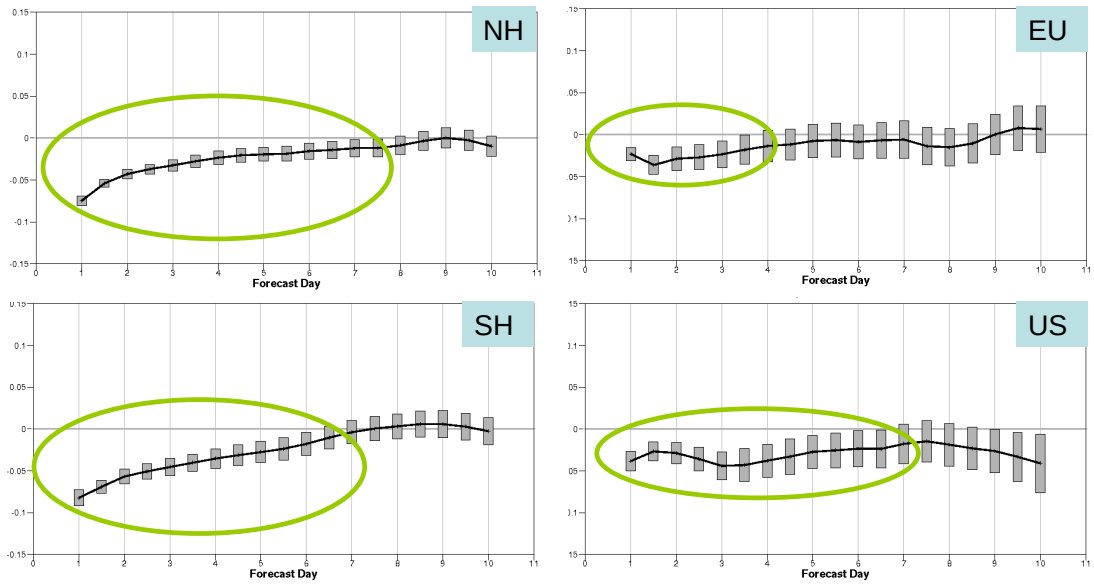

Figure 21: Annually averaged reduction in normalized RMS error for 500 hPa geopotential forecasts when AIRS and IASI data are added to the baseline system for the Northern Hemisphere (NH), the Southern Hemisphere (SH), the European region (EU) and the North American region (US). Vertical error bars indicate 95 % confidence intervals.

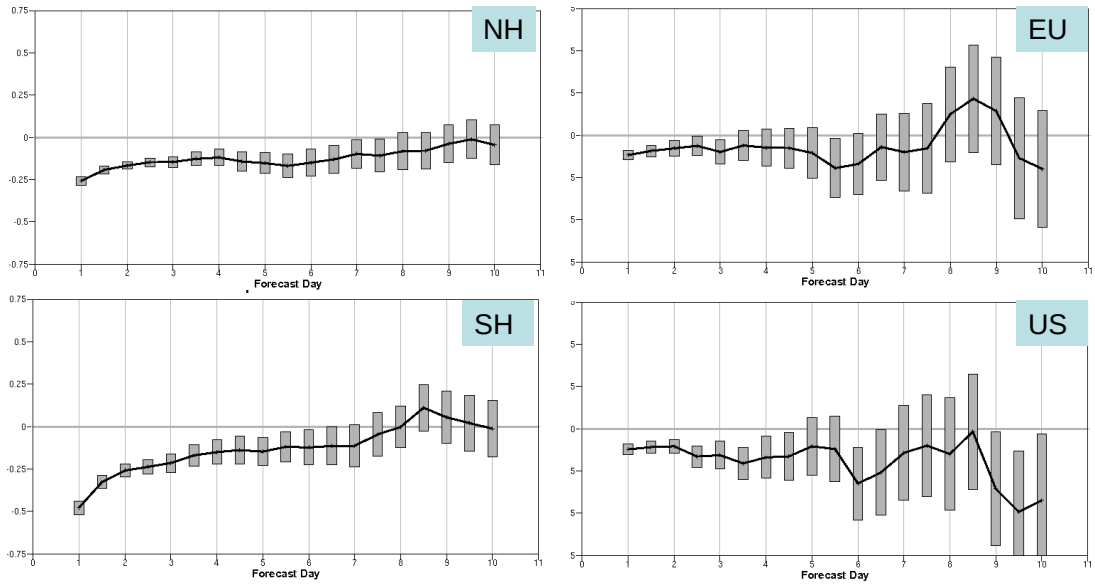

Figure 22: Annually averaged reduction in normalized RMS error for 850 hPa relative humidity forecasts when AIRS data are added to the baseline system for the Northern Hemisphere (NH), the Southern Hemisphere (SH), the European region (EU) and the North American region (US). Vertical error bars indicate 95 % confidence intervals.

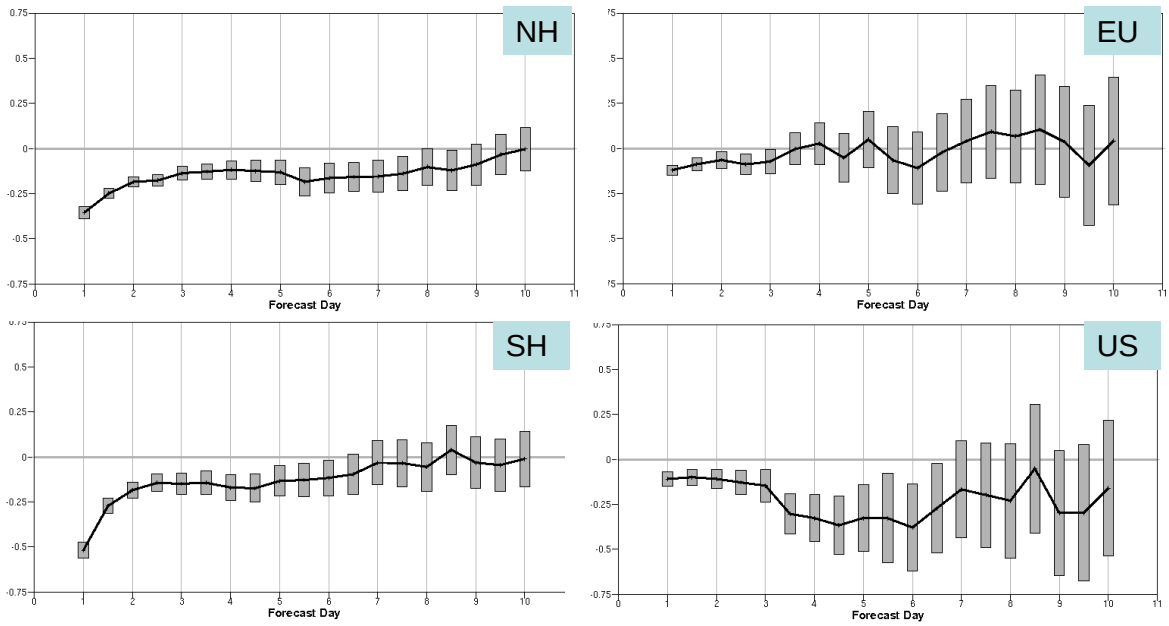

Figure 23: Annually averaged reduction in normalized RMS error for 850 hPa relative humidity forecasts when IASI data are added to the baseline system for the Northern Hemisphere (NH), the Southern Hemisphere (SH), the European region (EU) and the North American region (US). Vertical error bars indicate 95 % confidence intervals.

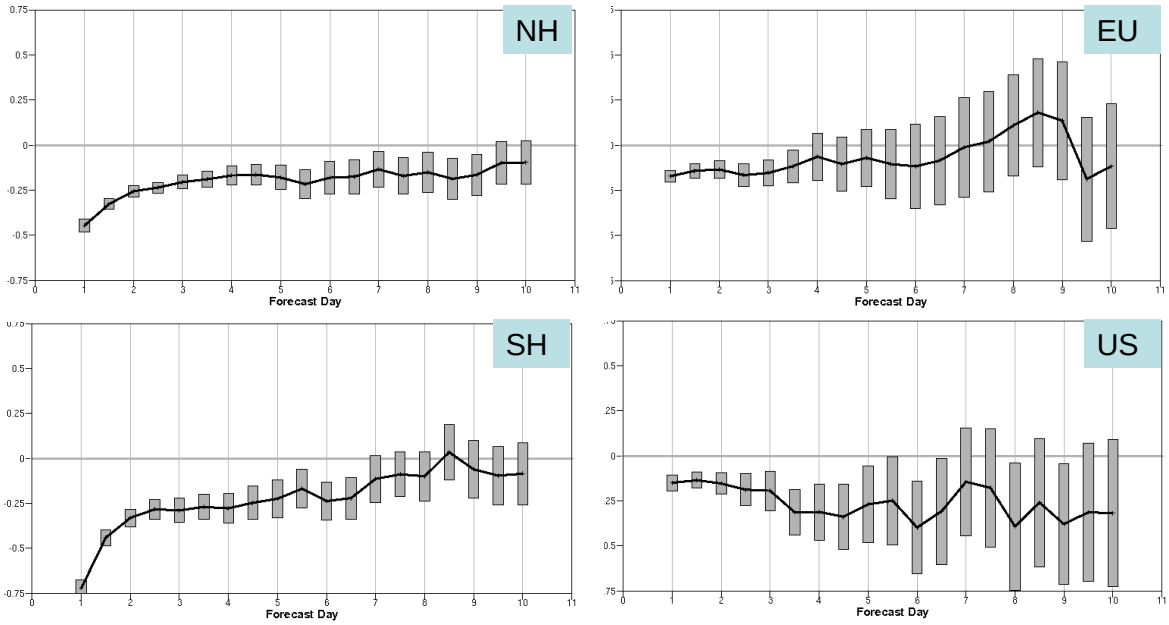

Figure 24: Annually averaged reduction in normalized RMS error for 850 hPa relative humidity forecasts when AIRS and IASI data are added to the baseline system for the Northern Hemisphere (NH), the Southern Hemisphere (SH), the European region (EU) and the North American region (US). Vertical error bars indicate 95 % confidence intervals.

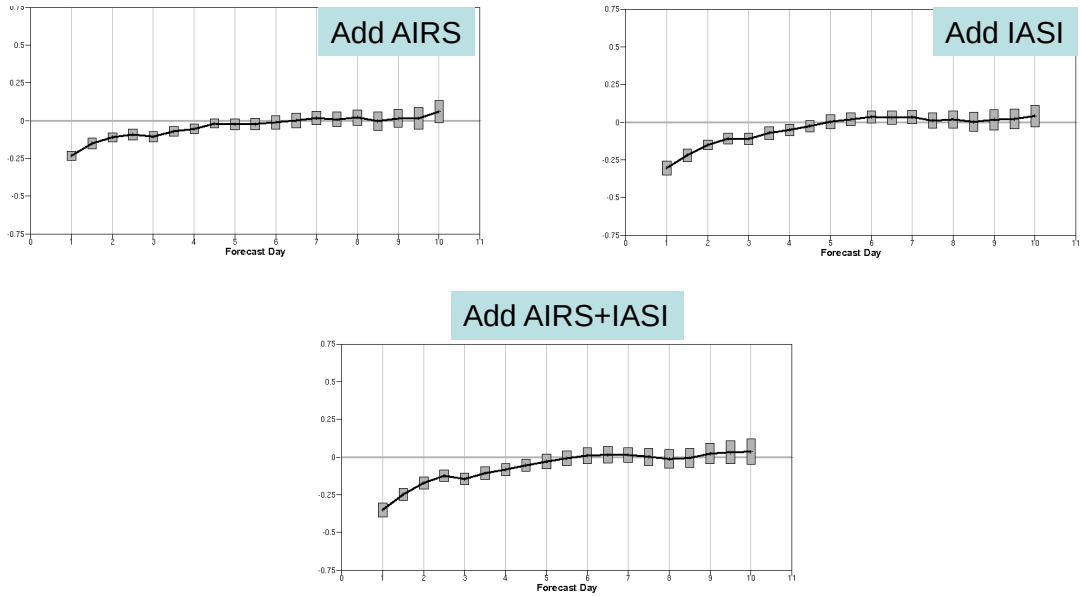

Figure 25: Annually averaged reduction in normalized RMS error for 850 hPa relative humidity forecasts when AIRS, IASI, and both data are added to the baseline system for the tropical region. Vertical error bars indicate 95 % confidence intervals.

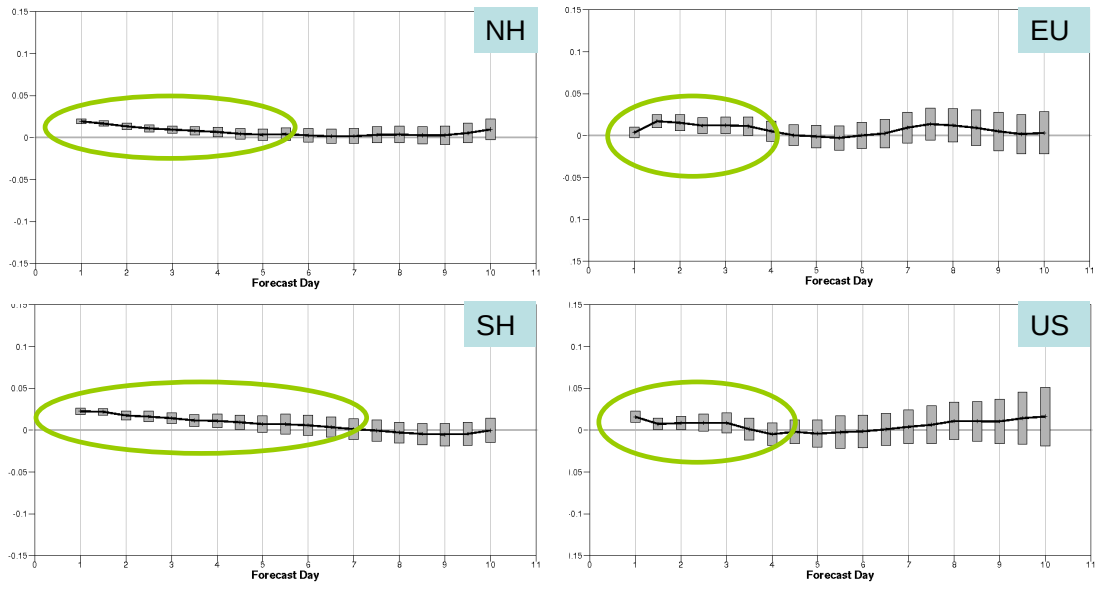

Figure 26: Annually averaged increase in normalized RMS error for 500 hPa geopotential forecasts when AIRS data are denied from the control system for the Northern Hemisphere (NH), the Southern Hemisphere (SH), the European region (EU) and the North American region (US). Vertical error bars indicate 95 % confidence intervals.

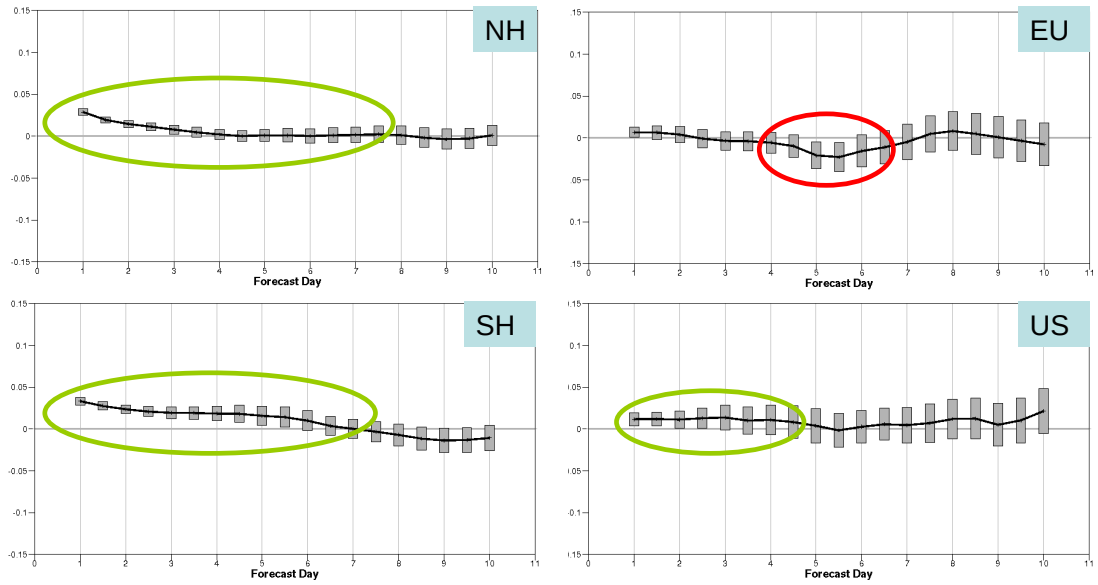

Figure 27: Annually averaged increase in normalized RMS error for 500 hPa geopotential forecasts when IASI data are denied from the control system for the Northern Hemisphere (NH), the Southern Hemisphere (SH), the European region (EU) and the North American region (US). Vertical error bars indicate 95 % confidence intervals.

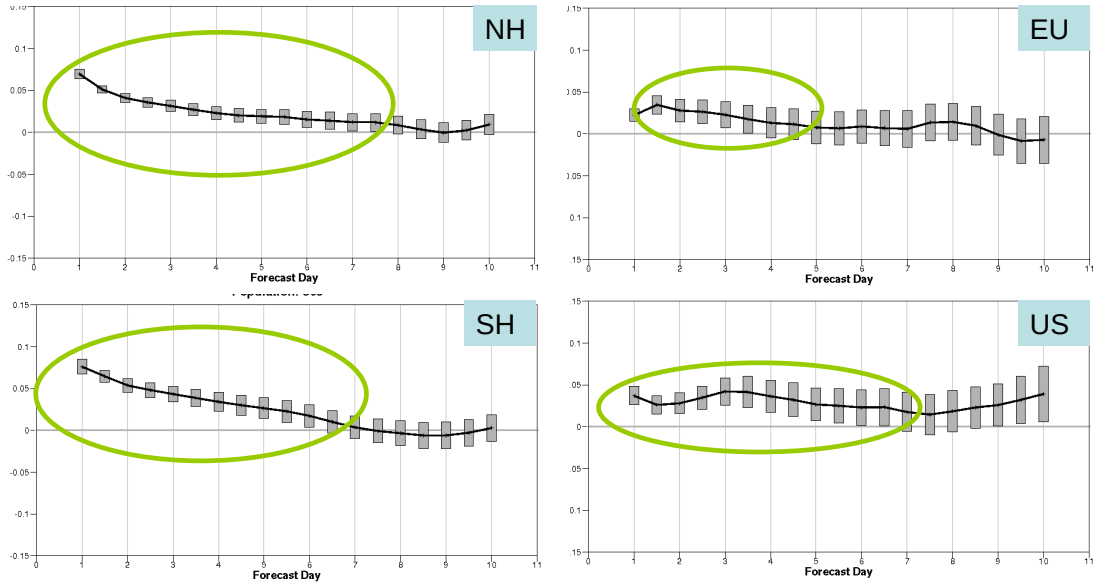

Figure 28: Annually averaged increase in normalized RMS error for 500 hPa geopotential forecasts when AIRS and IASI data are denied from the control system for the Northern Hemisphere (NH), the Southern Hemisphere (SH), the European region (EU) and the North American region (US). Vertical error bars indicate 95 % confidence intervals.

5.1.3 Advanced diagnostics

The distribution of relative 24-hour forecast error contribution (FEC) of the different observation types has been calculated from two experiments, namely the control and the AMSU-A/MHS denial experiment. Figure 29 shows the results that have been derived from 40 consecutive analyses in June 2009. The figure shows that IASI, AIRS and AMSU-A radiances contribute the most to the FEC, followed by radiosonde and aircraft observations as well as GPSRO. The AMSU-A/MHS denial experiment still shows FEC from AMSU-A since AQUA AMSU-A radiances of satellite AQUA remained in the system (Section 4.4.1). An important result is the apparent redistribution of FEC among the remaining instruments once AMSU-A and MHS have been withdrawn. Those observation types most sensitive to atmospheric temperature receive the largest additional FEC in this case indicating the strong contribution of temperature to the forecast error norm applied by FEC.

Single channels have been selected to illustrate the geographical distribution of the observation influence in the analysis (OIA) and FEC of both conventional and advanced sounders:

- Mid-tropospheric temperature: IASI channel 272, AIRS channel 221, AMSU-A channels 5-6, HIRS channel 5-6.
- Lower stratospheric temperature: IASI channel 179, AIRS channel 168, AMSU-A channel 10.
- Upper tropospheric humidity: IASI channel 2889, AIRS channel 1740, MHS channel 3, HIRS channel 12.

Figure 30 shows the maps for the mean (a) and the standard deviation (c) of OIA as well as mean (b) and the standard deviation (d) of FEC (right) for IASI channel 272. The statistics have been derived from the 4D-Var analyses of the control experiment for June 2009. The OAI map clearly indicates maximum sensitive areas over Southern hemispheric sea-ice coverage and over deep convection in the most intense Inter-Tropical Convergence Zone (ITCZ) and the Indian Ocean monsoon and a belt of moderate influence over Southern mid-latitude oceans. The convectively active areas and the Southern oceans are also the regions with the strongest OIA variability. Since the observation errors are constant for all radiance data used in the system, the spatial patterns are the result of the background error definition and the sensitivity of the model/observation operator to observation perturbations.

The sea-ice covered areas are spatially and temporally rather stable during a month and this is also shown by the small standard deviations of OIA in this are in Figure 30c. The large mean OIA values are most likely the result of the increased surface emission (skin temperature and emissivity) background errors and the fact that this IASI channel is sensitive to the surface. The tropical patterns are more likely related to the model/operator's sensitivity to the observation since small perturbations can produce a large impact in the analysis.

The observations have a positive mean influence on the forecast if the mean FEC value is negative (blue on the figure). Interestingly, both structures of large OIA are not seen in the FEC suggesting that the forecast does not maintain the information introduced by this channel in the initial conditions. However, the dark blue pattern over the Southern oceans showing positive impact (negative FEC) (Figure 30b) is similar to the areas of moderate OIA (Figure 30a). Here, the combination of larger background errors in mid-latitude storm tracks and the sensitivity of the model/observation operator to the observation produces noticeable analysis and forecast impact. The latter, however, shows significant spatial variability in the mean fields but the FEC standard deviations (Figure 30d) clearly highlight these areas.

Maps of mean FEC for AMSU-A channels 5 and 6 are shown in Figure 32. These two tropospheric temperature channels show very similar geographical distribution of FEC. The observations have the largest positive forecast impact over the Southern hemispheric oceans but both channels indicate a positive impact over a large area of Africa as well where little tropospheric temperature information is available from other (conventional) observations.

The mean OIA for tropospheric temperature sounding HIRS channels 5 and 6 show a very similar sensitivity pattern as IASI channel 272, i.e. high sensitivities in the ITCZ and monsoon areas over Antarctic sea-ice (Figure 33). Finally, tropospheric temperature AIRS channel 221 shows large OIA only over Southern oceans and the FEC is very similar to that of IASI channel 272 (not shown).

For the lower stratospheric temperature channels it is interesting to compare the OIA maps of AIRS channel 168 and IASI channel 179 (Figure 34). The patterns are very similar showing maximum values over the Southern hemispheric oceans during austral winter and more localized spots of large OIA over the central North Atlantic and Pacific. The corresponding FEC maps are again spatially more variable but also indicate a larger impact over the Southern hemisphere (not shown).

For the mid-to-upper tropospheric humidity channels Figure 35 shows the mean OIA maps, i.e. AIRS channel 1740 (top left; sensitivity peak near 300 hPa), IASI channel 2889 (top right; sensitivity peak near 600 hPa), HIRS channel 12 (bottom left; sensitivity peak near 300 hPa) and MHS channel 3 (bottom right; sensitivity peak near 300 hPa). The geographical distribution of the self-sensitivity with respect to the IASI humidity channel is similar to the temperature channels, i.e. high values characterize the ITCZ region, but here the area of high influence is somewhat larger than for the other channels since it peaks lower in the troposphere. The sensitive areas of OIA maps of HIRS channel-12 and MHS channel-3 are almost identical and refer to a similar peak altitude. The differences relate to the fact that Aqua (AIRS) and Metop-A (HIRS, MHS) have different orbits that produce different coverage patterns, namely the areas of systematically low OIA in the Pacific and over Africa for AIRS and similar patterns for HIRS/MHS over the Atlantic and Australia/Asia. Sensitivity is generally larger for observations near the end of the assimilation window so that these features emerge despite full global coverage by a sensor over 24 hours.

Mean maps of first guess and analysis (not show here) departures for HIRS channel 12 and AIRS channel 1740 show an interesting additional feature: As seen on Figure 36, the largest positive mean first-guess departures for these humidity sensitive channels largely coincide with the highest OIA areas of temperature channels (see e.g. the similarity of the Figure 36b and Figure 30a). This suggests that the systematic difference between model and observations in higher tropospheric humidity channels point at regions with high sensitivity of the analysis to both humidity and temperature channel observations.

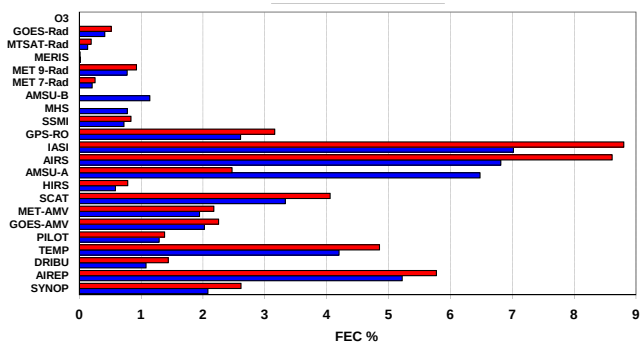

Figure 29: Distribution of relative forecast error contribution (FEC in %) due to different observational data sources in control experiment (blue bars), and AMSU-A/MHS denial experiment (red bars).

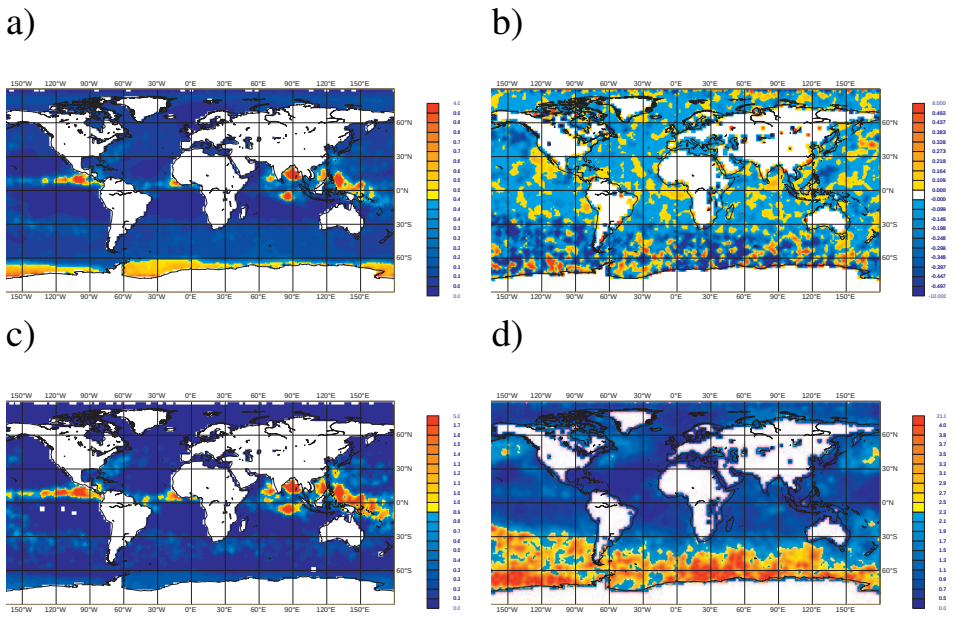

Figure 30: Maps of mean OIA (a), mean FEC (b), standard deviation of OIA (c) and standard deviation of FEC (d) derived from the control experiment for June 2009 and for IASI channel 272. Statistics are displayed for 1-degree grid boxes.

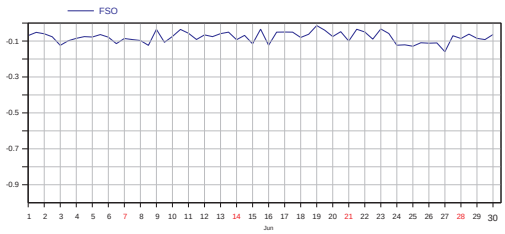

Figure 31: Time series of globally averaged FEC for IASI channel 272.

a)

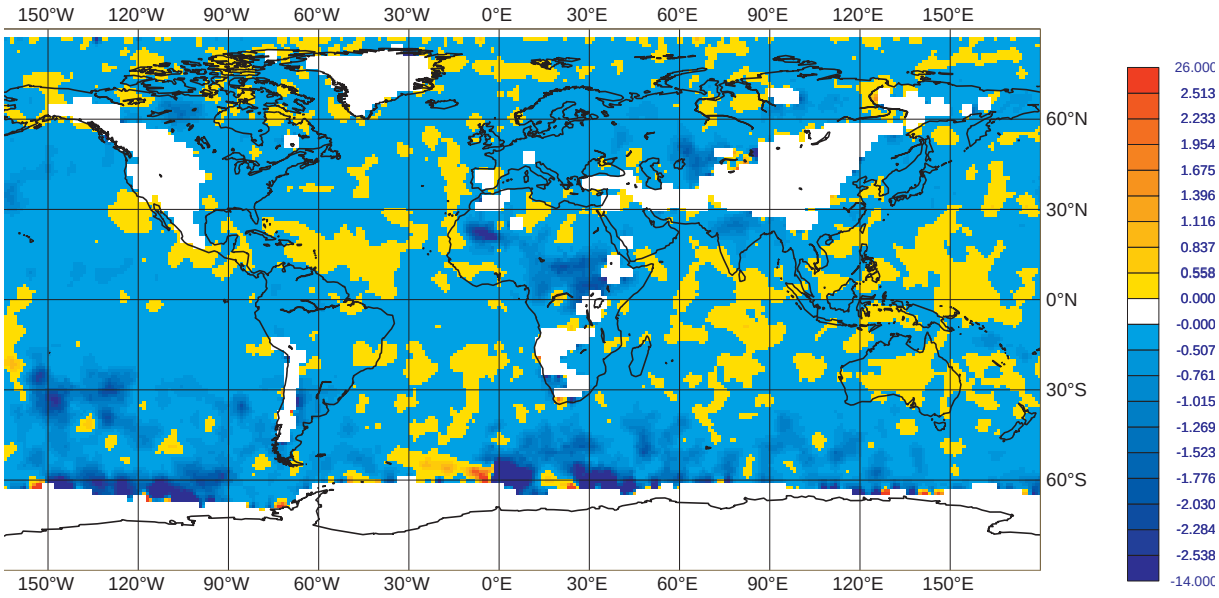

b)

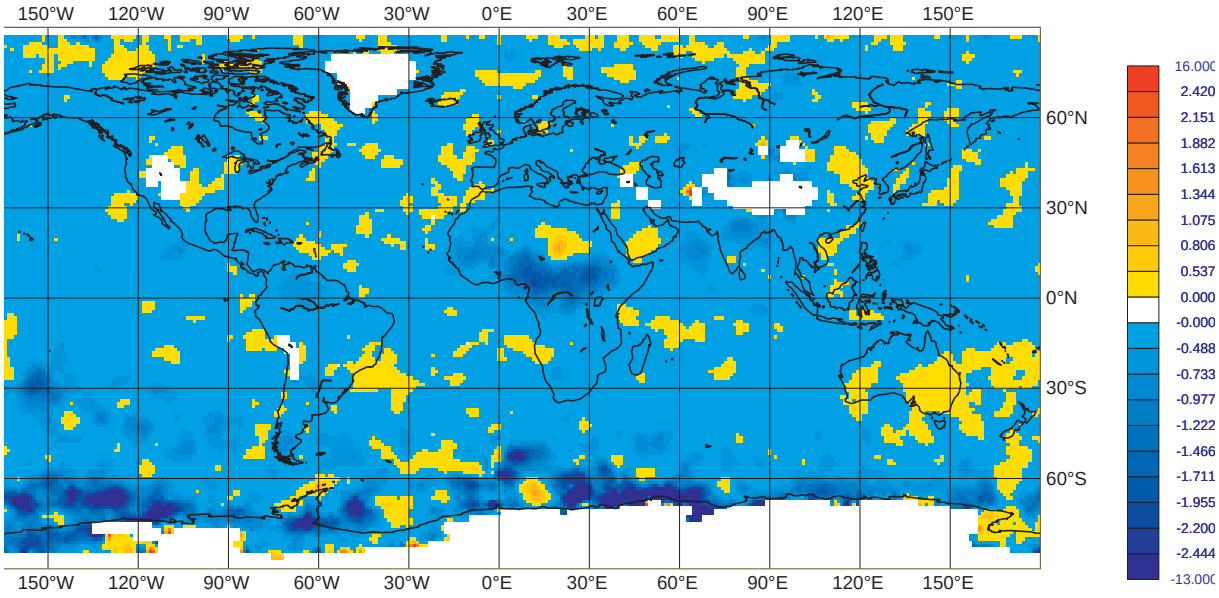

Figure 32: Maps of mean FEC for AMSU-A channel 5 (a) and channel 6 (b) derived from the control experiment for June 2009.Statistics are displayed for 1-degree grid boxes.

a)

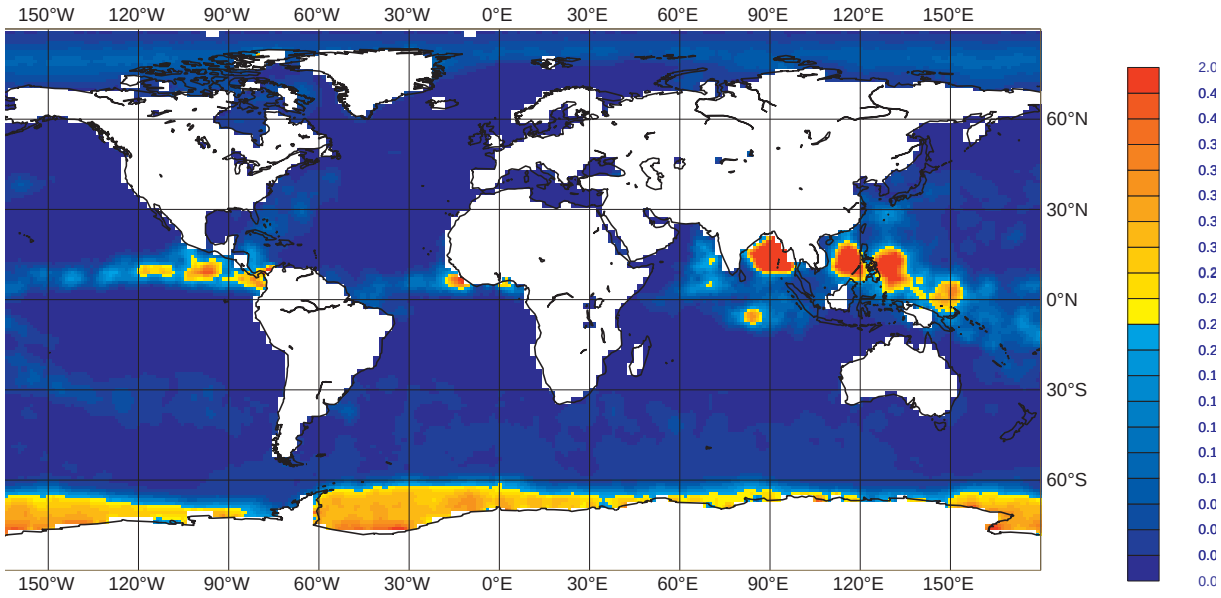

b)

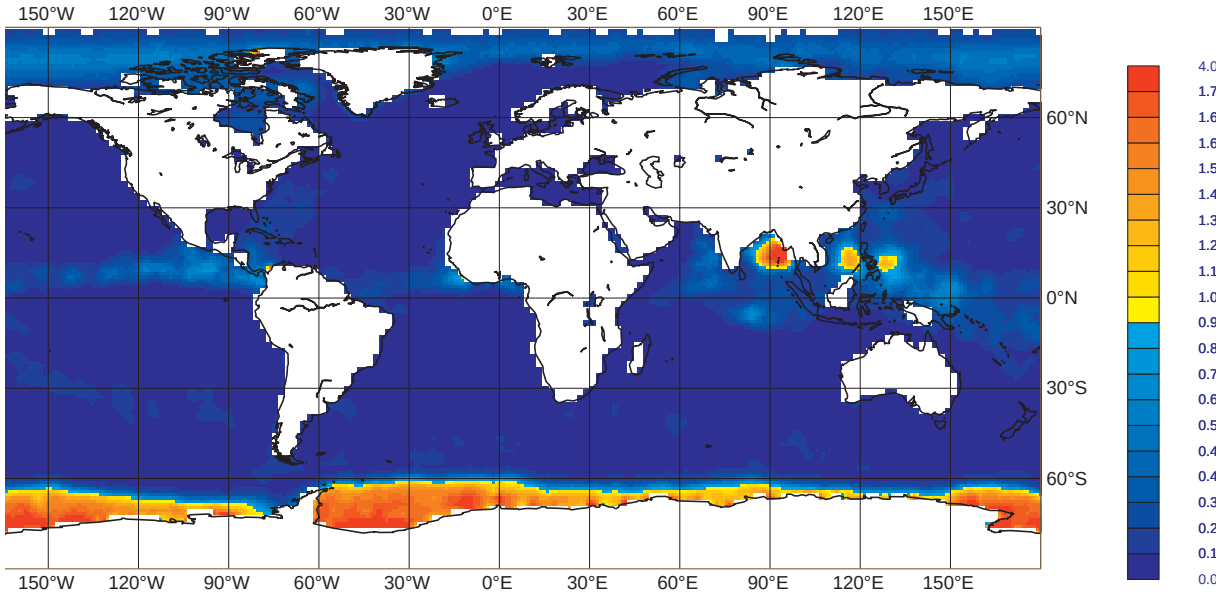

Figure 33: Map of mean OIA for HIRS channel 5 (a) and channel 6 (b) derived from the control experiment for June 2009. Statistics are displayed for 1-degree grid boxes.

a)

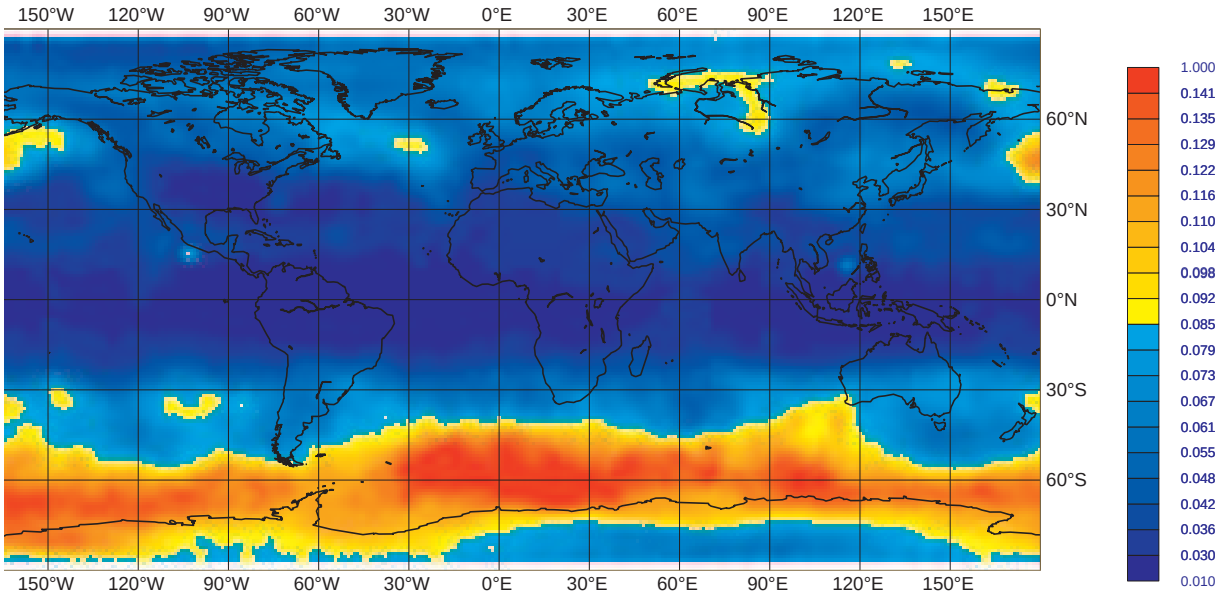

b)

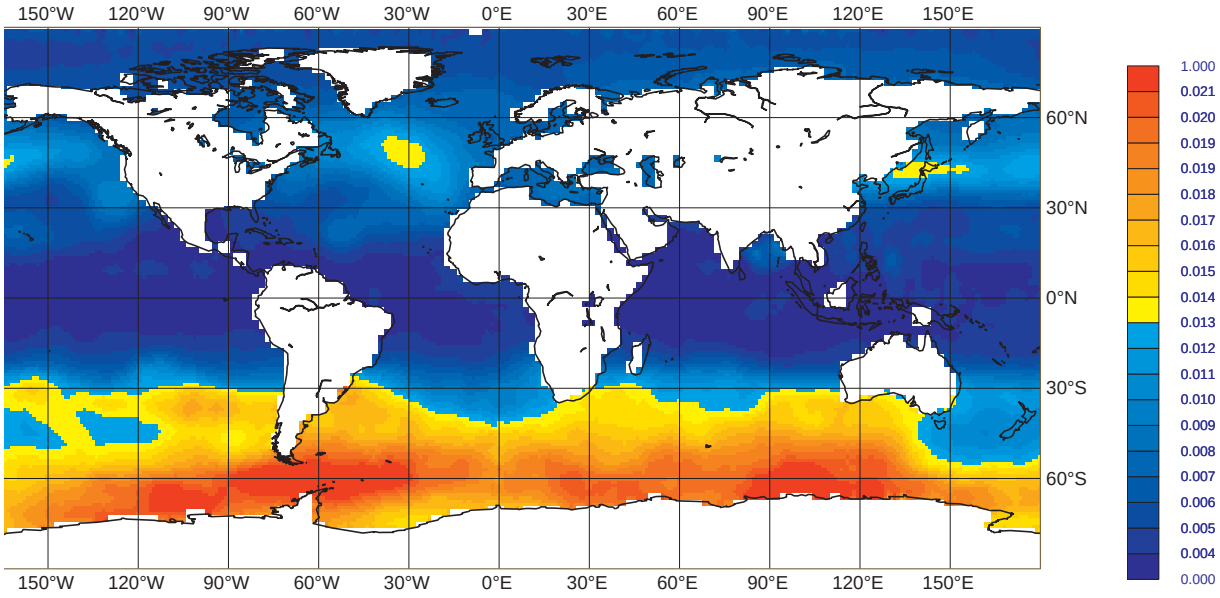

Figure 34: Maps of mean OIA for AIRS channel 168 (a) and IASI channel 179 (b) derived from the control experiment for June 2009. Statistics are displayed for 1-degree grid boxes.

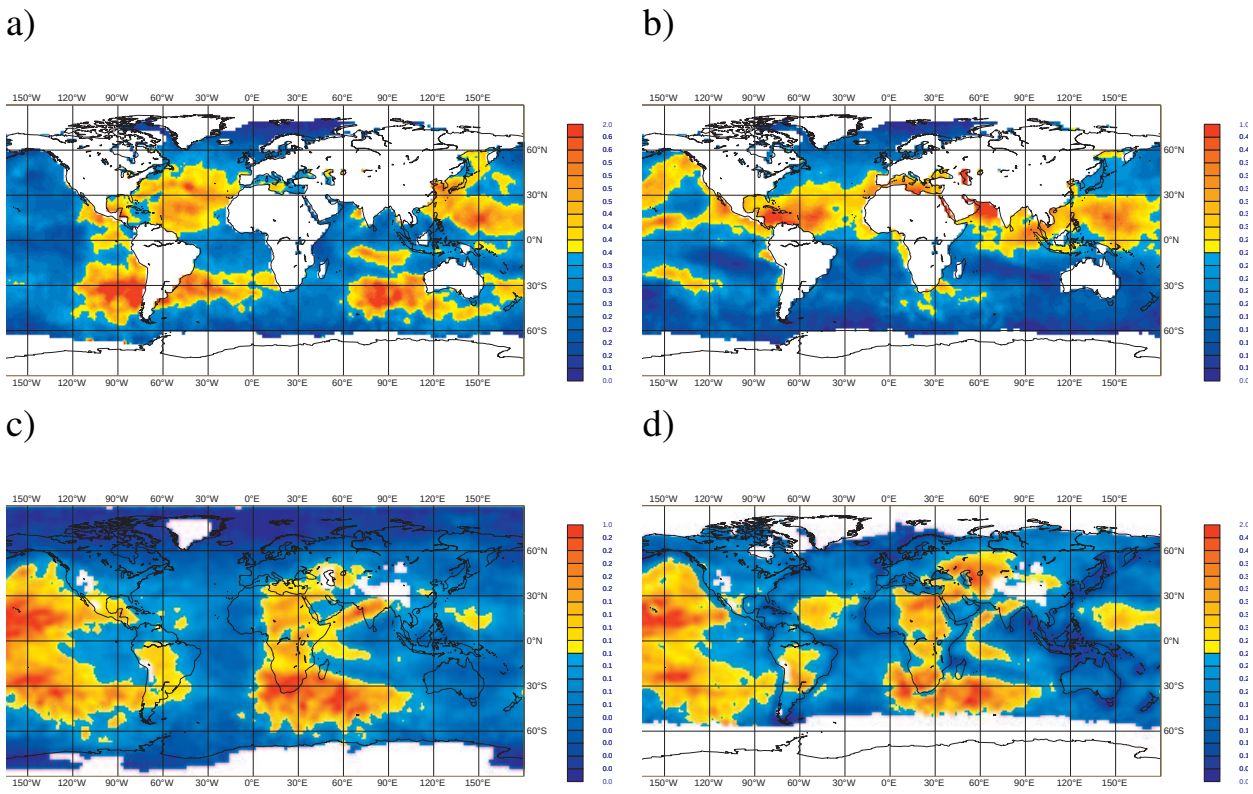

Figure 35: Maps of mean OIA for AIRS channel 1740 (a), IASI channel 2889 (b), HIRS channel 12 (c) and MHS channel 3 (d) derived from the control experiment for June 2009. Statistics are displayed for 1-degree grid boxes.

a)

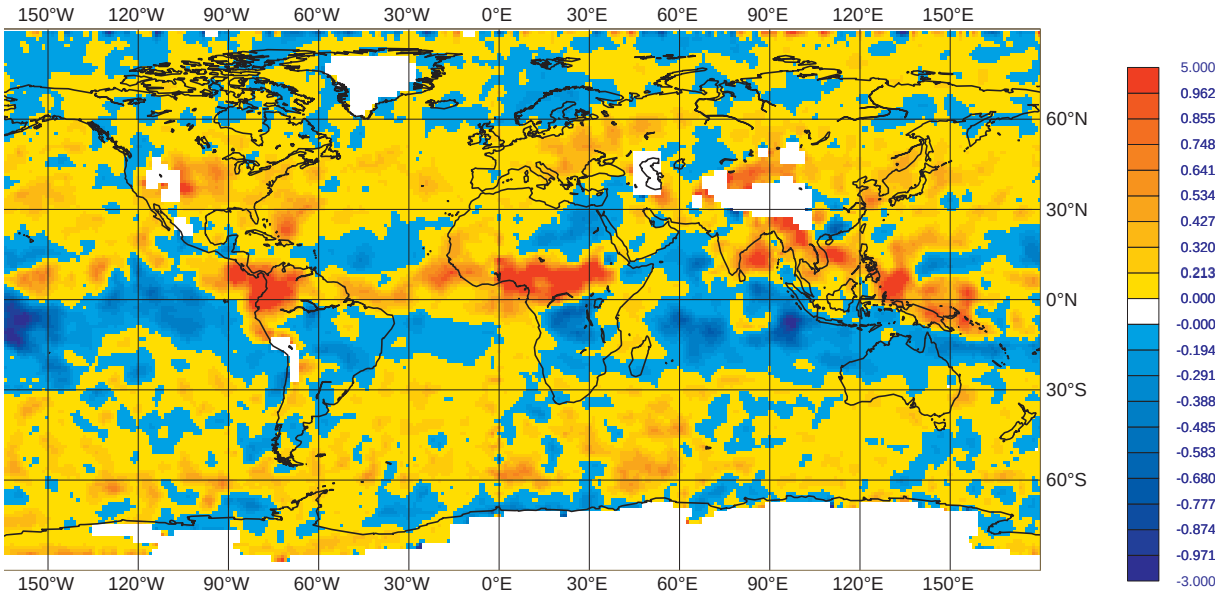

b)

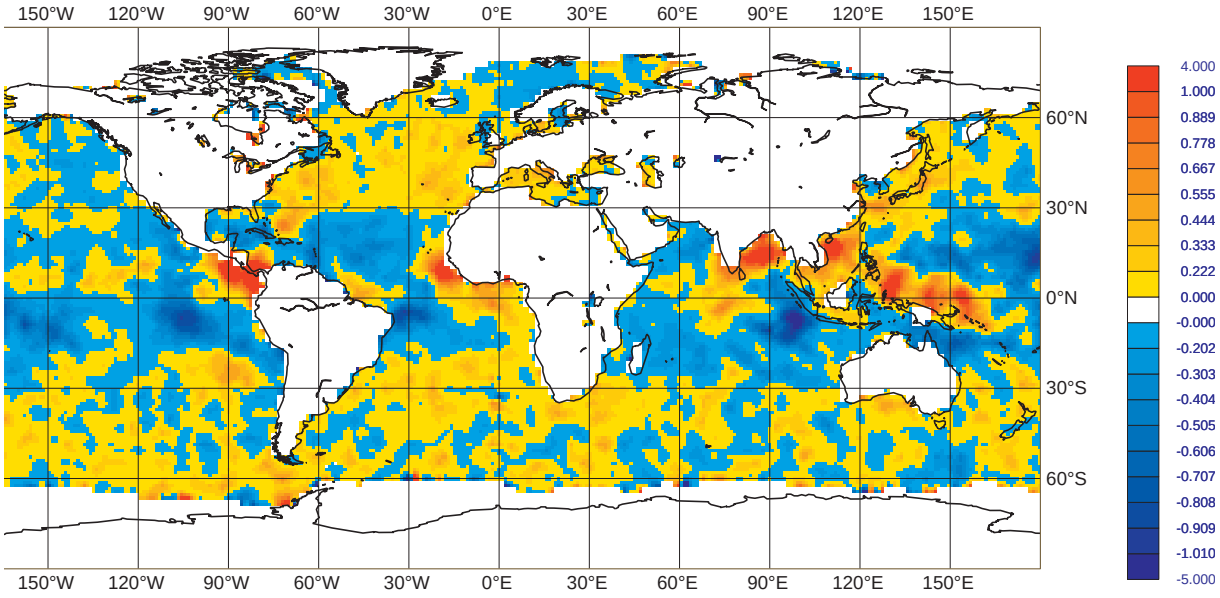

Figure 36: Maps of mean first-guess departures for HIRS channel 12 (a) and AIRS channel 1740 (b) derived from the control experiment for June 2009. Statistics are displayed for 1-degree grid boxes.

Summary

The impact of AIRS and IASI used either separately or together is significant over this extended one-year test period. The benefit of adding these instruments to a baseline can be seen in the improved fit of the analysis to conventional observations and a reduction of forecast errors out to the medium-range. Degraded forecasts result when the instruments are withheld, although the presence of one sounder is partially able to compensate for the loss of the other. These studies confirm and consolidate other impact experiments (performed at ECMWF and other centres) which collectively demonstrate that the information brought by advanced infrared sounders is crucial.

The one anomalous result that requires further investigation is the poor impact of IASI upon medium-range forecasts over the European region. In addition experiments the performance was only neutral. In denial experiments the removal of IASI actually reduced forecast errors. In contrast, results for AIRS over Europe were positive in both contexts. From the analysis diagnostics the only obvious difference between AIRS and IASI is in the low-level temperature (and humidity) at high northern latitudes and the enhanced large-scale north-south gradient (possibly responsible for the degraded fit to high latitude radiosonde wind data). However, investigations performed so far have been unable to confirm that this is in any way responsible for the degraded European forecasts. It should be noted that a poor performance over Europe was not evident in any of the pre-operational tests that were carried out on IASI in the past (indeed European scores were significantly improved when IASI was first used). The understanding of this problem remains a priority.

Adjoint diagnostic techniques demonstrate that a substantial fraction of the observational influence in the analysis is driven by the variability of the model background error variance distribution as well as the model's sensitivity to perturbations of the particular observation. This is, for example, evident when channels sensitive to both surface and clouds are evaluated where the contribution of large skin temperature background error variances over sea-ice produce significant contributions to the observational influence in the analysis as does the model's sensitivity to radiance perturbations in the presence of clouds in the ITCZ. Due to the small number of infrared radiance observations actively used in clouds the forecast impact, as obtained from the forecast sensitivity calculations, is small which is consistent with the results of the observing system experiments.

5.2 Cloud/precipitation imagers/sounders

Two denial experiments have been performed for this work-package and the definition of the Reference experiment as well as the examination period are the same as for the sounder experiments. The first denial experiment aimed at studying the impact of the assimilation of cloud and precipitation affected radiances in a full 4D-Var framework (Bauer et al. 2010, Geer et al. 2010). This meant in practice to deny all SSM/I radiances and ENVISAT MERIS total column water vapour retrievals (Bauer 2009).It has to be mentioned that AMSR-E and TMI radiances have been excluded already from the control so they did not have to be denied in the experiment.

In the second denial experiment the assimilation of overcast cloud-affected infrared radiances (McNally 2009) has been deactivated (in the Reference and all other experiments overcast infrared radiances have been included). In order to not include any cloud-affected radiance impact in this experiment, SSM/I data have also been removed and therefore the control experiment in this part of the study is the SSM/I denial experiment.

5.2.1 *Analysis*

The comparison of analysis and first-guess statistics of the SSM/I data denial experiment compared to the Reference shows that the assimilation of SSM/I radiances results in keeping significantly more AMSU-A radiances in the system (not shown) as a result of the improved clear-sky analysis that produces less AMSU-A data rejection. This is especially true over the Tropics for AMSU-A channels 5-8, where the difference in data usage reaches 2%. The same holds for the HIRS and AIRS data usage. The assimilation of SSM/I data improves the first-guess model fit to MHS channel 5 radiances, that is sensitive to the moisture in the mid to lower troposphere, mainly over the Tropics as seen in Figure 37 for NOAA-18 (top) and METOP (bottom).

The impact of SSM/I data on the fit of model first-guess and analysis to advanced sounder data is similar as has been shown for the AMSU-A/MHS data in Section 5.1 (compare Figures 38 and 5). Biases with respect to the assimilated IASI humidity channels are similar in the two denial experiments, but the signal is slightly weaker in the SSM/I than in the AMSU-A/MHS denial experiment. The systematic differences with respect to radiosonde humidity profiles, as seen in Figure 6b, are even more similar in the two denial experiments.

The total column water vapour mean difference maps between the SSM/I denial and Reference experiments are shown in Figure 39. As before, the average has been computed for summer (Fig. 39a) and for autumn (Fig. 39b) separately. The largest differences are in the Southern hemisphere where the denial of SSM/I increases the moisture content. This is in agreement with what has been found in the radiosonde humidity departure statistics. A similar impact of SSM/I data on the mean moisture state over the oceans has been documented by Bauer et al. (2006b) and Kelly et al. (2007).

Another feature of SSM/I radiance assimilation is its impact on near-surface wind speed because the radiances also exhibit sensitivity to surface roughness. From the observation statistics improved fits of model first-guess and analysis to QuikSCAT, ASCAT and buoy wind speed observations was found when SSM/I data was assimilated (not shown).

In the second denial experiment of this work-package the analysis and forecast impact of the infrared radiances (HIRS, AIRS and IASI) at locations that are identified as overcast has been examined. Figure 40 shows the horizontal distribution of IASI observations in a given window-channel (channel number 906, i.e. wavenumber 871.25 cm^{-1}) over a 12 hour period used in 4D-Var. Blue dots denote all assimilated data in the Reference experiment and the red dots denote those data that are identified as overcast points and therefore are missing in the clear-sky only system (where both SSM/I and overcast infrared data are denied). In this particular case there are about 3000 data points from this window-channel and 250 (i.e. 8%) of them correspond to additional overcast points. In general, channels whose weighting functions peak in the lower troposphere the overcast observations add 2-5% of data to the system.

The impact of the overcast data can be quite significant because they are located in areas where, due to the presence of clouds, systematically less sounder data is used than in clear-sky areas and because cloud-affected areas are near regions where the forecast skill is rather sensitive to the accuracy of the initial conditions (McNally 2002). The relatively large analysis impact of overcast infrared radiances can be well illustrated by the mean lower level temperature analysis difference between the clear-sky and clear-sky plus overcast radiance assimilation experiments. Figure 41 and Figure 42 show the mean 850 hPa and 700 hPa temperature differences, respectively, where systematic mean temperature differences can be identified over ocean areas with frequent stratocumulus occurrence, e.g. west of the American Continent. A dipole structure is seen where the impact of the overcast data is a warming at 700 hPa and cooling at 850 hPa. Such dipole structures are the consequence of the temperature inversion below the

clouds in conjunction with the displacement of the stratocumulus cloud top height due to the assimilation of cloudy radiances. An indication that this impact is towards improved analyses is given by the fact that the short-range forecast biases with respect to IASI temperature channels are slightly reduced when overcast infra-red radiances are assimilated as shown in Figure 43 for both Northern (top) and Southern (bottom) hemispheres.

5.2.2 Forecast

In Figure 13 and Figure 14 (Section 5.1.1), a comparison of forecast scores from the main data denial experiments has been compiled. The statistics suggested that the impact of SSM/I data is stronger than that of AMSU-A/MHS or HIRS on boundary layer temperature and for humidity, especially over the Tropics.

Figure 44 shows the corresponding zonal cross-sections of normalized RMS temperature forecast error differences between the SSM/I denial and the Reference experiments. Positive values indicate a positive impact of the SSM/I data. As mentioned, the impact of the data is strong and significantly positive over the Tropics and the Southern hemisphere mid-latitudes that reaches up to 500-700 hPa. In contrast to temperature sounders the impact of moisture sounders on temperatures and geopotential dissipates faster with increasing forecast range. Here, the impact remains significantly positive near the ground and in the Tropics for up to 2 days. Wind scores (not shown here) indicate a similar signal and humidity scores are also similar. For the latter, the positive impact is the strongest in the Tropics at 700-850 hPa as shown in Figure 45.

The impact of the overcast cloudy infrared radiance assimilation on forecast scores is generally small and, for most of the parameters/areas, it is statistically insignificant. However, for 700 hPa temperature forecasts a small but statistically significant positive impact can be identified over the Southern hemisphere when each experiment is verified against its own analysis. This is shown in Figure 46.

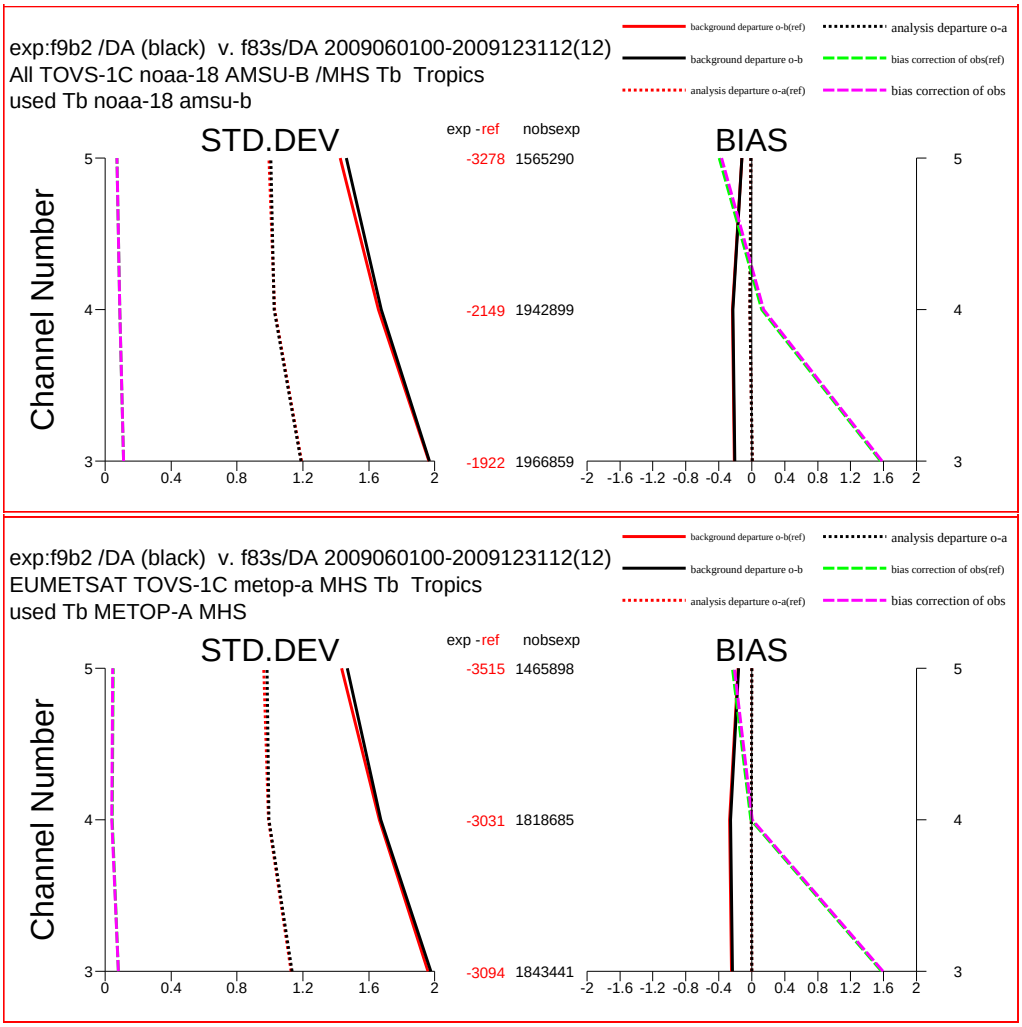

Figure 37: Fit of model first-guess (solid) and analysis (dashed) to MHS brightness temperatures for NOAA-18 (top) and METOP (bottom) in SSM/I denial (black) and Reference (red) experiments. Left panels show standard deviations, right panels show biases. Numbers in central columns denote the data sample from the denial (right, black) experiment and the difference between denial experiment and Reference (left, black or red). Green and pink curves denote bias correction from Reference and denial experiment, respectively. Statistics were generated over the Tropics from the period 01/06-31/12/2009.

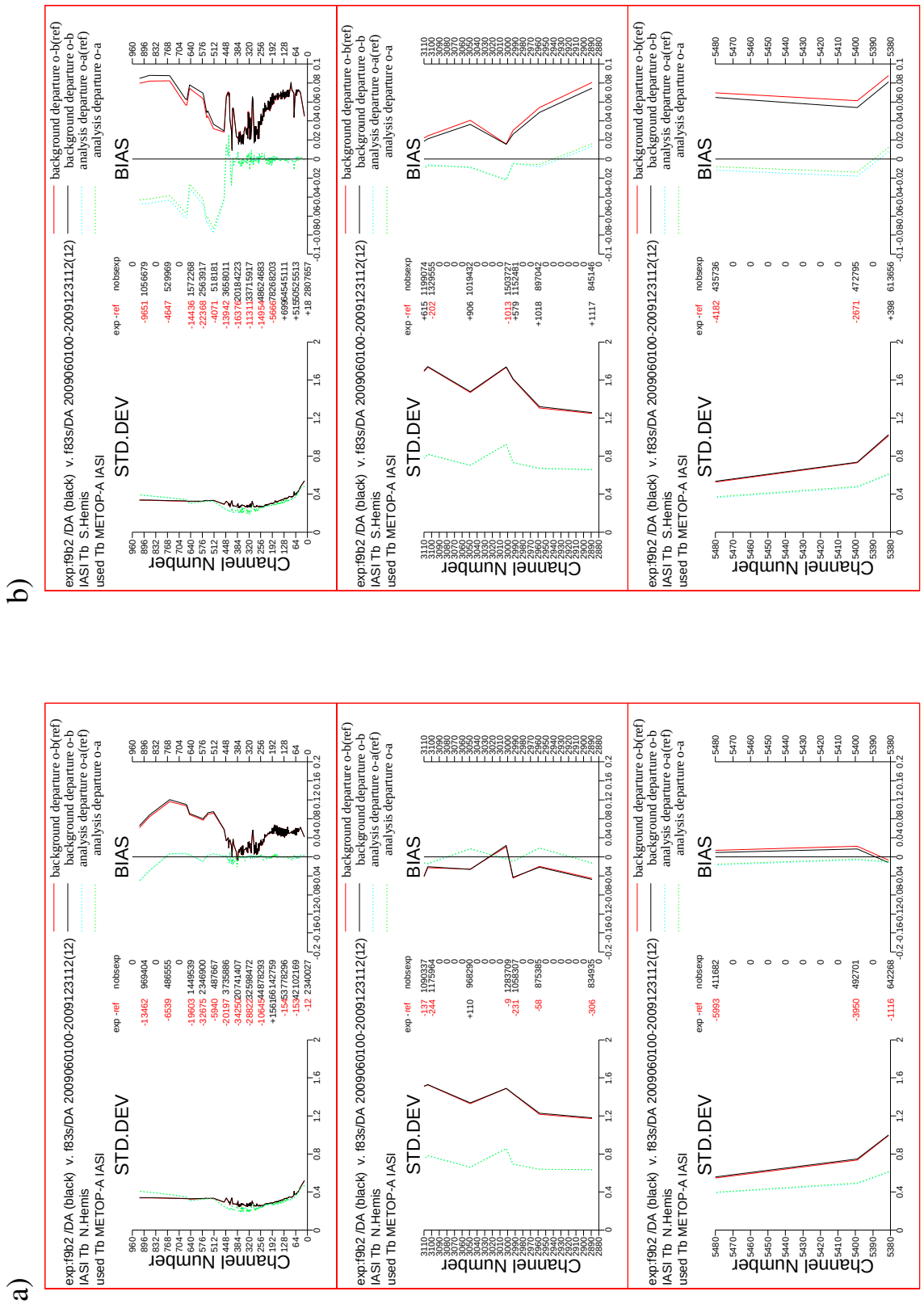

Figure 38: Fit of model first-guess (solid) and analysis (dashed) to IASI brightness temperatures for temperature channels (top), humidity channels (middle and bottom) from SSM/I denial (black) and Reference (red) experiments. Left panels show standard deviations, right panels show biases. Numbers in central columns denote the data sample from the denial (right, black) experiment and the difference between denial experiment and Reference (left, black or red). Statistics were generated from period 01/06-31/12/2009. a) shows Northern hemisphere and b) shows Southern hemisphere.

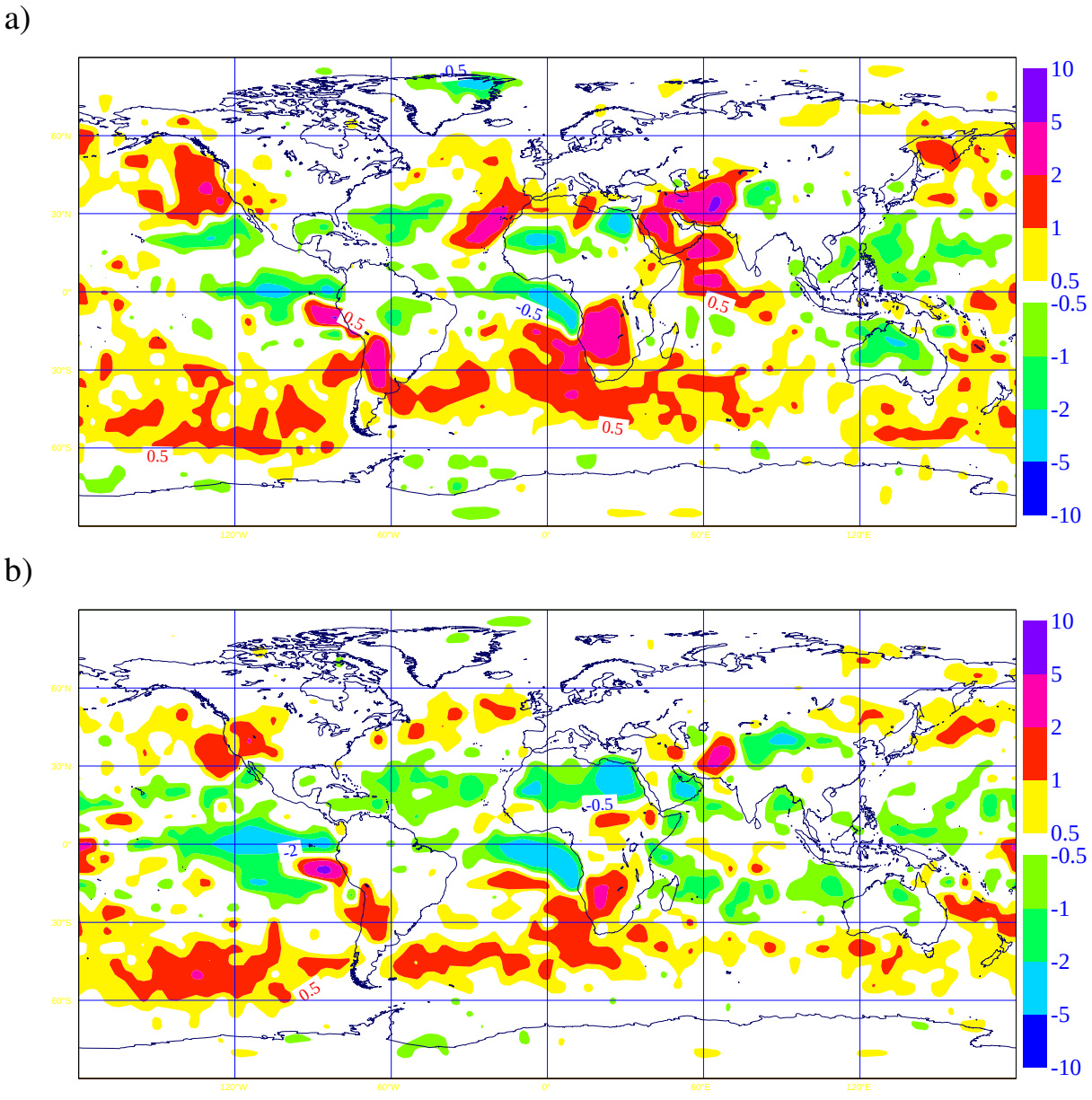

Figure 39: Normalized mean analysis difference maps of total column water vapour between the SSM/I denial and Reference experiments, where the mean has been computed for 3 months of summer (a) and autumn (b) separately. Yellow to red (green to blue) colours indicate that the denial experiment is more (less) humid.

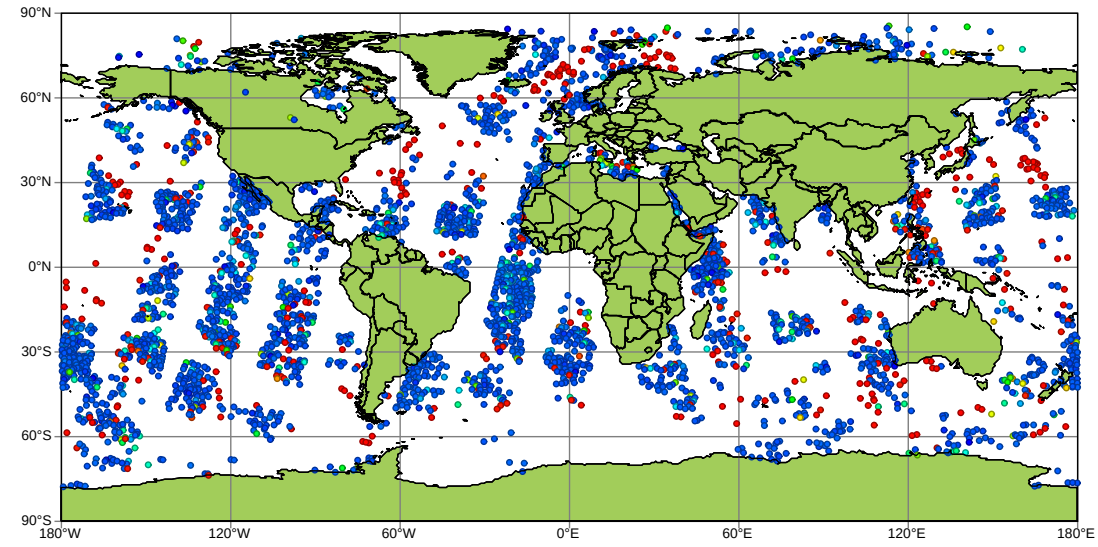

Figure 40: Horizontal distribution of all assimilated IASI window channel 906 (wavenumber 871.25 cm^{-1}) data for a given 12 hour 4D-Var assimilation window. Blue dots represent clear-sky, red points overcast data.

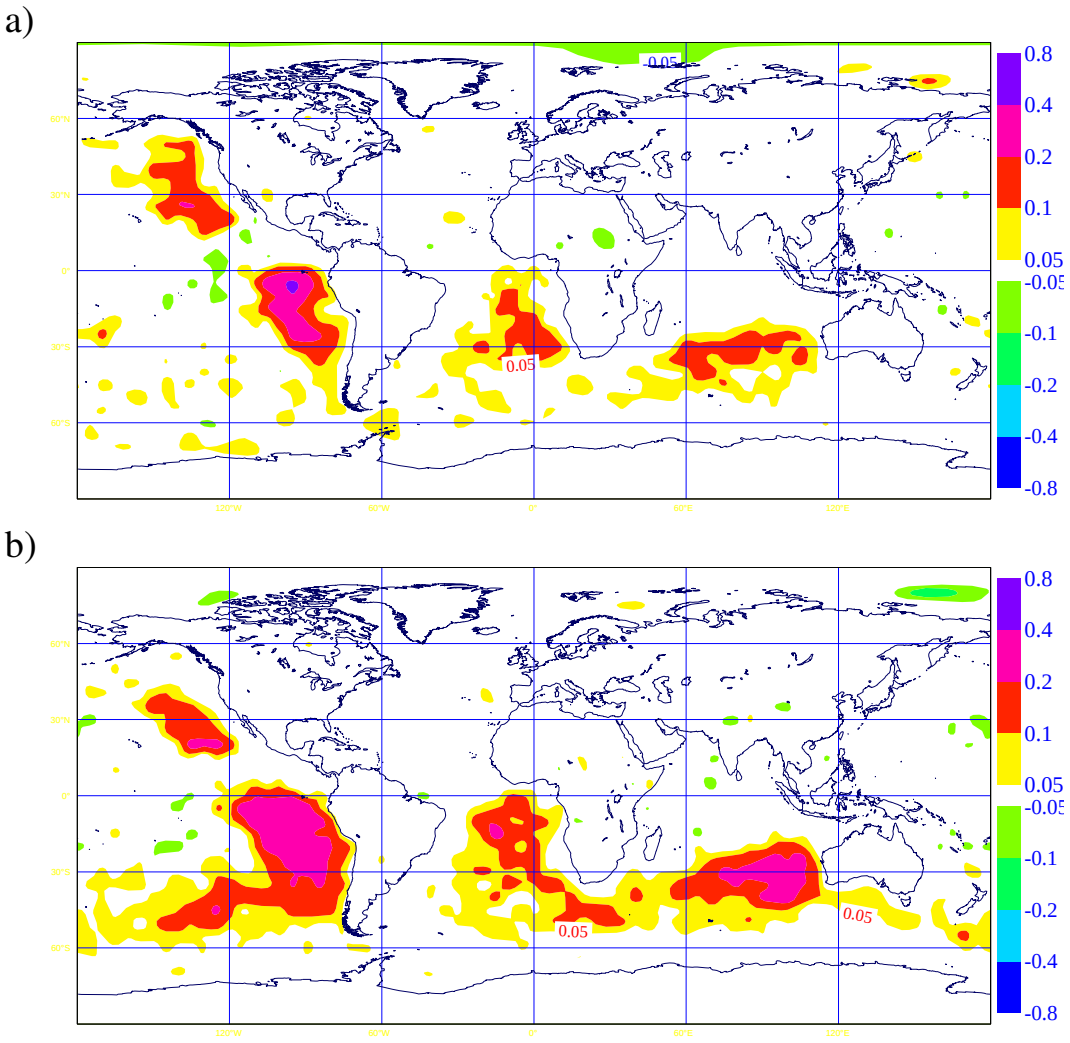

Figure 41: Mean analysis difference of 850 hPa temperature (in K) between clear-sky and clear-sky plus overcast infrared data experiments, where the average has been computed for the 3 months in summer (a) and autumn (b) separately. Yellow to red (green to blue) colours indicate that the clear-sky experiment is warmer (colder).

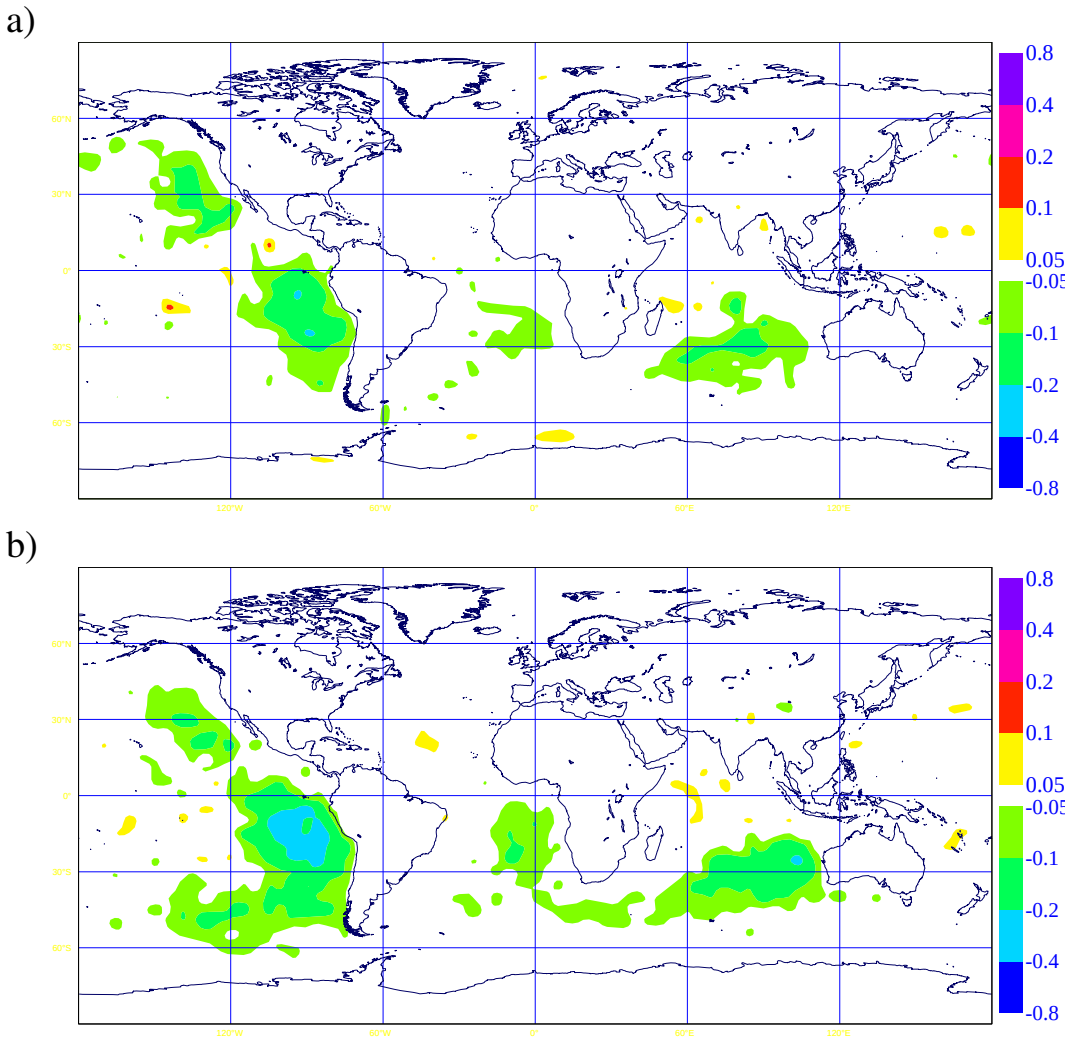

Figure 42: As Figure 41 for 700 hPa.

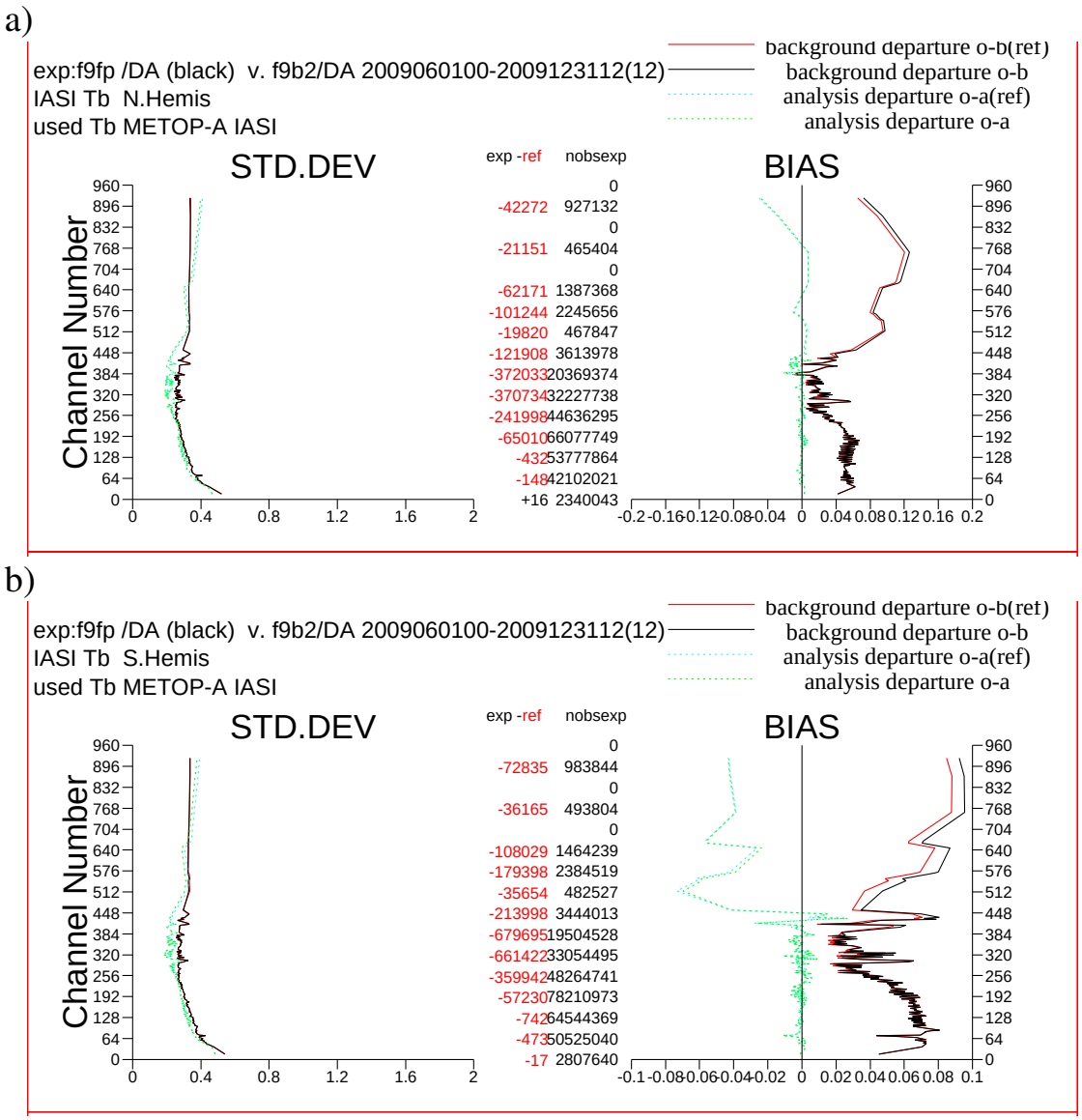

Figure 43: Fit of model first-guess (solid) and analysis (dashed) to IASI brightness temperatures for temperature channels over Northern hemisphere (a) and Southern hemisphere (b) from clear-sky (black) and clear-sky plus overcast (red) experiments. Left panels show standard deviations, right panels show biases. Numbers in central columns denote the data sample from the clear-sky (right, black) experiment and the difference between clear-sky experiment and clear-sky plus overcast (left, black or red). Statistics were generated from period 01/06-31/12/2009.

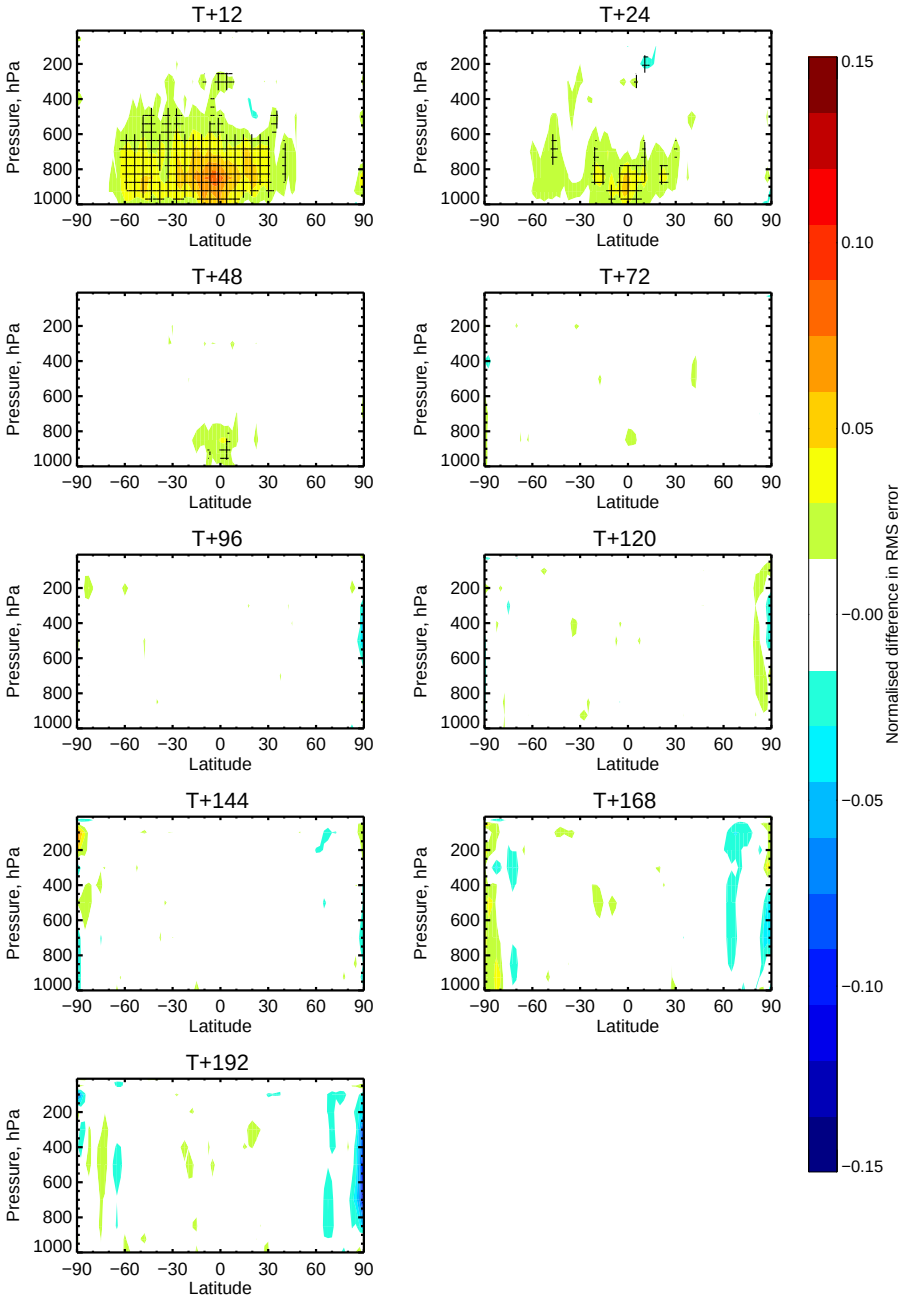

Figure 44: Zonal cross-sections of normalized RMS forecast error difference between SSM/I denial and Reference experiments for temperature. Positive values indicate positive impact of the assimilated SSM/I radiances. Panels show forecast range of 12, 24, 48, 72, 96, 120, 144, 168 and 192 hours. Crosses indicate where scores are statistically significant at the 95% level. Forecast verification is against operational analyses, verification period is 20/05/2009-31/12/2009.

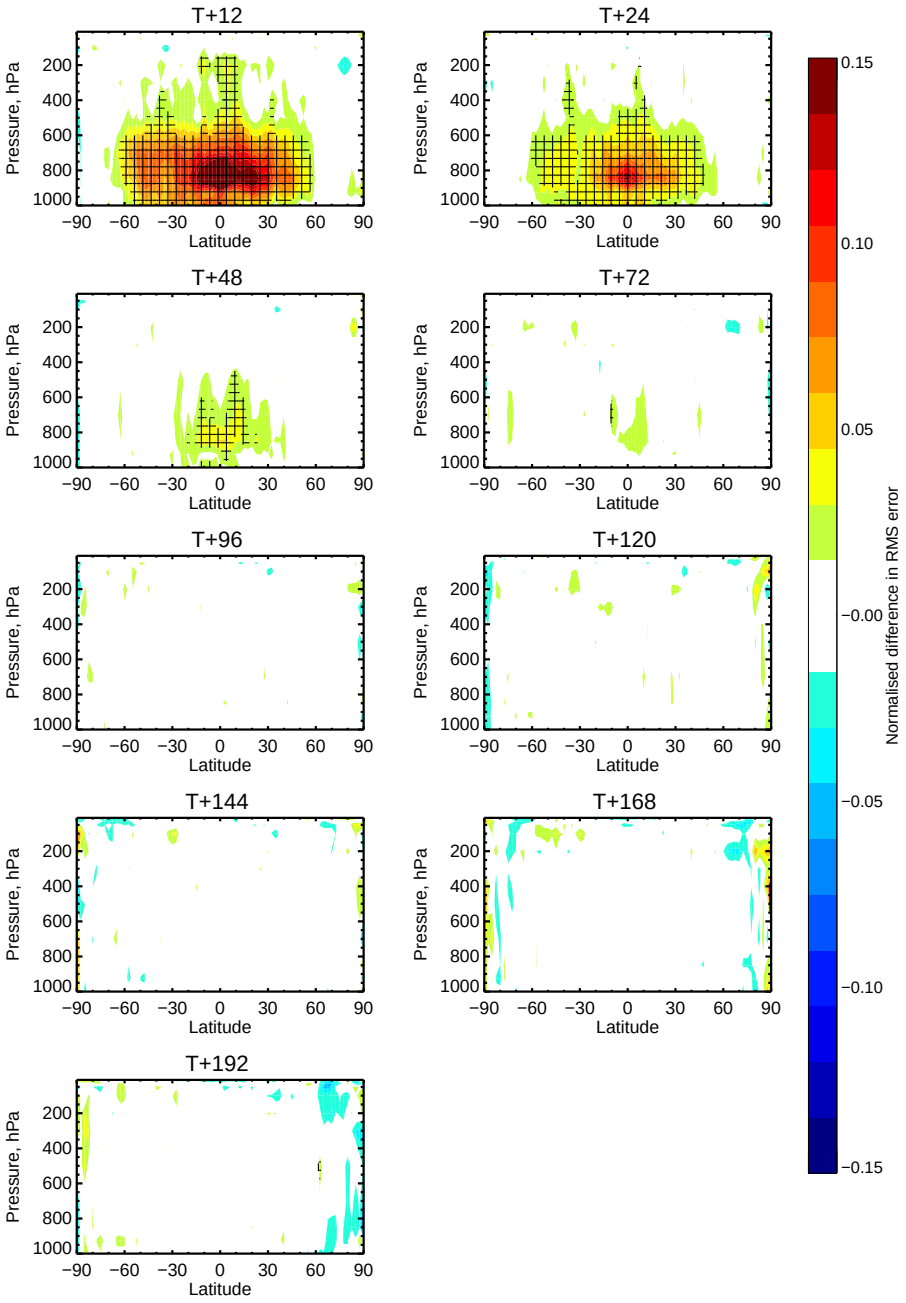

Figure 45: As Figure 44 for relative humidity.

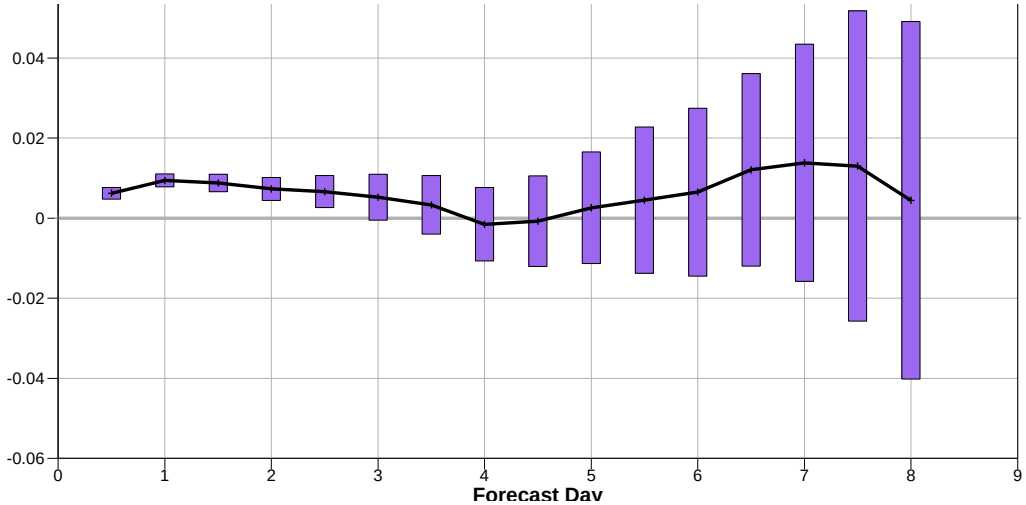

Figure 46: RMS forecast error difference between clear-sky and clear-sky plus overcast infrared radiance assimilation experiments for temperature (in K) at 700 hPa over the Southern hemisphere. Positive values indicate positive impact of the overcast data. Forecast verification is against own analysis, verification period is 20/05/2009-31/12/2009. Vertical bars represent 95% significance levels.

5.2.3 Advanced diagnostics

Analysis and forecast experiments using the ECMWF 4D-Var system have been performed for June 2009 to assess, in particular, the impact of SSM/I and AMSR-E microwave imagers observations that are sensitive to humidity, cloud, precipitation and ocean surface wind speed (Geer at al. 2010). The 24-hour forecast error contribution (FEC) of the all observing system components has been computed and shown in Figure 47. The largest contributions to reducing forecast error (FEC) is provided by AMSU-A (16%), IASI and AIRS (12%) followed by AIREP (aircraft data 10%), TEMP (radiosonde 7%), GPSRO (6%) and SCAT data (5%). All other observations contribute up to 4%. SSM/I decreases the 24-hour forecast error by 4% and AMSR-E by 2%. Therefore SSM/I provides the largest contribution among radiance data sensitive to humidity.

The total observation influence of microwave imager data (or DFS, see Section 6.2) can also be computed by channel and be separated into clear and cloud/precipitation affected areas. Figures 48a-b show the DFS (a) and FEC (b) for the five active SSM/I and AMSR-E channels, and for the different data classes. The classes are assigned during the assimilation process according to the presence or absence of clouds in the model first guess (12-hour forecast) and the observations. 'Cloudy' and 'Clear' denote those data samples where both model and observations have cloud and clear-sky conditions while 'OBS-Clear' and 'OBS-Cloudy' denote the samples where the model and observations disagree.

For the SSM/I, the largest observational information contribution in the analysis is provided in clear skies between 18% by channel 1 and 5% by channel 6. The other samples have fairly similar DFS that are below 5%. The first two SSM/I channels have strong sensitivity to surface wind while channels 3 and 6 are dominated by water vapour. The 'Clear' sample also represents the largest mean OIA per single observation. On the contrary, the 'Cloud' sample has the smallest OIA per single observation so that the DFS is increased due to the large number of data in this sample and not the largest mean observation influence. For the AMSR-E, the per-channel-impact distribution is different, partly because the instrument also has a horizontally polarized 24 GHz channel with strong sensitivity to water vapour. This channel enhances the contribution of both channels 7 and 8.

With respect to FEC (Figure 48c-d), class 'Cloudy' produces by far the largest values in SSM/I channels 1-3 while the FEC is more similar across all samples for channels 4 and 6. Channels 1-3 are mostly sensitive to precipitation and water vapour in that class and there will also be some impact through surface wind. Again, the distribution is slightly different for AMSR-E where both 24 GHz channels receive the highest FEC in clouds.

In general, the assimilation of humidity sensitive radiances from microwave instrument shows the largest analysis influence when observations, together with the model first-guess, indicate that the scene is clear sky while the largest contribution to the 24-hour forecast error reduction comes instead from observations taken in cloudy areas. This can be due to various reasons: Cloudy areas are believed to be the regions where the forecast error is propagating faster, the forecast error therefore depends more strongly on the initial conditions and, consequently, the assimilated observations contribute stronger to reduce forecast error than in other regions where the forecast error is much smaller. Moreover, both OIA and FEC depend on the transpose Kalman gain matrix, $\mathbf{K}^T$, and FEC also depends on the accuracy of the forecast error calculation. In particular FEC is modulated by the percentage of the forecast error that projects onto $\mathbf{K}^T$. Therefore, errors in the forecast error and errors in both model and observation operator can lead to inaccurate estimates of FEC. However, the above results show quite substantial differences between OIA and FEC and, most likely, these are due to the above mentioned effect of data being most effective in areas with large dynamic activity and where forecast errors are large.

Observation influence and forecast impact with respect to a particular data type can also be geographically mapped. Figure 49a shows the average OIA for all SSM/I radiances. The largest contribution in the analysis is found at tropical and sub-tropical latitudes and follows the distribution of water vapour and precipitation. When separated into clear and cloudy data samples no significant difference in the geographical distribution was found, i.e. also the sensitivity of the observation to water vapour is dominant in clear skies.

The distribution of FEC is illustrated in Figure 49b where negative (blue shading) and positive (red shading) values relate to a decrease and increase of forecast error, respectively. A quite consistent decrease of the 24-hour forecast error is observed almost everywhere. The degradation (positive values) patterns are difficult to associate with meteorological features and do not show strong systematic geographical patterns. Areas of improvement are near regions of dynamic activity even though they do not exactly correspond with the areas of highest OIA in convection. Among the different data classes the 'Cloudy' sample matches best the distribution shown in Figure 49b.

Two areas of forecast impact have been analyzed in detail: the central eastern equatorial Pacific where the ITCZ is located, and the Arabian sea where the Monsoon season is active at this time of the year. Figure 49b showed that SSM/I largely contributes to a decrease of forecast error along the mean position of ITCZ. The impact of the SSM/I on the mean analysis state has been investigated by performing another experiment in which SSM/I data have been withdrawn. Figure 50 shows a zonal cross section between 150 and 110 degrees West (150-110W) of the mean analysis differences for June 2009 for relative humidity (Fig. 50a) and vertical velocity (Fig. 50b). Figure 50a shows that the amount of humidity in the upper boundary layer is decreased by a maximum of 4% whilst near the surface relative humidity is increased on average by 2% between 0 and 20N.

The indirect impact on the circulation can be seen in Figure 50b where the vertical velocity cross section differences indicate an intensification of the Hadley circulation. In particular, the main location of the Hadley cell's upward motion near 8N depicts an increased vertical velocity of 0.04 Pa that results in the intensification of the lower level convergence. SSM/I data therefore tends to enhance the Hadley circulation in this case. Note that this circulation tends to be too weak in the ECMWF model on a general principle.

In the Arabian sea the month of June is dominated by the initiation of the Monsoon circulation. In Figure 49b, a general decrease of the 24-hour forecast error has been found in this area with a larger impact close to the Arabian peninsula and the Indian continent. The mean relative humidity analysis difference between the two experiments indicates a mean moisture reduction by the SSM/I data by up to 6% in the lower troposphere and along the meridional direction (Figure 51a). Here, the indirect effect on the wind field can be summarized from Figure 51b. The zonal cross section between 50 and 71E indicates an overall reduction of the zonal wind component in the boundary layer by up to 0.4 m/s, again counteracting a model tendency to overestimate the northward circulation in the northern part of the Arabian sea and the equatorial region.

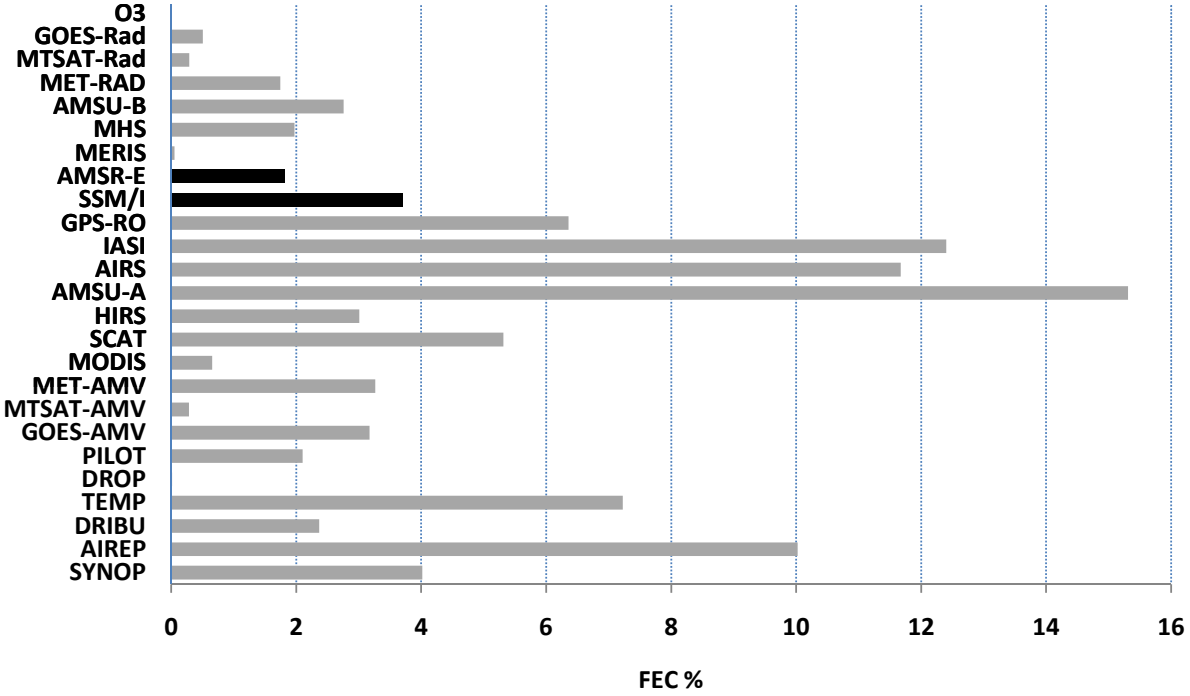

Figure 47: 24-hour relative forecast error contribution (FEC) in % for June 2009 and all assimilated observation types.

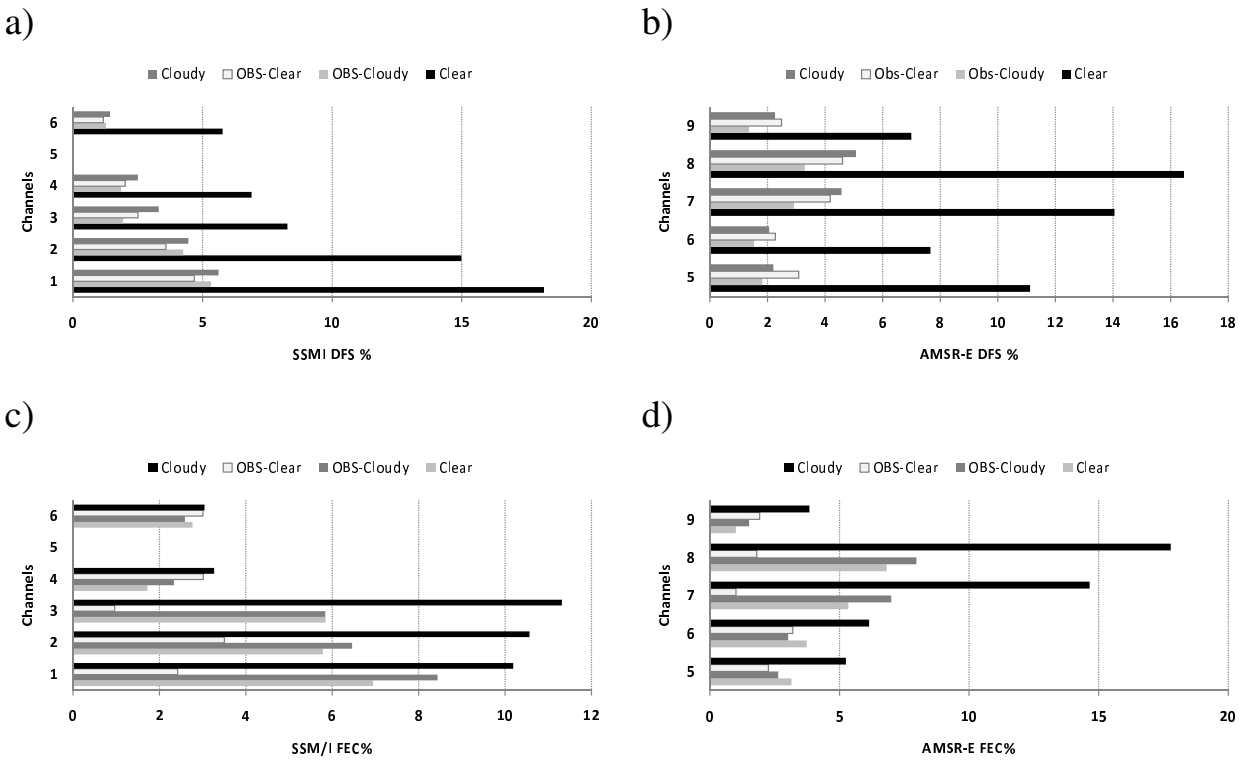

Figure 48: DFS (a, b) (i.e. sum of OIA) and FEC (c, d) in % per assimilated SSM/I (a, c) and AMSR-E channel and per clear/cloud data set.

a)

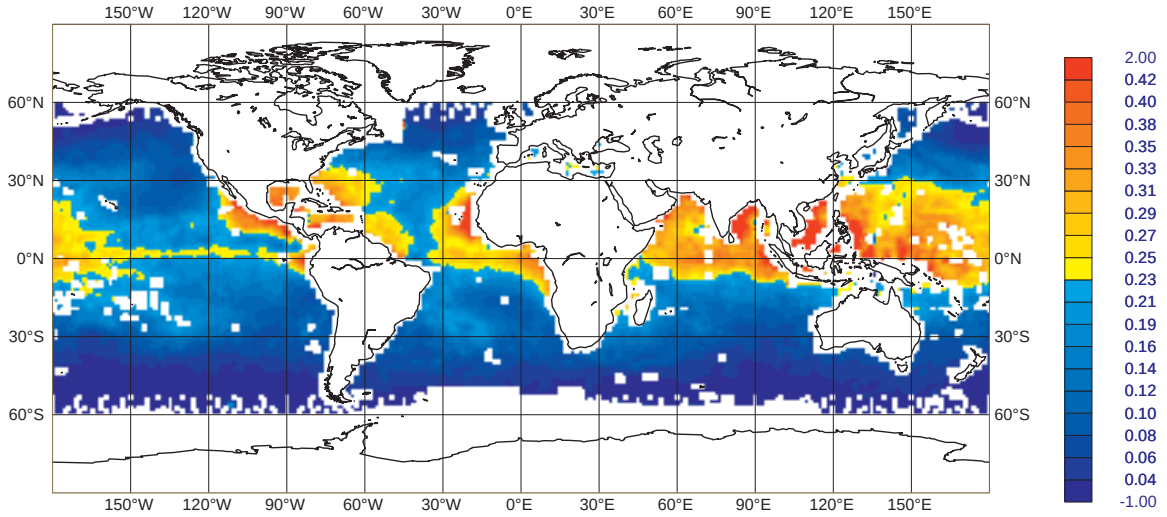

b)

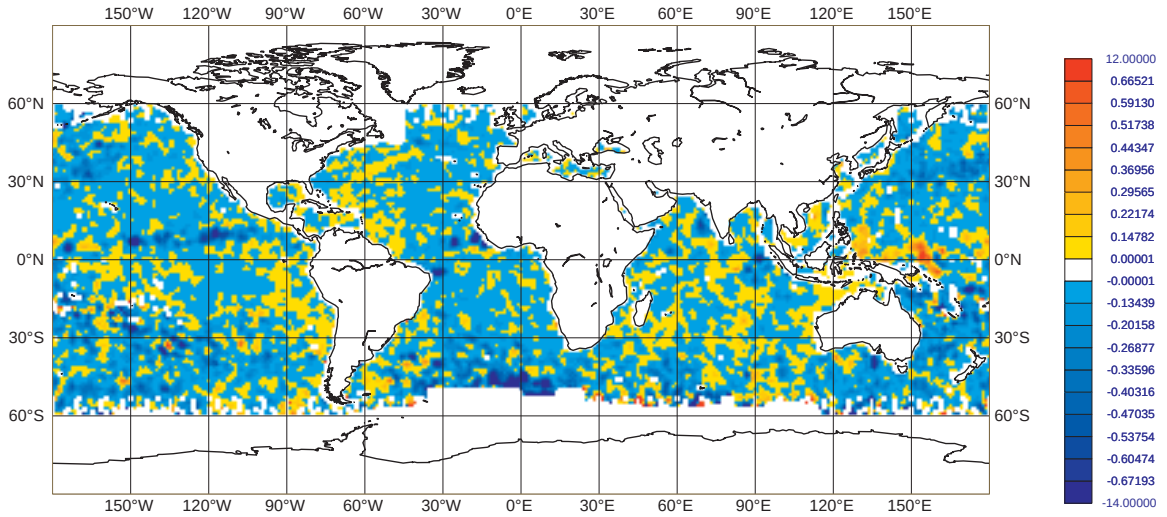

Figure 49: Geographical distribution of SSM/I radiance OIA (a) and FEC (b; in Joule) averaged over June 2009.

a)

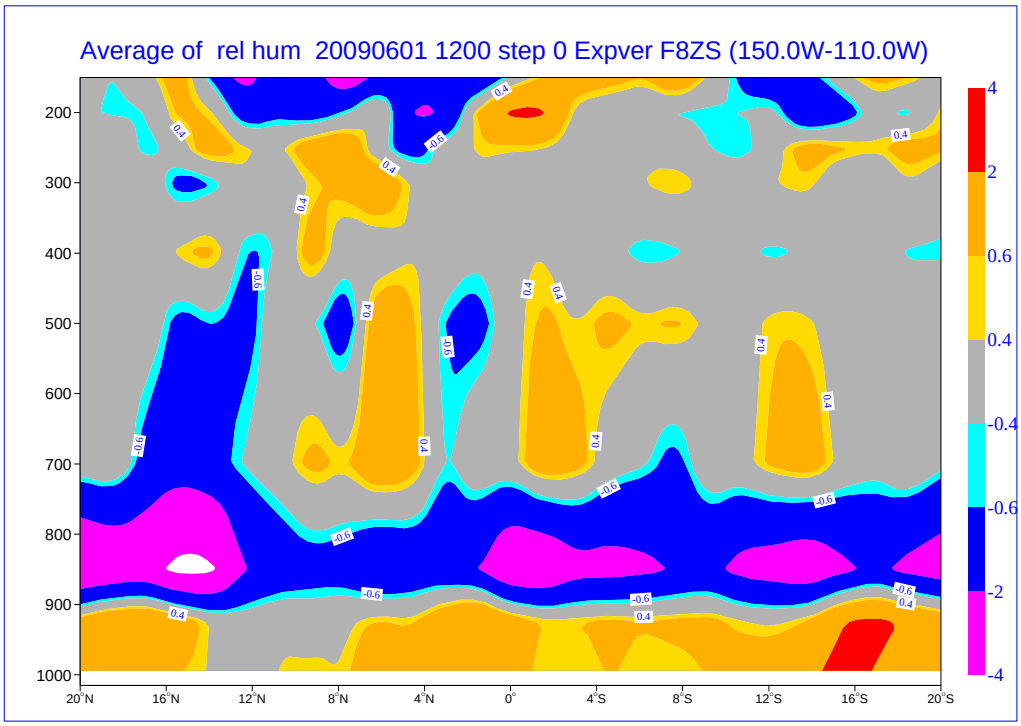

b)

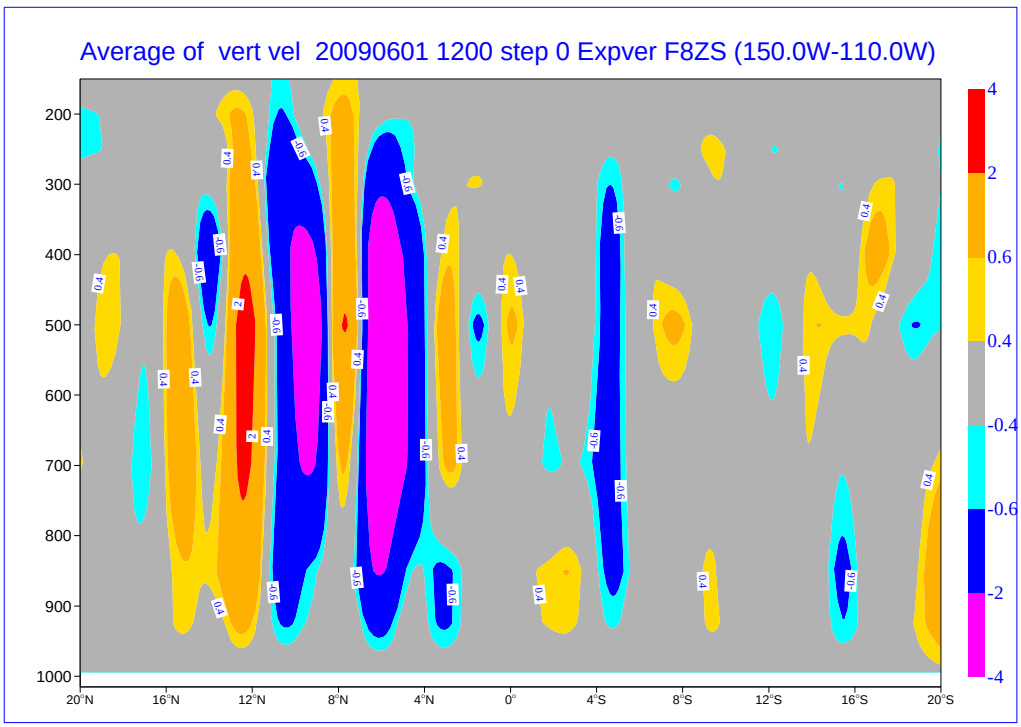

Figure 50: Zonal cross section (150-110W) of the mean analysis difference between experiments with and without SSM/I data for June 2009 for relative humidity (a; in %) and vertical velocity (b; in $10^{-2}Pa/s$).

a)

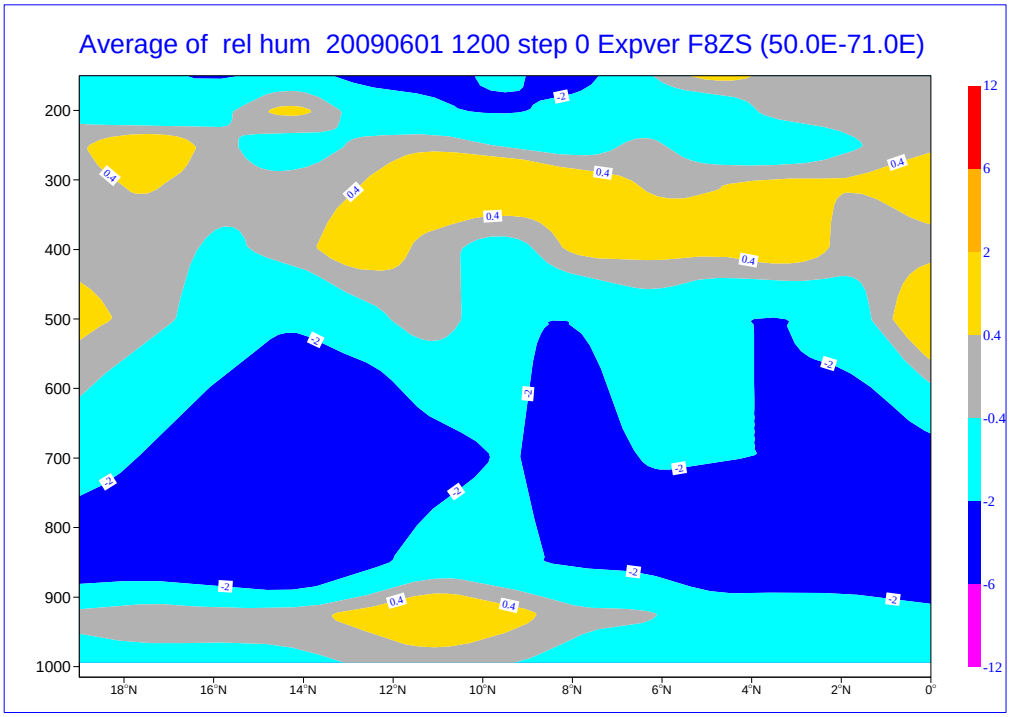

b)

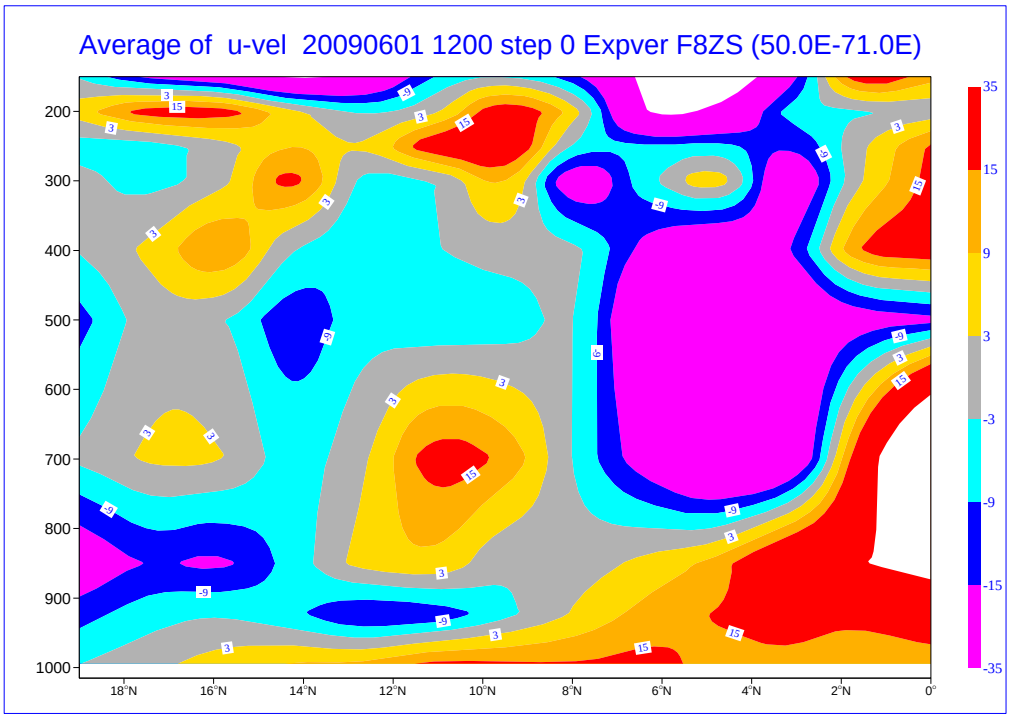

Figure 51: Zonal cross section (50-71E) of the mean analysis difference between experiments with and without SSM/I data for June 2009 for relative humidity (a; in %) and zonal wind speed (b; in m/s).

Summary

The assimilation of all-sky radiances from microwave imagers over oceans is found to systematically change the mean state of moisture over oceans. This change produces a better fit of analyses and short-range forecasts with other moisture sensitive radiances over oceans and also causes less general radiance data rejection. The impact of SSM/I data on boundary layer temperature and humidity is stronger than that of AMSU-A/MHS or HIRS, especially over the Tropics. Forecast verification of moisture instrument impacts strongly depends on the verifying analysis. In this case, the operational analysis that is used as a reference also contains all-sky microwave imager data and may thus produce favourable results. However, a positive impact was found for temperature, moisture and wind that lasts for a few days but dissipates faster than the forecast impact obtained from temperature sensitive data that affect larger scale structures. The assimilation of cloud-affected infrared radiances was shown to systematically affect temperatures in areas of overcast cloud regimes. While the impact of this on forecasts is small, the regional temperature analysis has been improved. This result is quite significant since, generally, much less radiance data is used in the presence of clouds.

The analysis and forecast impact of microwave all-sky radiances is strong as indicated by the adjoint measures. Interestingly, the impact on the analysis is mostly driven by clear-sky observations while the forecast impact is dominated by cloud-affected observations. This demonstrates the combined impact of the model and data assimilation and their sensitivity to information in areas where background errors are large and the model is rather sensitive to temperature and moisture information. Case studies also demonstrate the link between the observations' primary sensitivity to moisture/temperature and dynamics. Cases obtained over the ITCZ and the Indian Ocean monsoon show wind increments that are consistent with the moisture information provided by the observations and that counteract known model deficiencies in these areas.

5.3 Atmospheric Motion Vectors

The initial work plan included impact experiments based on AMVs derived from METOP AVHRR and a version of the same product that employs an improved height-assignment based on IASI cloud top retrievals. One month worth of data has been provided and the results from the evaluation performed in the ECMWF system has been reported elsewhere so that they will not be reproduced here. This section will thus focus on the comparative impact of AMVs derived from MODIS imager and HIRS infrared sounder data on wind analysis.

Peubey and McNally (2009) (hereafter PM09) compared the wind analysis impact of geostationary clear-sky radiances (CSRs) and atmospheric motion vectors (AMVs) derived from geostationary satellites. They isolated the different mechanisms through which the assimilation of CSRs constrains the analysis and they found that the most important mechanism in this respect is the humidity tracer advection. This means that 4D-Var is trying to adjust wind such that moisture fields can be redistributed to minimize differences between observed and modelled moisture sensitive radiances. In this work package a similar comparison has been performed for polar-orbiting satellite data to understand in how far the PM09 results can be transferred to high latitudes.

An investigation of the details of CSR impact as in PM90 has not been repeated in this study because it is reasonable to assume that the gross findings of PM09 from geostationary observations are also valid for polar orbiting satellites. The experimentation period covered 01/07-30/09/2009. Similarly to the sounder experiments a T511 model resolution has been used and the experiments are based on model version CY36R1. As in PM09, a baseline (hereafter 'Baseline') observing system has been defined that

only contained NOAA-18 AMSU-A radiances in addition to conventional observations to constrain the main large-scale atmospheric structures. The exclusion of most satellite data allows the amplification of the impact of wind observations for general study purposes.

In total, the following experiments have been performed:

- A: Baseline with conventional observations plus NOAA-18 AMSU-A radiances;
- B: Baseline plus MODIS polar AMV winds derived from TERRA and AQUA MODIS imagery;
- C: Baseline plus all HIRS radiances from both NOAA-19 and METOP (i.e. channels 11, 12);
- D: Baseline plus only water vapour HIRS channel radiances from both NOAA-19 and METOP;
- E: like C, but HIRS usage restricted to polar areas;
- F: like D, but HIRS water vapour channel usage restricted to polar areas;
- G: B+E, i.e. MODIS winds plus HIRS radiances over polar areas;
- H: B+F, i.e. MODIS winds plus HIRS water vapour channel radiances over polar areas.

Figure 52 shows the horizontal distribution of all assimilated HIRS water vapour channel 12 and MODIS polar AMV data in a given 12-hour 4D-Var assimilation window. This represents the data usage in experiments D and B, respectively, in addition to the Baseline observing system. It can be seen that the HIRS data usage covers the entire globe with an orographic restriction (i.e. land points with more than 1500 m elevation are excluded due to excessive surface emission contributions) while AMV data usage is, by definition, limited to the polar areas. This makes the comparison of experiments B and C-D difficult due to the potential impact of non-polar data on polar winds. Therefore experiments E-H have been added. Due to the orographic restriction of HIRS radiance data usage over large areas near the South Pole data counts can also be in favour of AMVs. For reasons of different data selection, the following impact analysis has to be interpreted with care.

The following assessment is performed in terms of analysis error that is quantified as the RMS difference between analyses of the respective experiments and a reference analysis, i.e. operations. The latter is based on the high-resolution model and the entire observing system. When data is added to the baseline the resulting analysis is always expected to perform better when compared to Baseline.

Figure 53 shows the normalized RMS analysis error reduction of 700 hPa vector winds from adding AMVs (left, experiment B), all HIRS radiances (middle, experiment C) and HIRS water vapour channel radiances (right, experiment D). The results for the North (South) Pole are shown in the top (bottom) panel. Figure 54 shows the same picture for 300 hPa. Both figures suggest that both AMV and CSR data improve the wind analysis. Not surprisingly, the impact of AMVs is restricted to the Poles and is somewhat smaller than that of CSRs. Exceptions are the 700 hPa level over the North Pole where the positive impact of AMVs is slightly stronger and at 300 hPa in the central part of the Antarctic continent where HIRS data are practically not used but AMVs are proven to give an important contribution to the wind analysis. It can also be seen that, in general, assimilating only water vapour channel HIRS data results in significantly worse wind analyses than when all HIRS channels are used. This suggests, that in the case of the assimilation of CSRs from polar orbiting satellites the humidity tracer advection effect is not the only mechanism that provides a contribution to the wind analysis improvement. Obviously, the temperature sensitive channels are crucial for improving the analysis in general and the wind analysis in particular just like at lower latitudes.

Table 3 summarizes the overall mean values of the normalized RMS analysis error reductions seen in the above figures for all experiments (B-H) compared to the Baseline. From the table it is derived that the impact of the added data is - as expected - always positive, even though it is close to neutral at 200 hPa where the smallest data numbers are found. Using only HIRS water vapour channels basically halves the impact of all channels on analysis quality. In this case, radiance and AMV assimilation impact is fairly similar, a results that was also obtained at lower latitudes by PM09. Restricting the radiance data usage to polar areas has a weaker effect in the North than South. In the North, the impact of data assimilated at lower latitudes affects polar winds very little while in the South a 20% increase of analysis error is noted when data is only used over polar areas. In fact, the Southern hemispheric winter troposphere exhibits rather wide areas of atmospheric instability that will increase the sensitivity of the polar analysis to non-polar data.

Similar pressure levels are found for which the strongest impact is observed from either AMV or radiance assimilation, which is in contrast to the experience at lower latitudes. For both data, the impact at 300-700 hPa is most pronounced while at lower latitudes AMVs showed a particularly strong impact for low-level winds in subtropical subsidence zones. While large parts of the northern polar areas are dominated by Arctic stratus in the summer season, the derived AMVs do not seem to produce large data samples at very low altitudes, partly due to problems of low-level cloud detection.

When AMVs and CSRs are assimilated together the analysis accuracy is improved over the accuracy obtained from assimilating either one alone. This, however, only holds for the Northern polar areas while adding AMVs to the radiance assimilation over the South Pole does not produce an improvement over the radiance assimilation.

Figure 55 shows the normalized RMS analysis error reduction of 500 hPa vector winds over the South Pole area for experiments B-H as compared to the Baseline. It is seen that only AMVs are improving the wind analysis over most of the Antarctic continent itself (i.e. experiments B,G and H) due to the limited radiance data usage over the Antarctic plateau. The radiance data impact that is represented in Table 3 therefore originates from areas away from high surface elevations.

Summary

The impact of AMV observations has been tested in a more fundamental way than that of the other observation types because the main objective has been to evaluate the impact of AMVs on the wind analysis in comparison to that of radiance observations in polar areas. This study complements a previous effort performed for both AMVs and CSRs at mid and lower latitudes derived from geostationary satellites. The experiments demonstrated that AMVs in polar areas produce a similar impact to infrared radiance observations (HRS) if only water vapour channels are used while adding temperature sensitive radiances adds more impact. The experiments showed a significant difference of the results between North and South Poles, mainly caused by the largely different quality control applied to radiance data over the Antarctic continent due to high surface elevations.

In contrast to the experiments with geostationary data the heights of largest impact were quite similar over the Poles while over lower latitudes the radiance impact was strongest at mid-levels and the CSRs acted most strongly at low and high levels at which more data is assimilated. Adding radiance data and AMVs together showed an additional improvement that was more pronounced at Northern high latitudes. It must be kept in mind that both AMVs and HIRS-type radiance data do not represent the strongest information contribution in the analysis so that the above described results may be insignificant if a full background observing system is available.

Table 3: Areal mean reduction of the normalized RMS wind analysis error for the experiments B-H compared to the baseline (A) for different vertical levels and for both poles ('all' refers to AMVs obtained from both infrared and water vapour channels or all actively assimilated HIRS channels, 'water vapour' refers to HIRS channels 11 and 12).

Experiment Data type Channels Coverage	B AMV polar	C CSR all global	D CSR water-vapour global	E CSR all polar	F CSR water vapour polar	G CSR+AMV all polar	H CSR+AMV water vapour polar
North Pole:							
850 hPa	2	3	1	3	1	5	3
700 hPa	5	4	2	4	2	7	5
500 hPa	5	8	6	7	6	9	7
300 hPa	5	8	6	7	6	8	8
200 hPa	1	1	1	1	0	2	1
South Pole:							
850 hPa	1	9	4	7	3	7	3
700 hPa	2	9	4	7	3	7	4
500 hPa	6	11	6	7	4	10	8
300 hPa	6	8	5	5	3	9	8
200 hPa	1	3	1	1	1	2	1

a)

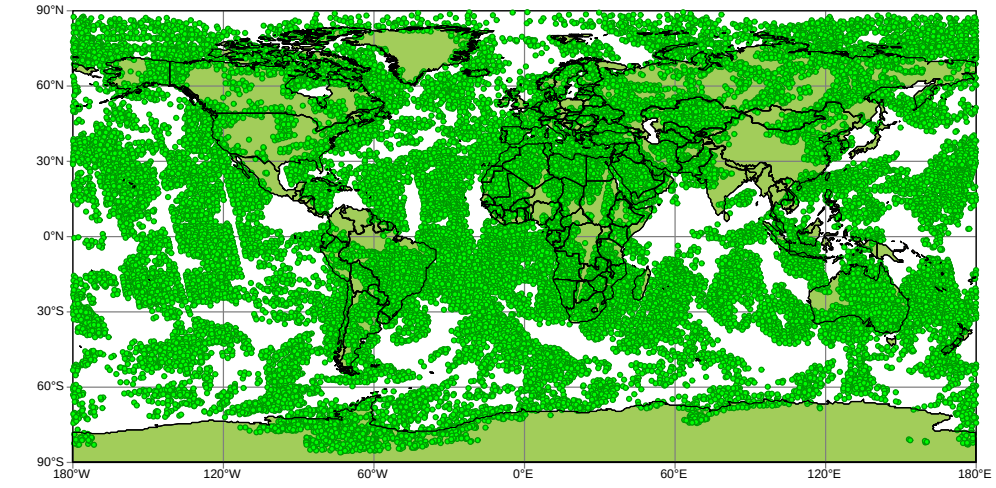

b)

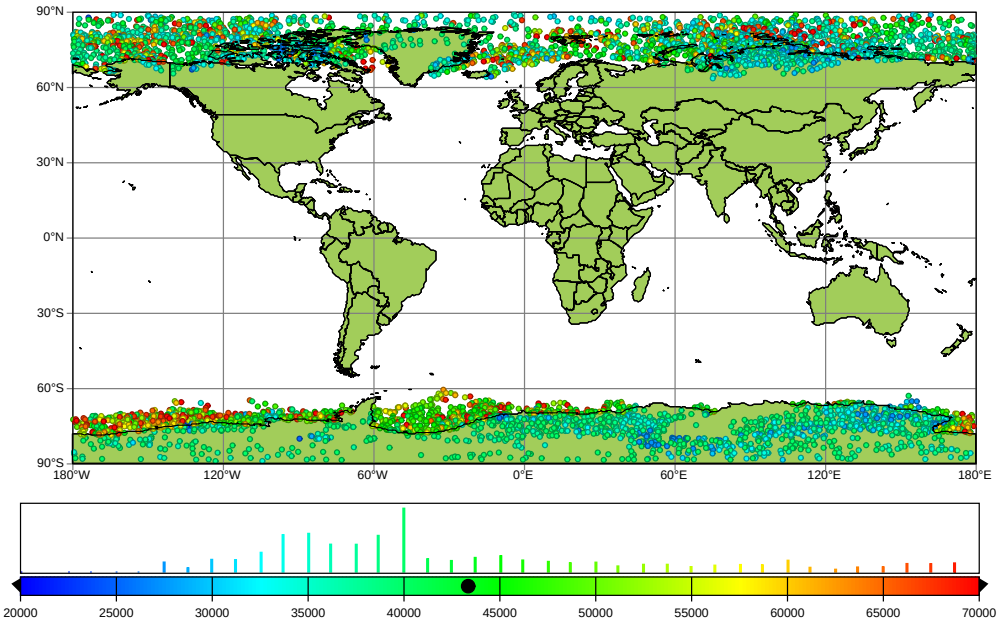

Figure 52: Horizontal distribution of all assimilated HIRS water vapour channel 12 data (a) and MODIS AMV data (b) for a given 12 hour 4D-Var assimilation window. Colours of dots represent pressure levels of polar AMVs.

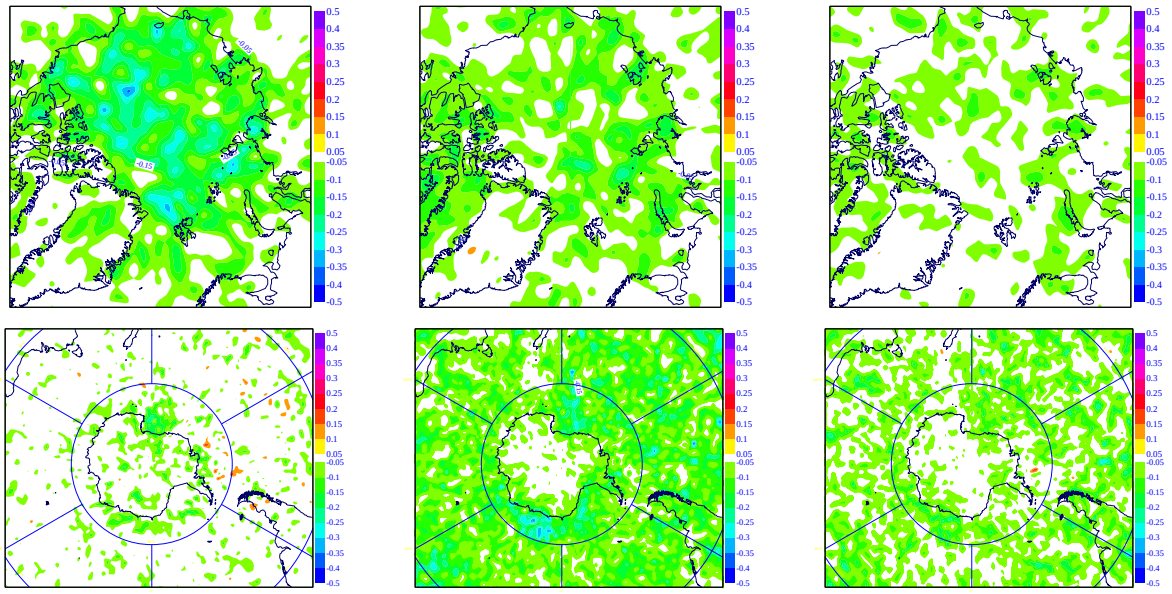

Figure 53: Normalized RMS analysis error reduction of 700 hPa vector wind due to adding AMV (left) HIRS (middle) and water vapour channel HIRS (right) data. Top figures are for North Pole and bottom figures for South Pole. Analysis verification is against the operational analysis and verification period is 07/07/2009-30/09/2009. Negative values (green, blue colours) indicate positive a impact of the additionally assimilated data.

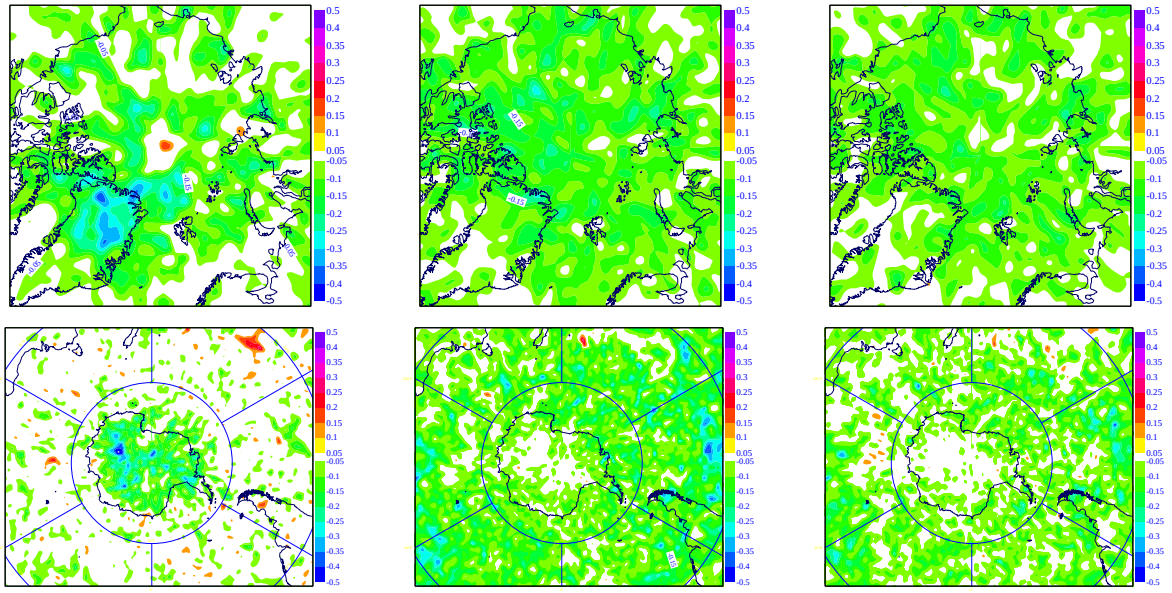

Figure 54: As Figure 53 for 300 hPa.

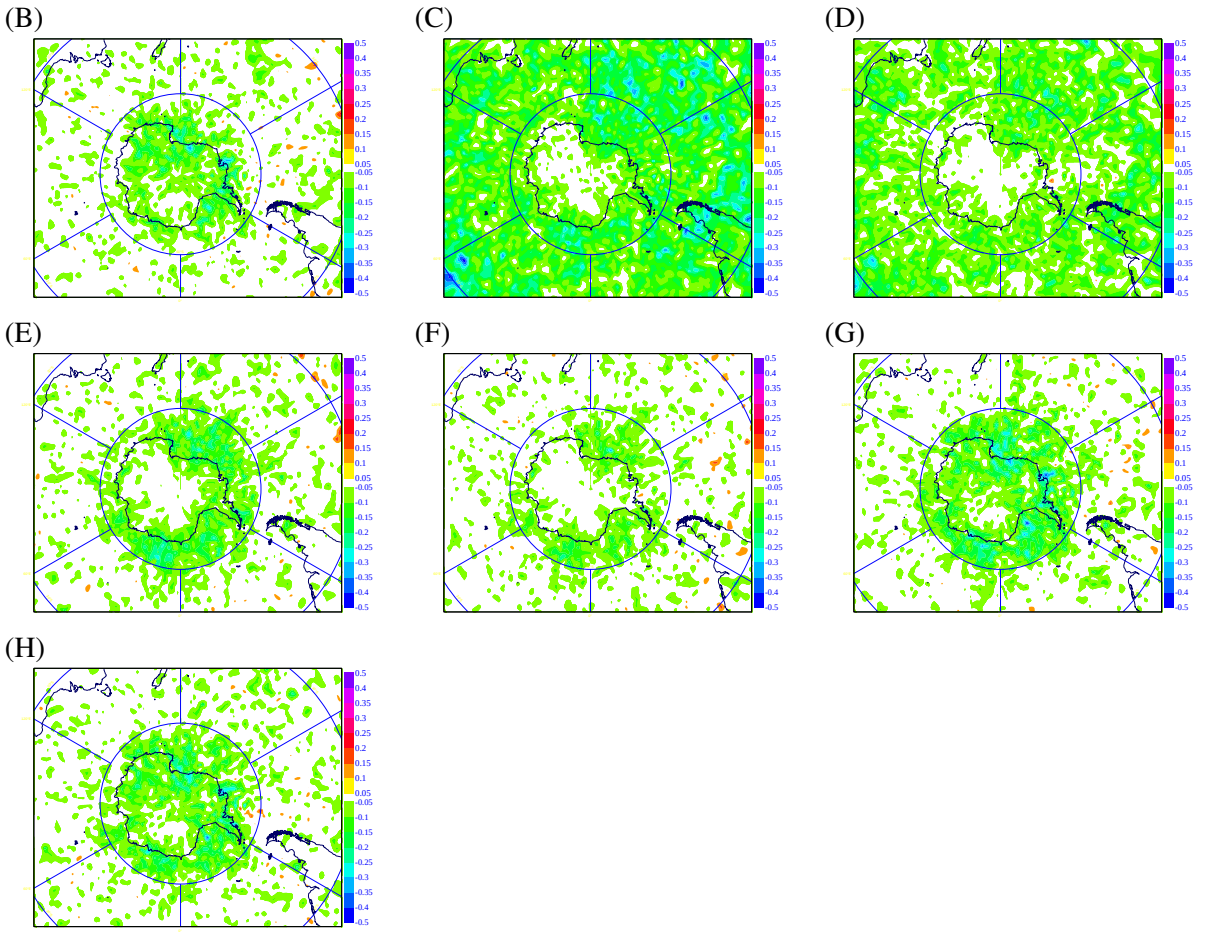

Figure 55: Normalized RMS analysis error reduction of 500 hPa vector wind over the South Pole due to adding AMV and HIRS observations from experiments B-H (see labels near panels). Analysis verification is against operational analysis, verification period is 07/07/2009-30/09/2009. Negative values (green, blue colours) indicate positive impact of the additionally assimilated data.

Table 4: Total number of GPSRO bending angle observations from different sources for a given 12-hour 4D-Var assimilation window 4D-Var.

Type	Number	Type	Number
GRAS	50,087	CHAMP	13,888
Terrasar-X	22,154	GRACE-A	11,059
SAC-C	16,714		
COSMIC-1	48,804	COSMIC-2	58,064
COSMIC-3	44,606	COSMIC-4	59,295
COSMIC-5	40,596	COSMIC-6	53,075

5.4 GNSS Radio occultation OSEs

The experiments with GPS radio occultation data have been performed for 3 months, namely July-September 2008, a period for which experimental GPSRO data from CHAMP, GRACE-A, Terrasar-X and SAC-C have been acquired in addition to the COSMIC and GRAS data that are operationally used at ECMWF. The COSMIC data used in this study was a reprocessed dataset, using the latest operational processing code employed at the University Corporation for Atmospheric Research (UCAR). The reprocessed COSMIC data is much more consistent with GRAS data, in terms of bias characteristics of the bending angles in the lower/mid stratosphere, although the biases with respect to ECMWF short-range forecasts have increased. The SAC-C and Terrasar-X datasets were also processed at UCAR using the latest operational code, specifically for this study. These OSE's are the first assimilation experiments with SAC-C and Terrasar-X datasets. The combined number of bending angle profiles available per day, averaged over the 3 month period, is 2940 which is about 20% more data than used in the operational system.

The background observing system applied in these experiments is analogous to that of the sounder experiments (i.e. Reference), except for the GPSRO usage. In the control experiment all available GPSRO data have been assimilated and three denial experiments have been run assimilating only 5, 33 and 67% of the GPSRO data, respectively. The 5% experiment (i.e. about 150 profiles) is representative of the data numbers from a single instrument, mission of opportunity (e.g. CHAMP), and the 33% and 67% experiments roughly represent a half and full COSMIC constellation, respectively. The total number of different assimilated GPSRO bending angles in a randomly chosen 4D-Var cycle can be seen in Table 4 and the horizontal distribution of all the assimilated GPSRO data in the same cycle is shown in Figure 56.

5.4.1 Analysis

Figure 57 shows the first-guess and analysis fit of the 5% of GPSRO data experiment compared to control in terms of radiosonde temperatures (Fig. 57a) and aircraft temperatures (Fig. 57b). When more GPSRO data are used, the analysis and first-guess are significantly less biased with respect to radiosonde temperatures. This is true both in the troposphere, where the model is warmer than radiosonde observations, and in the stratosphere where it is colder. The only exception is the lower boundary layer, where the model is slightly colder again and the GPSRO data seem to increase the bias. This bias does not appear to be caused by tropospheric bending angles, because it remains when they are blacklisted (not shown). The bias with respect to aircraft temperatures grows with the use of more GPSRO data, but it is mostly due to the aircraft temperature biases, which are at present not accounted for in the ECMWF data assimilation

system.

Figure 58 shows the same statistics, but in this case for the 67% experiment. What has been described for the 5% experiment still holds, but the differences compared to the control experiment are much smaller now.

In Figure 59 the first-guess and analysis fits to GPSRO data itself are shown (5% GPSRO usage vs control on the left and 67% vs control on the right). Having 5% of GPSRO data is clearly insufficient to remove the bias between the model and GPSRO data, which means that a single receiver despite global coverage does not provide enough data. This is particularly true between 12 and 30 km height. The bias difference between the 67% and the control experiments is again smaller, but it is still clearly present and it has its peaks at the same heights as the 5% experiment.

All these results indicate that the assimilation of GPSRO data has a systematic effect on temperature analyses and that there is significant vertical variability due to the general structures of model temperature bias. For further analysis, Figure 60 shows the mean temperature analysis difference fields at 3 different vertical levels between the experiment fully denying GPSRO data and the control (positive values mean that the denial experiment is warmer). From the figure the systematic differences can be well identified and they reach up to 1 K. The figure clearly confirms what has been seen from the radiosonde fits, i.e. that GPSRO data warm the analysis in the stratosphere and cool it in the troposphere. It is also seen, that these differences are much smaller in the data-rich continental areas of the Northern hemisphere. This is likely to be because radiosondes strongly constrain the analysis reducing the draw towards GPSRO data and because radiosonde temperatures and GPSRO data are in good agreement.

Due to the hydrostatic relationship GPSRO data do not only constrain the temperature profile of the analysis, but simultaneously the surface pressure as well. Therefore it can be expected that the assimilation of GPSRO data has an impact on surface pressure analysis. This effect is, however, not easy to see in standard experimentation first-guess and analysis departure statistics since the land and buoy surface pressure observations are actively assimilated.

Another set of experiments has been performed where conventional surface pressure observations have been removed and the impact of GPSRO has been examined in the same framework as for the other experiments. In these experiments the passive conventional surface observations can be used as an independent, unbiased representation of the truth. Figure 61 shows the first-guess and analysis departure histograms for SYNOP and buoy surface pressure observations over the Southern hemisphere and North Atlantic region, respectively, for the experiments with (red) and without (black) GPSRO data. If no surface pressure related data are assimilated biases are large and amount to 1-2.5 hPa. However, the presence of GPSRO data removes half of this bias compared to both against buoy and SYNOP surface pressure observations. The error standard deviations are also 2-10% smaller when GPSRO data are present both in the first-guess and in the analysis. It has to be mentioned that the statistics shown in Figure 61 have been generated after a two-months spin up period of the experiments, which seems to be required for the surface pressure bias to stabilize when this experiment is initialized with the operational analysis at the beginning of the period. This two months drift has can be seen in Figure 62 for the experiment without GPSRO data.

5.4.2 Forecast

Figure 63 shows zonal cross-sections of normalized RMS temperature forecast error differences (left) and geopotential height anomaly correlation differences (right) that are derived from the GPSRO full denial experiment against the control. Both indicate a strong positive impact of GPSRO data, especially

in the upper atmosphere. Above 200 hPa the impact remains visible even for 7 days. It has to be noted that for geopotential height RMS errors do not clearly indicate the positive effect which is due to the change in biases shown in Figure 64 for 100 hPa geopotential. It can be seen that GPSRO assimilation systematically reduces the 100 hPa geopotential as an integral of the tropospheric cooling and stratospheric warming effect discussed before. It is also worth noting that the reprocessed COSMIC bending angle bias characteristics differ from those used operationally during this period and this will have an impact on the 100 hPa height biases because the GPSRO measurements receive a lot of weight in this region due to the definition of observation errors.

Figure 65 shows the same geopotential height anomaly correlation difference as the right picture of Figure 63 but now for the experiments where 33 (left) and 67% (right) of the GPSRO data are assimilated. The forecast score differences become smaller and smaller as more and more GPSRO data are assimilated and with using two thirds of the data the differences vanish, except for the first 24 hours above 200hPa.

Figure 66 shows the normalized RMS forecast error difference between the different GPSRO denial experiments (numbers denote the percentage level of denial) and the control for temperature. Down to 500 hPa the more GPSRO data is used the better the scores become. A surprising negative effect can be observed, however, at 1000 hPa, especially over the Tropics. This degradation is again very likely a model bias issue and it is in agreement with what has been seen in Figure 57 from the boundary layer statistics, where the detrimental impact of GPSRO data on the biases against radiosonde temperatures was noted. At 200 hPa in the Southern hemisphere and 500 hPa in the Tropics GPSRO data tends to have a negative impact between days 2 and 4 and the degree of degradation increases with GPSRO data volume. This degradation is most likely an artefact from the differences in data pre-processing between the experiments and the operational system, the latter being used for verification in this figure. The UCAR processing translates to a small but noticeable change observation-minus-model biases that produce sub-optimal analyses when compared to operations given the impact of these observations on model biases changing sign across the tropopause.

The capability of GPSRO data for constraining temperature analyses in comparison with other satellite data, especially advanced sounders, has been investigated with another set of experiments in a poor baseline context. The Baseline of these experiments contained no radiance data at all (and no aircraft temperature data due to apparent observation biases as mentioned before). Figure 67 (red curves) shows the normalized differences of temperature anomaly correlations between Baseline minus Baseline+GPSRO in red and Baseline+IASI minus Baseline+GPSRO in black. The negative values for the red curves indicates that adding GPSRO data always improves the scores and it is evident that the improvement is the strongest at 200 hPa over the Southern hemisphere. The black curves directly compare the IASI and GPSRO impact show whether IASI (above zero) or GPSRO (below zero) data improve the temperature anomaly correlation scores more efficiently. Up to 500 hPa the IASI impact is clearly stronger while at 200 hPa over the Southern hemisphere they seem to be of equal impact. It is worth noting in this context that typically 3 million IASI radiances are assimilated per 12 hour cycle, compared with around 300,000 bending angle values.

Summary

GPSRO data represent a substantial part of the observing system since they do not require bias correction and produce accurate observations of (mainly) temperature with very good vertical resolution in the upper atmosphere where radiance data is more sparse and NWP model errors are large. For the experiments in this study, data in addition to the currently assimilated receivers onboard METOP GRAS and the Formosat-COSMIC constellation have been acquired to make available as many GPSRO observation as

possible. All data have been assimilated and three denial experiments have been run using only 5, 33 and 67 % of the GPSRO data, respectively. The 5 % experiment (i.e. about 150 profiles) is representative of the data numbers from a single instrument.

The results from the 5 % experiment indicate that the impact on temperature analysis is significant but not yet sufficient to remove the entire upper atmospheric temperature bias. Gradually increasing the number of observations further corrects the problem but the analysis fits to radiosonde observations clearly indicate that more observations could benefit. The radiosonde fits also suggest that the impact has a vertical structure, namely that GPSRO data warm the analysis in the stratosphere and cool it in the troposphere.

Due to the hydrostatic relationship GPSRO data do not only constrain the temperature profile of the analysis, but simultaneously the surface pressure as well. This has been tested by removing conventional surface pressure observations but assimilating GPSRO data. The presence of GPSRO data removes half of the surface pressure bias originating from removing surface pressure observations when verified against both buoy and SYNOP surface pressure observations. The error standard deviations are also 2-10 % smaller when GPSRO data are present both in the first-guess and for the analysis.

RMS temperature forecast errors and geopotential height anomaly correlations are positively affected by GPSRO data, especially in the higher atmosphere. Above 200 hPa the impact remains visible even for 7 days. A surprising negative effect is found, however, at 1000 hPa, especially over the Tropics for temperature. This degradation is very likely a model bias issue and it is in agreement with what has been seen in boundary layer radiosonde statistics.

Finally, experiments have been run to compare the impact of IASI radiance data with that of GPSRO observations. Up to 500 hPa the IASI impact is clearly stronger, At 200 hPa over the Southern hemisphere they seem to be of equal impact. Over the Tropics GPSRO seems to bring slightly more improvement than IASI. Over the Northern hemisphere in the first two days GPSRO data improves the forecast slightly more, but afterwards the IASI impact becomes much stronger. These results have to be viewed keeping in mind that about one order of magnitude more radiances than bending angles are assimilated.

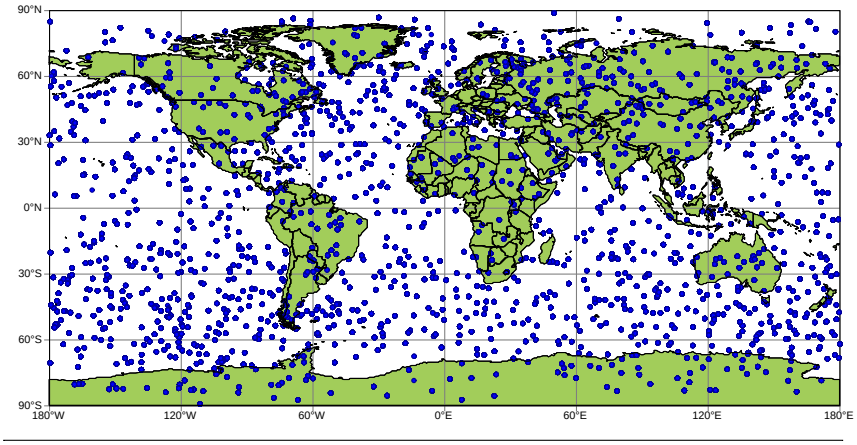

Figure 56: Horizontal distribution of all assimilated GPSRO data for a given 12-hour 4D-Var assimilation window 4D-Var.

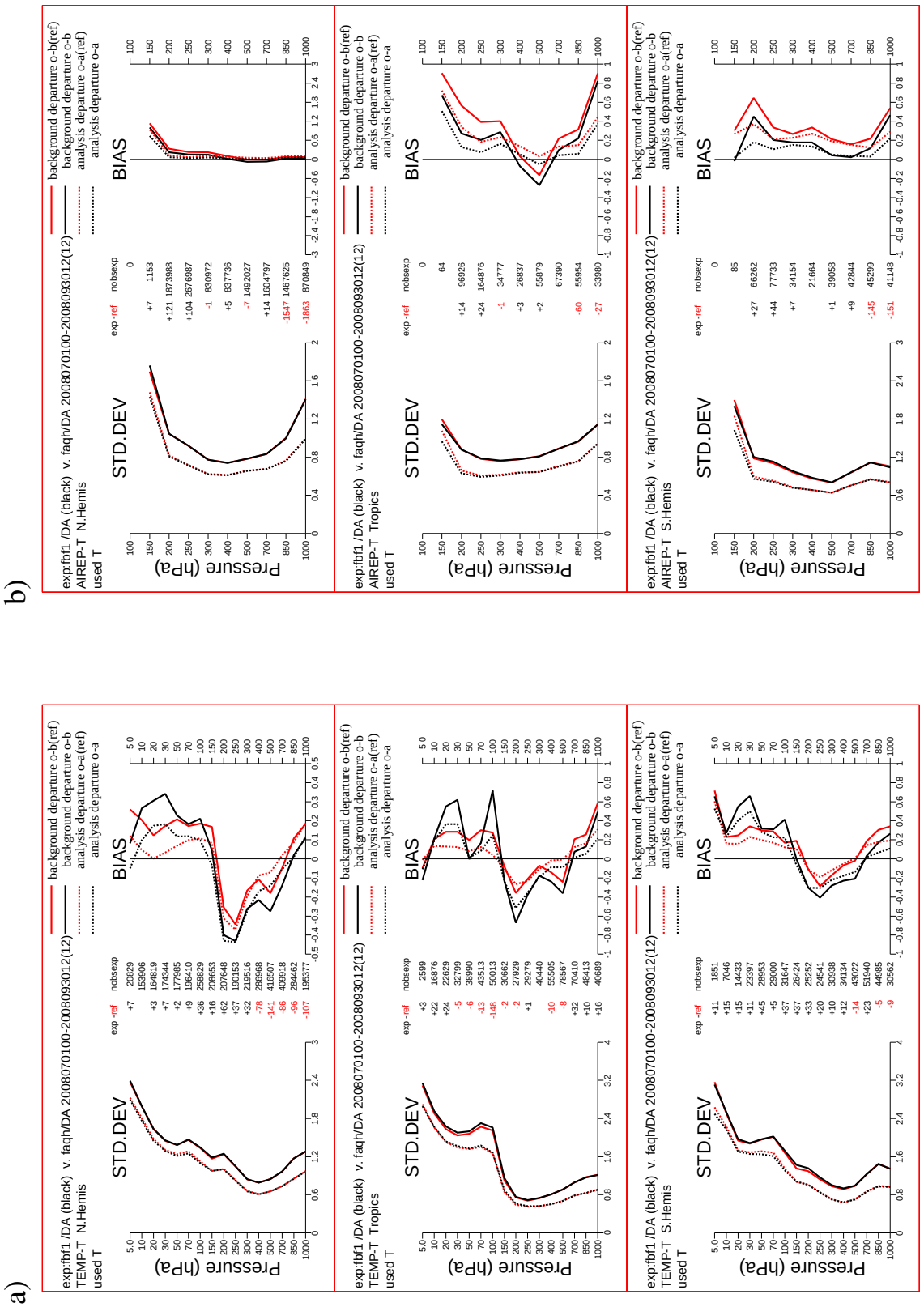

Figure 57: A): Fit between model first-guess (solid) and analysis (dashed) with radiosonde temperatures in the Northern hemisphere (top), Tropics (middle) and Southern hemisphere (bottom) from GPSRO denial (black) keeping only 5% of RO data and control (red) experiments. Left panels show standard deviations, right panels show biases. Numbers in central column denote the data sample from the denial (right, black) experiment and the difference between denial experiment and control (left, black or red). Statistics were generated from period 01/07-30/09/2008. B): Same as A), but statistics for aircraft temperatures

a)

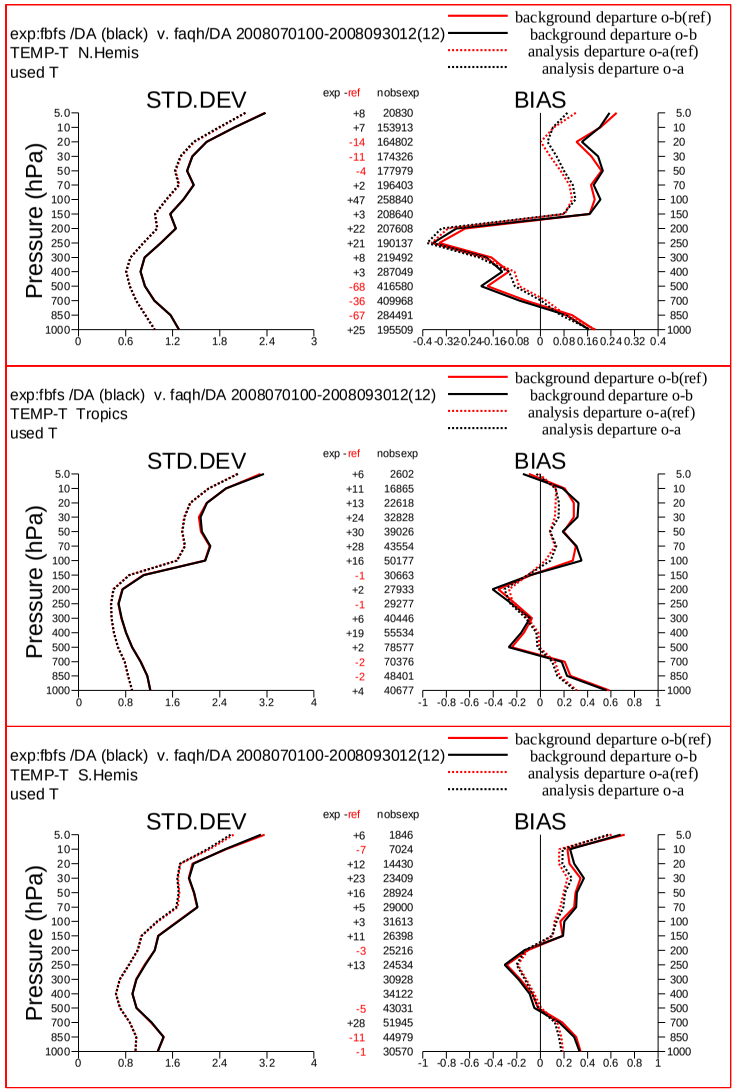

b)

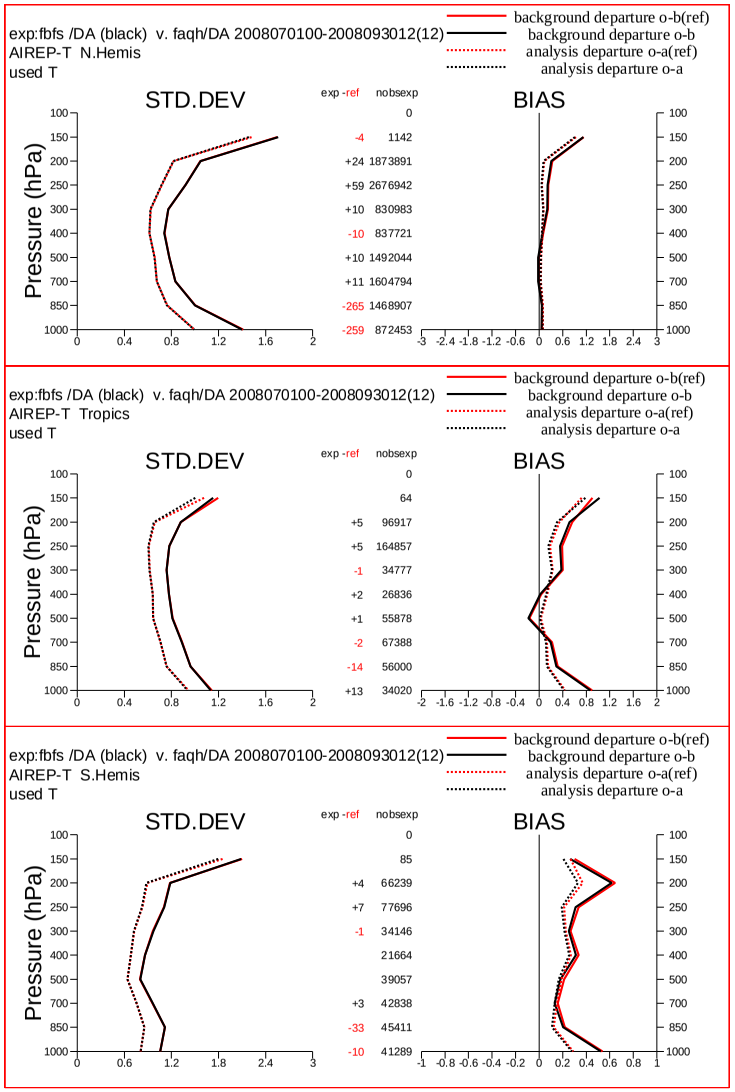

Figure 58: a): Fit between model first-guess (solid) and analysis (dashed) with radiosonde temperatures in the Northern hemisphere (top), Tropics (middle) and Southern hemisphere (bottom) from GPSRO denial (black) keeping only 67% of RO data and control (red) experiments. Left panels show standard deviations, right panels show biases. Numbers in central column denote the data sample from the denial (right, black) experiment and the difference between denial experiment and control (left, black or red). Statistics were generated from period 01/07-30/09/2008. b): Same as a), but statistics for aircraft temperatures.

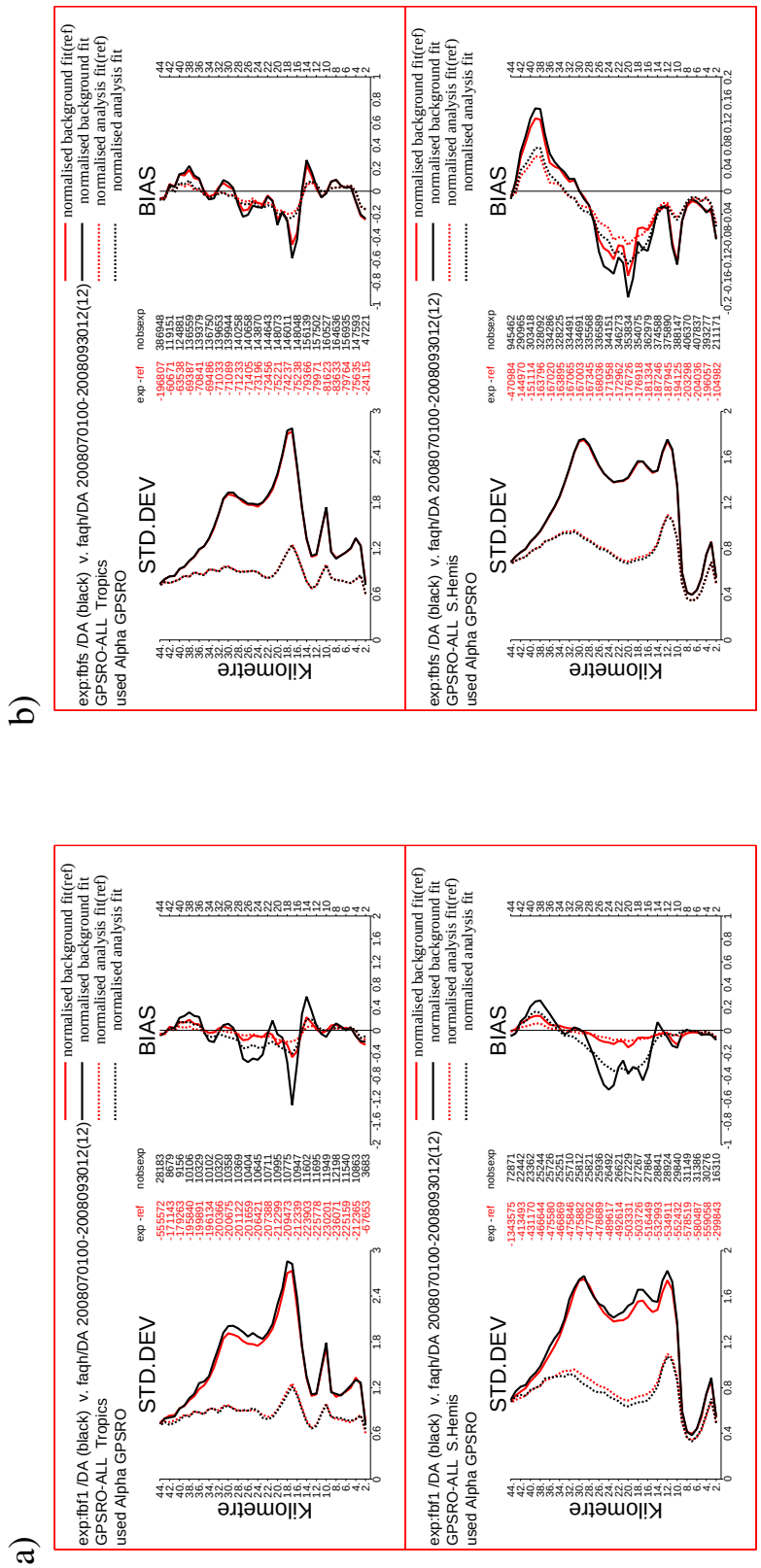

Figure 59: Fit between model first-guess (solid) and analysis (dashed) with GPSRO data in the Tropics (top), and Southern hemisphere (bottom) from GPSRO denial (black) keeping only 5% (a) or 67% (b) of RO data and control (red) experiments. Left panels show standard deviations, right panels show biases. Numbers in central column denote the data sample from the denial (right, black) experiment and the difference between denial experiment and control (left, black or red). Statistics were generated from period 01/07-30/09/2008.

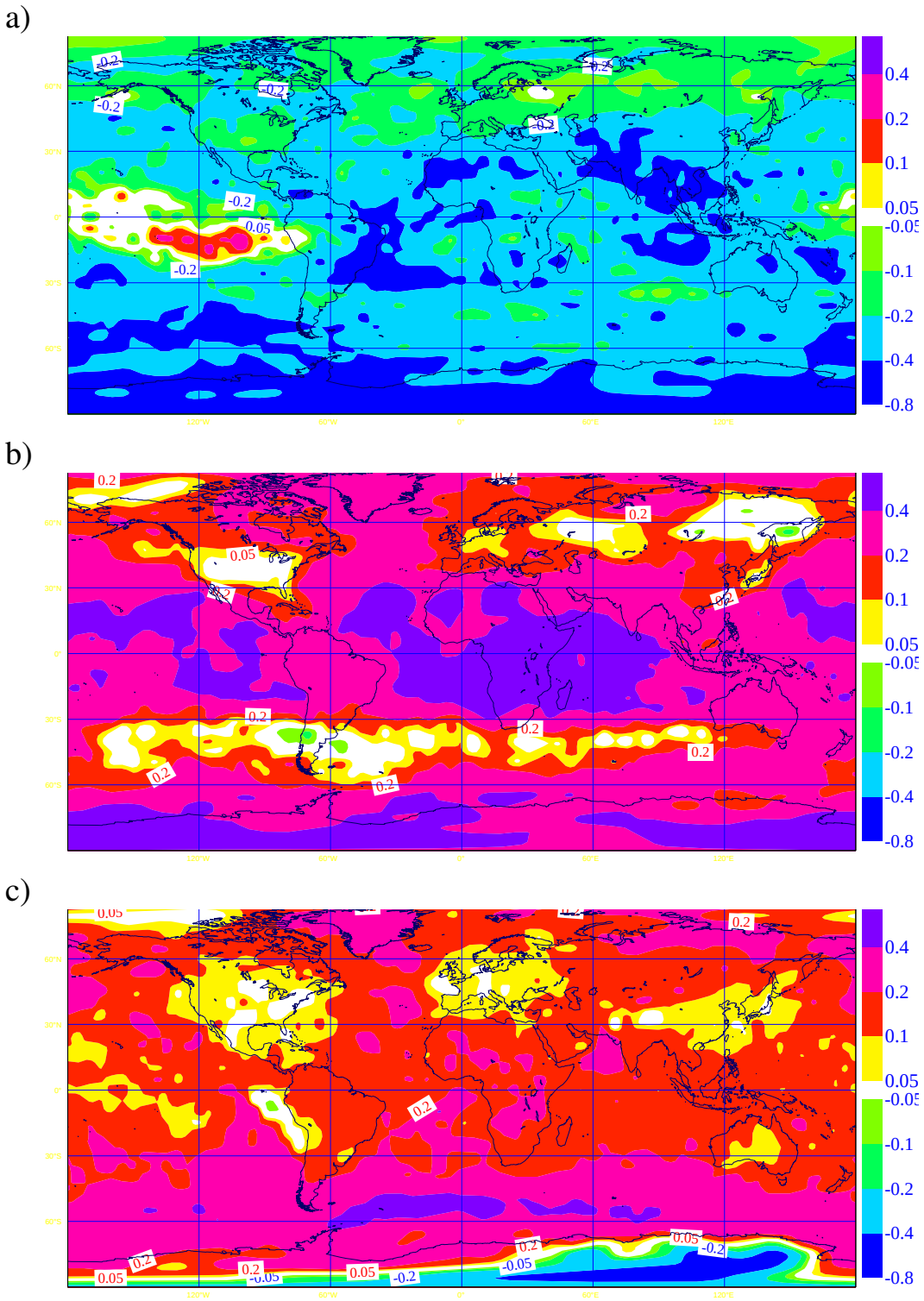

Figure 60: Mean temperature analysis difference between GPSRO denial and control experiments at 20 hPa (a), 200 hPa (b) and 850 hPa (c) levels for the period 01/07-30/09/2008.

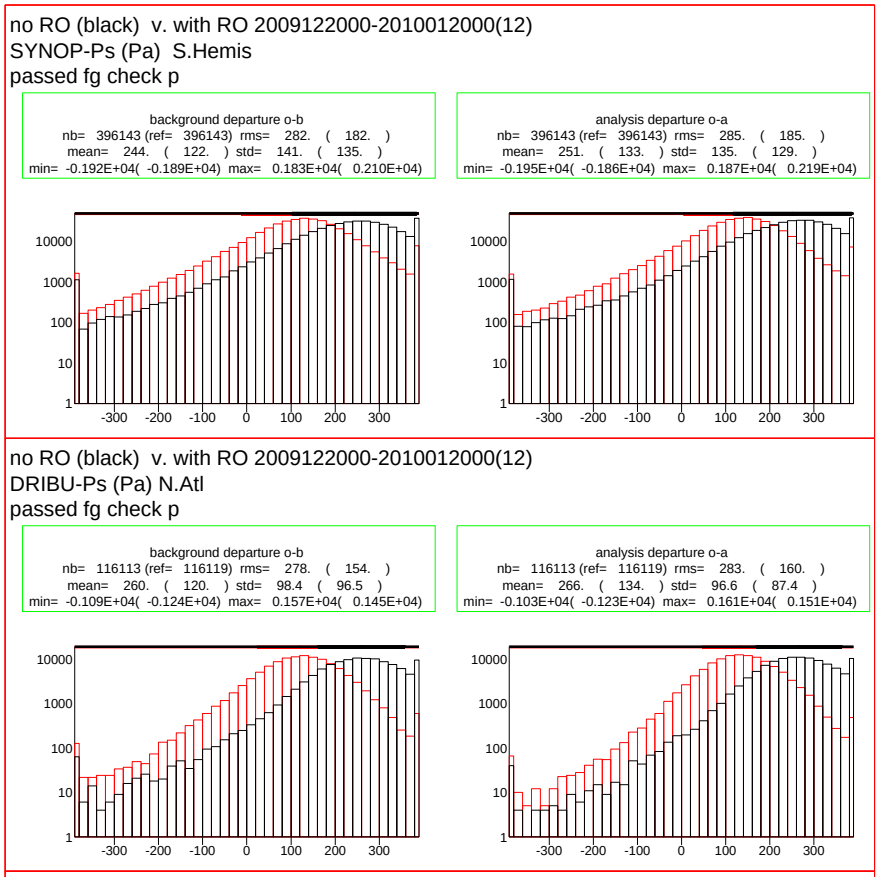

Figure 61: Fit between model first-guess (left) and analysis (right) and independent surface pressure observations in Southern hemisphere SYNOP data (top) and Northern Atlantic buoy observations (bottom). Statistics were generated from period 20/12/2009-20/01/2010 after 2 months of spin-up time to let the model drift away from conventional surface pressure observations.

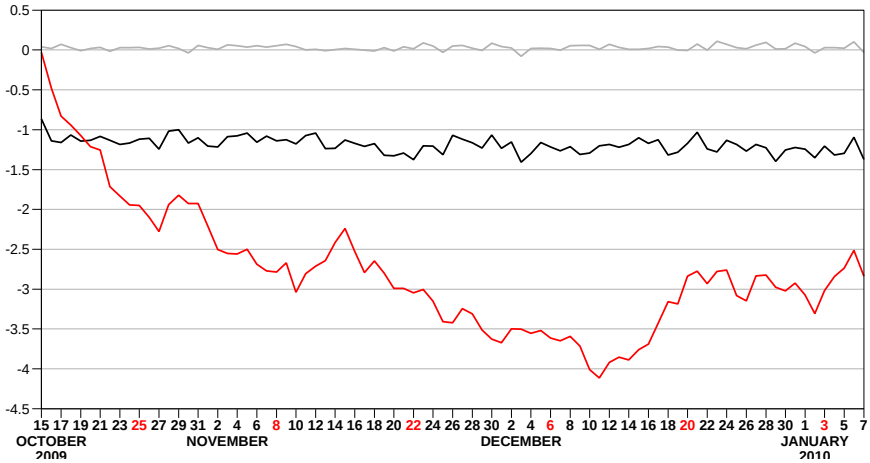

Figure 62: Temporal evolution of surface pressure bias of 12-hour forecasts over the Northern hemisphere verified against operational analysis for three experiments: control using all observations (grey), all conventional surface pressure observations removed (black) and surface pressure and GPSRO observations removed (red). Period of investigation is 15/10/2009-7/1/2010.

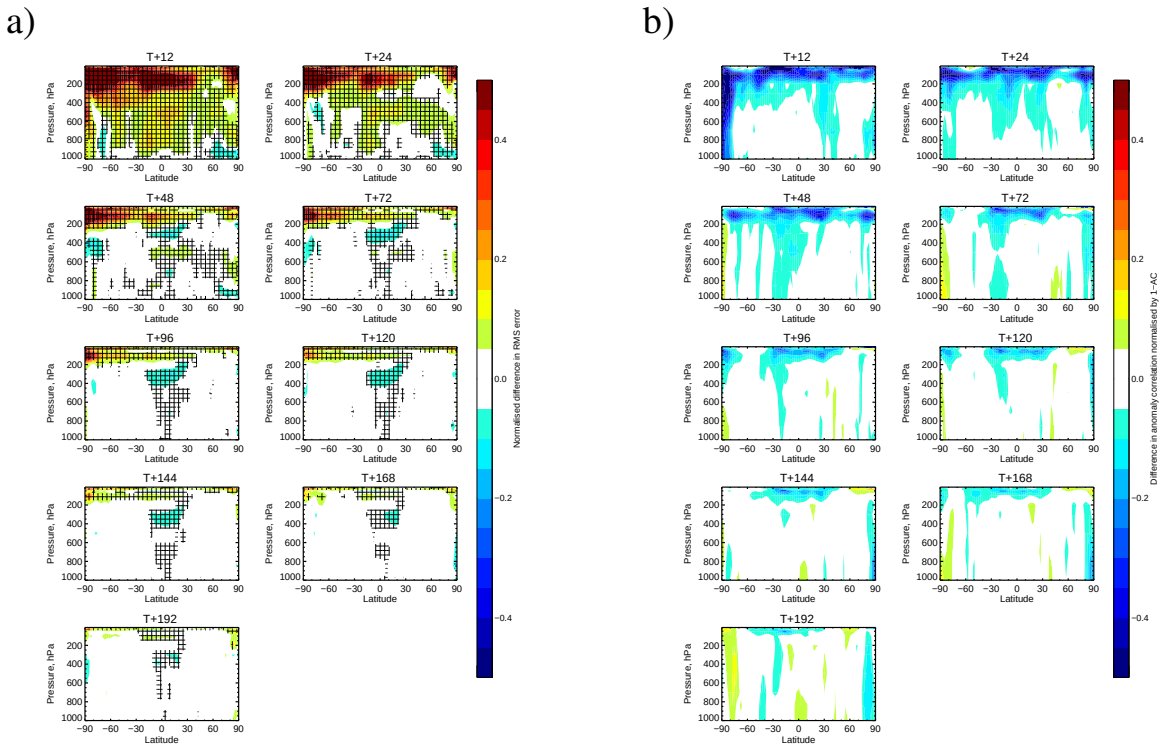

Figure 63: Zonal cross-sections of normalized RMS forecast error difference of temperature (left) and of anomaly correlation difference of geopotential height (right) between GPSRO full denial and control. Positive values for RMS error (a) and negative values for anomaly correlations (b) indicate positive impact of the assimilated GPSRO data. Panels show forecast range of 12, 24, 48, 72, 96, 120, 144, 168 and 192 hours. Crosses indicate where scores are statistically significant at the 95% level. Forecast verification is against operational analysis, verification period is 01/07-30/09/2008.

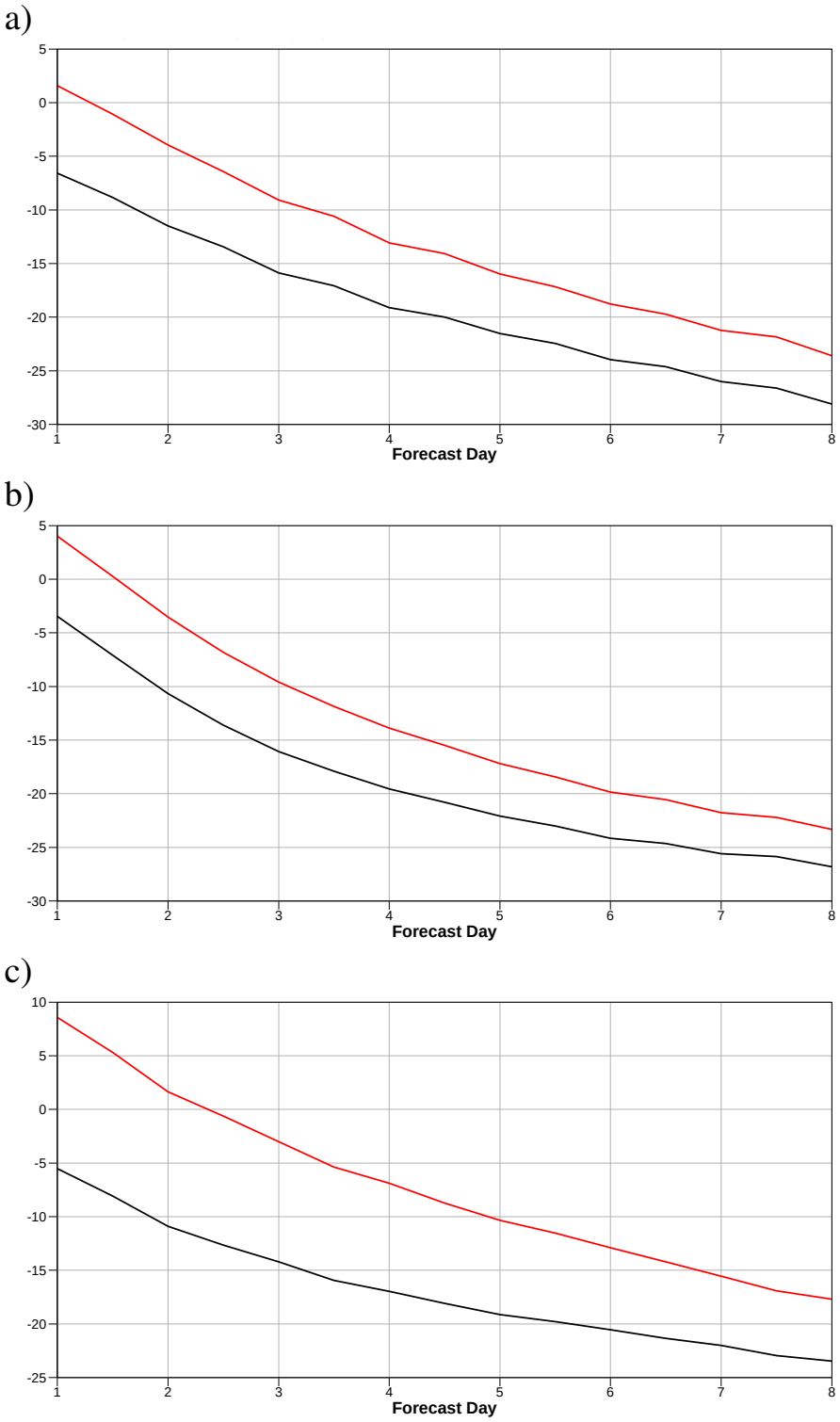

Figure 64: 100 hPa geopotential height forecast bias for the GPSRO full denial (red) and the control (black) experiment. for Northern hemisphere (a), Tropics (b), and Southern hemisphere (c). Forecast verification is against operational analysis, verification period is 01/07-30/09/2008.

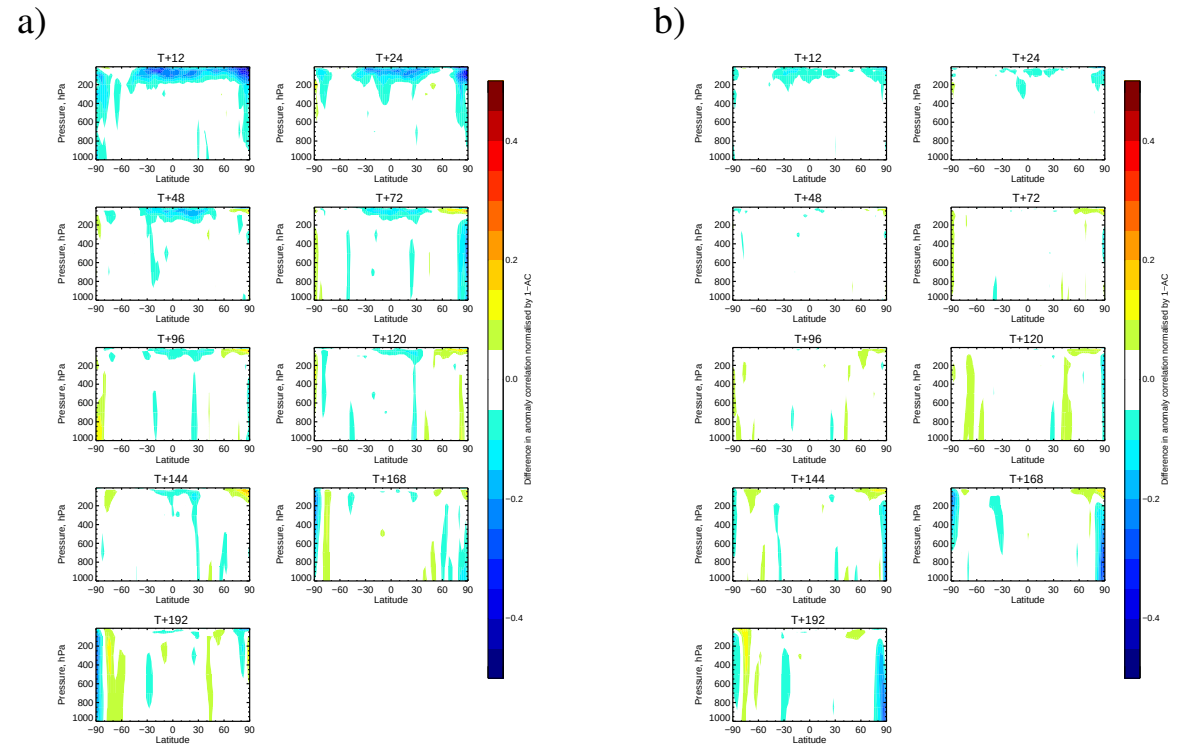

Figure 65: Zonal cross-sections of normalized anomaly correlation difference of geopotential height between 33 % of total GPSRO data and control (a) and GPSRO 67 % of total GPSRO data and control (b). Negative values for anomaly correlation differences indicate positive impact of the assimilated GPSRO data. Panels show forecast range of 12, 24, 48, 72, 96, 120, 144, 168 and 192 hours. Crosses indicate where scores are statistically significant at the 95% level. Forecast verification is against operational analysis, verification period is 01/07-30/09/2008.

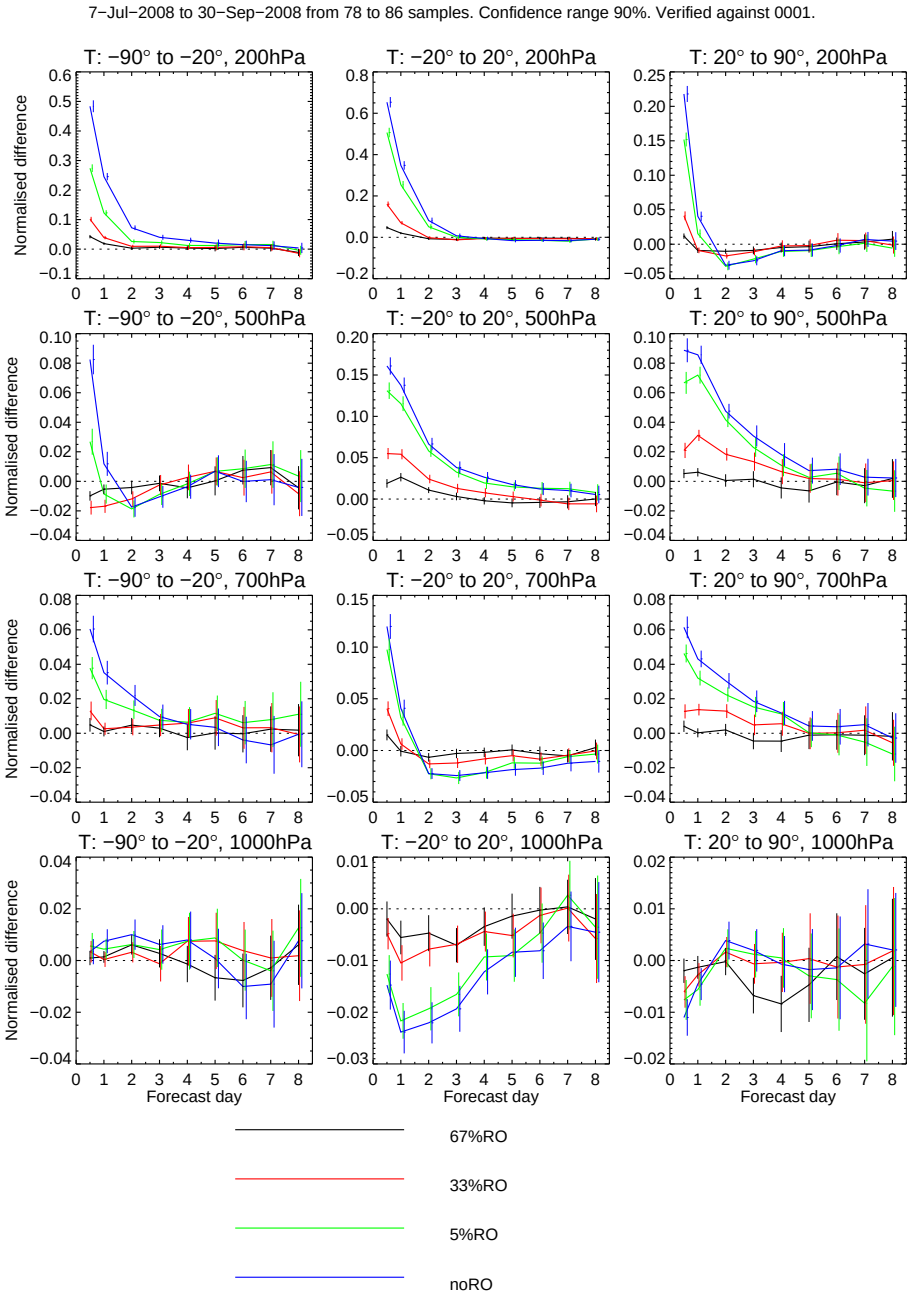

Figure 66: Normalized RMS error difference between GPSRO denial experiments (numbers denote the percentage used) and control for temperature. Positive values indicate positive impact of GPSRO data. Left, middle and right columns refer to Southern hemisphere, Tropics and Northern hemisphere. Rows correspond to 200, 500, 700 and 1000 hPa (from top to bottom). Forecast verification is against operational analysis, verification period is 01/07-30/09/2008.

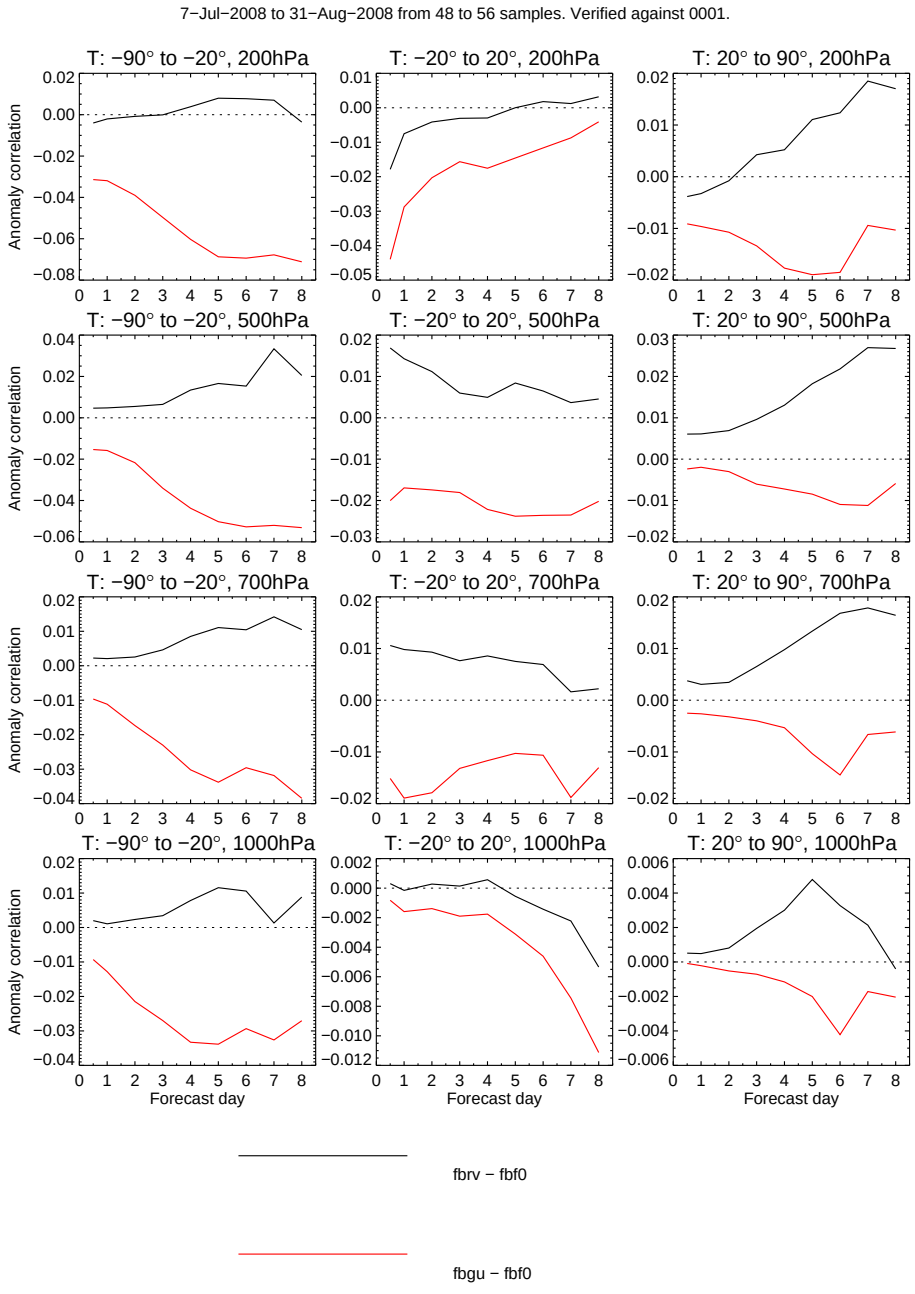

Figure 67: Temperature forecast anomaly correlation difference for Baseline minus Baseline + GPSRO (red) and Baseline + IASI minus Baseline + GPSRO (black). Left, middle and right columns refer to Southern hemisphere, Tropics and Northern hemisphere. Rows correspond to 200, 500, 700 and 1000 hPa (from top to bottom). Forecast verification is against operational analysis, verification period is 7/7/2008-31/8/2008.

5.5 ASCAT soil moisture

An ASCAT soil moisture impact experiment has been run for an entire year over the period 01/12/2008 to 30/11/2009 at a T255 (about 80 km) resolution. Two experiments have been run, both using the recently developed simplified extended Kalman Filter (SEKF) scheme for the point-wise analysis of soil moisture. This scheme has been implemented in November 2010 with the IFS 36r4 and it replaces the previous Optimum Interpolation soil moisture analysis. In the current operational configuration the SEKF is using conventional SYNOP observations of screen level parameters. The replacement of the OI scheme by SEKF itself resulted in drastically reduced soil moisture analysis increments and it helped to reduce the night-time cold bias of 2-metre temperatures in the model as reported in de Rosnay et al. (2009). The SEKF soil moisture analysis opens possibility to assimilate satellite based soil moisture observations, such as those from METOP ASCAT, and to optimally combine them with observed screen-level parameters. The only difference between the two experiments is the usage of ASCAT soil moisture products. In the experiment where ASCAT data is assimilated, soil moisture data have been matched to the model soil moisture using a Cumulative Distribution Function (CDF) as described in Scipal et al. (2008). CDF matching corrects observations bias and variance. In the data assimilation scheme the observed ASCAT soil moisture variability is assimilated. However it is expected that in places where the model has systematic soil moisture errors, like in Sahel for instance where precipitation is underestimated because the West African monsoon does not go far enough to the north, the CDF matching will prevent from using efficiently the ASCAT soil moisture information. In the ASCAT soil moisture experiment, only low incidence angle ASCAT measurements are used (ASCAT nodes between 11 and 26). At higher incidence angles ASCAT soil moisture product is noisier and first guess departures are larger as shown by de Rosnay 2009. The angular dependency and noise level of the ASCAT soil moisture product is related to current issues in the ASCAT-ERS inter-calibration as detailed in a report by the Technical University of Vienna (IPF, 2009). EUMETSAT recently revised the processing of the ASCAT soil moisture product. The revised product, still experimental has no longer angular sensitivity to incidence angle and the noise level of the observation has been drastically reduced. This new product will be implemented in operations by EUMETSAT in early 2011 and it should enable to improve considerably the ASCAT soil moisture data usage, as already presented from experiments conducted with the new product prototype by de Rosnay at the EUMETSAT SAG meeting in 2010 (de Rosnay, 2010). So in the preliminary experiment presented in this report, it is important to notice that the impact of ASCAT data assimilation might be limited by both the quality of the current ASCAT product and the CDF-matching approach used in the assimilation scheme.
Figure 68 shows mean analysis difference maps of 1000 hPa temperature in degrees K (top) and relative humidity in % (bottom) between the experiments with and without ASCAT soil moisture assimilation. The average has been computed from the period June-August 2009. It can be seen that the low level humidity and temperature analysis fields are influenced by the ASCAT soil moisture data over the continental areas. The biggest systematic impact can be found near the Amazon basin, but the African continent and the Northern parts of Asia and North-America also show stronger differences between the mean analysis states.

Figure 69 shows the ASCAT cumulative distribution function (CDF) matching parameters (Scipal et al, 2008) at resolution T799 (about 25 km). The white patches indicate areas where ASCAT soil moisture data is not used due to quality control data rejection (e.g. too high vegetation, snow cover, etc). It can be seen that the Amazon basin is such an area due to dense vegetation. Therefore the largest analysis and forecast differences obtained for this area are surprising and must be a response to the differences in the surrounding areas.

The temperature response of the assimilation system to the change of soil moisture analysis can be more

easily seen in Figure 70, which shows the mean difference of 24-hour forecasts instead of analyses for 1000 hPa temperature and thus the short-range forecast impact of different initializations.

Figure 71 and Figure 72 show the time evolution of normalized RMS forecast error difference between the two experiments for 1000 hPa temperature and humidity, respectively. The error difference patterns are very noisy because, in most areas, the differences are very small and the small random differences are amplified by the normalization. However, some agreement can be identified between the continental areas where large analysis differences were found (Figure 68) and the present maps of forecast score differences.

In the abovementioned areas, i.e. the Amazon basin, northern Asia and Canada, the near surface forecast scores also differ and a positive forecast impact (blue colours) is dominating. On the other hand, when near surface temperature forecasts are verified against radiosonde observations, a small negative impact of the ASCAT soil moisture assimilation can be identified over some continental areas. Figure 73 and Figure 74 show the RMS error and bias of 1000 hPa temperature forecast verified against radiosondes over North-America. Red curves denote the experiment with ASCAT data and it can be seen that both RMS errors and biases are somewhat larger in the ASCAT experiment.

Screen level parameter verifications against SYNOP data have also been performed for the whole period of one year. Figure 75 shows the evolution of 2m temperature and relative humidity 48 hour forecast scores for the two experiments during the entire year of experimentation over North America. No visible differences can be identified in the performance. For other continents and time ranges the situation is similar (not shown here).

De Rosnay et al (2009) have performed additional verification against in situ soil moisture measurements (12 stations in Southern France) for 8 months of the experimentation period. They also found that using the SEKF scheme the assimilation of ASCAT soil moisture data does not have a significant impact on the scores.

This low sensitivity is explained as discussed above by the quality of the current ASCAT soil moisture product, which presents a strong angular sensitivity and a relatively high noise level. In addition the ECMWF CDF-matching approach is a strong constraint that prevents the analysis from using efficiently the information in areas affected by systematic errors. With the revised version of the ASCAT soil moisture product that will come into operations at EUMETSAT in early 2011 and the update of the CDF-matching approach to be conducted at ECMWF in 2011, we expect ASCAT data assimilation to have a more important impact on the surface soil moisture and screen level parameters.

Summary

ASCAT soil moisture impact experiments have been run for an entire year over the period 01/12/2008 to 30/11/2009 at reduced model resolution. The experiments employed the recently developed simplified extended Kalman Filter scheme for the point-wise analysis of soil moisture. Mean low level humidity and temperature analysis fields are affected by the ASCAT soil moisture data over continental areas. The biggest systematic impact can be found near the Amazon basin, but the African continent and the Northern parts of Asia and North-America also show large changes of the mean analysis state.

Forecast scores have been calculated verifying the ASCAT assimilation experiment and its control with the experiments' own analyses. From this, positive forecast impact is derived over most continental areas. If near surface temperature forecasts are verified against radiosonde observations, a small negative impact of the ASCAT soil moisture assimilation can be identified over some continental areas that

needs to be further investigated. Verifications against SYNOP observations and against in situ soil moisture measurements over Southern France show no impact of ASCAT soil moisture data on the forecast scores. Larger impact is expected to be found with the improved quality product that will be released by EUMETSAT in 2011 and the revised CDF-matching approach that will be developed at ECMWF.

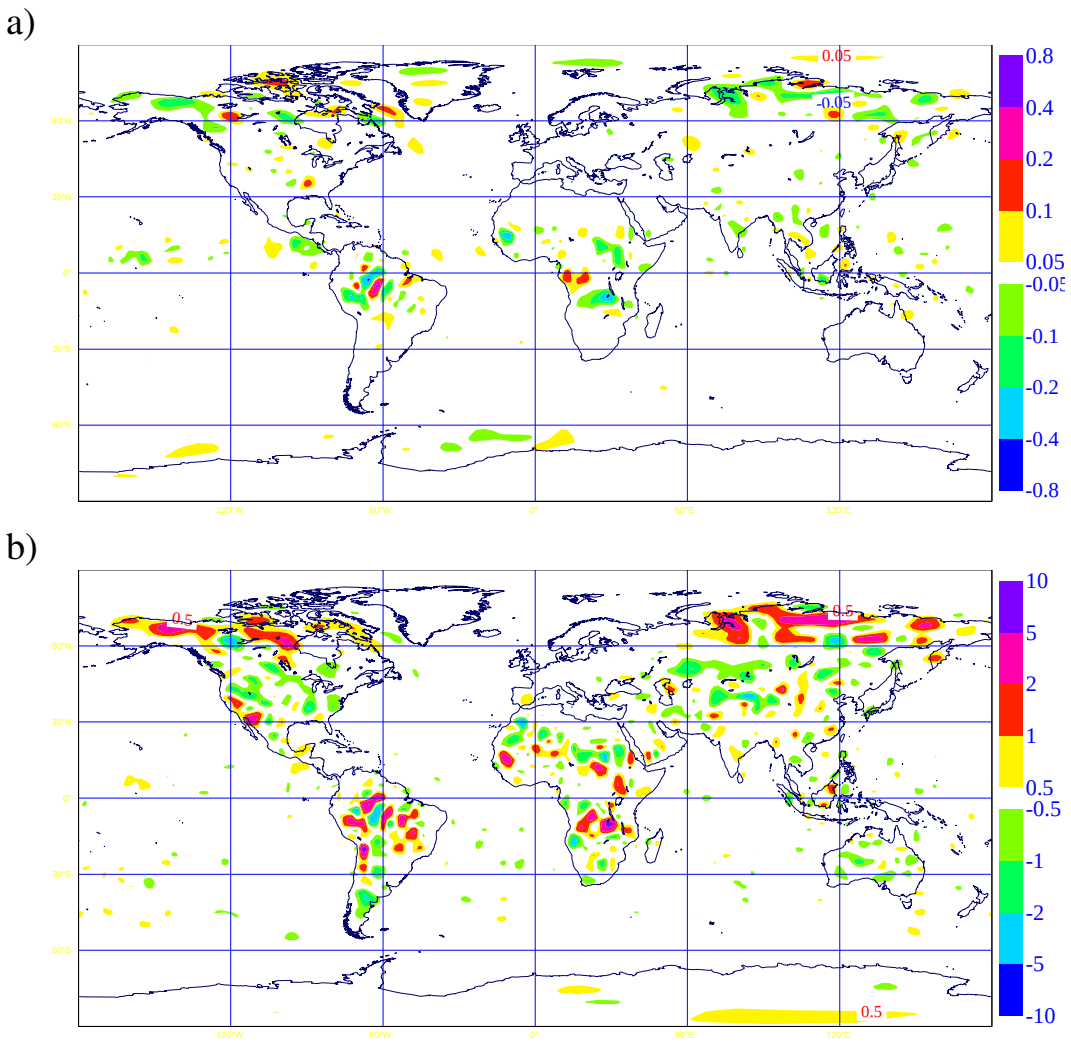

Figure 68: June-August 2009 mean analysis difference maps of 1000 hPa temperature (in K, a) and relative humidity (in %, b) between the experiments with and without ASCAT soil moisture assimilation. Yellow to red colours mean that the experiment with ASCAT soil moisture included is warmer (wetter), green to blue means that it is colder (drier).

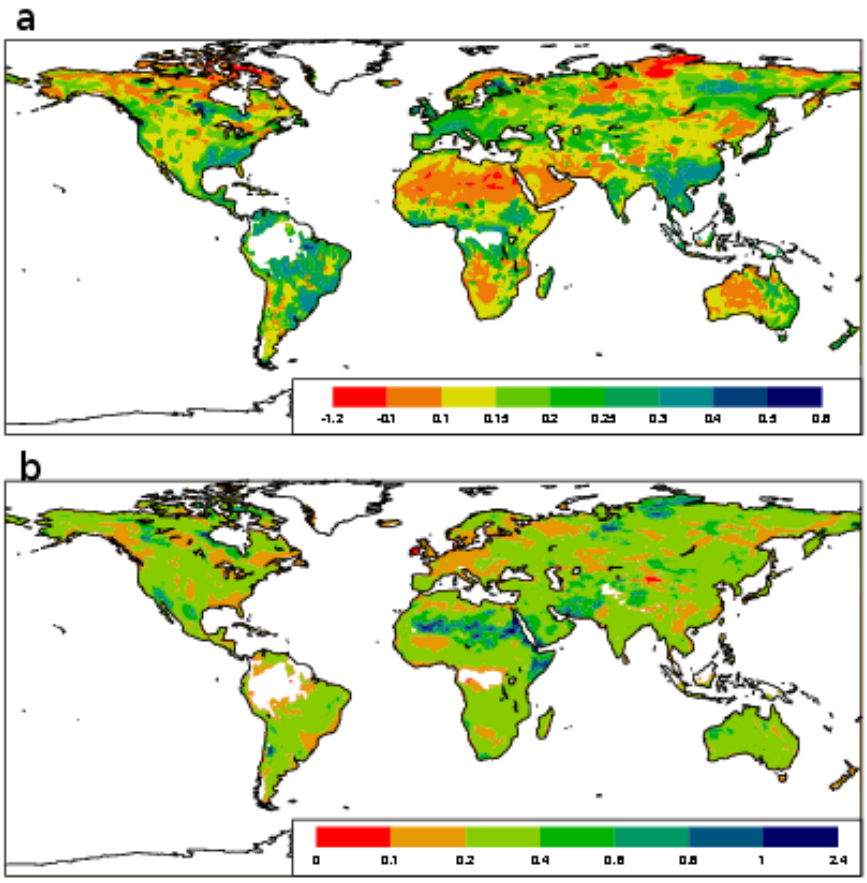

Figure 69: ASCAT CDF matching parameters at resolution T799. The parameter a (top) and b (bottom) are expressed in m^3/m^3.

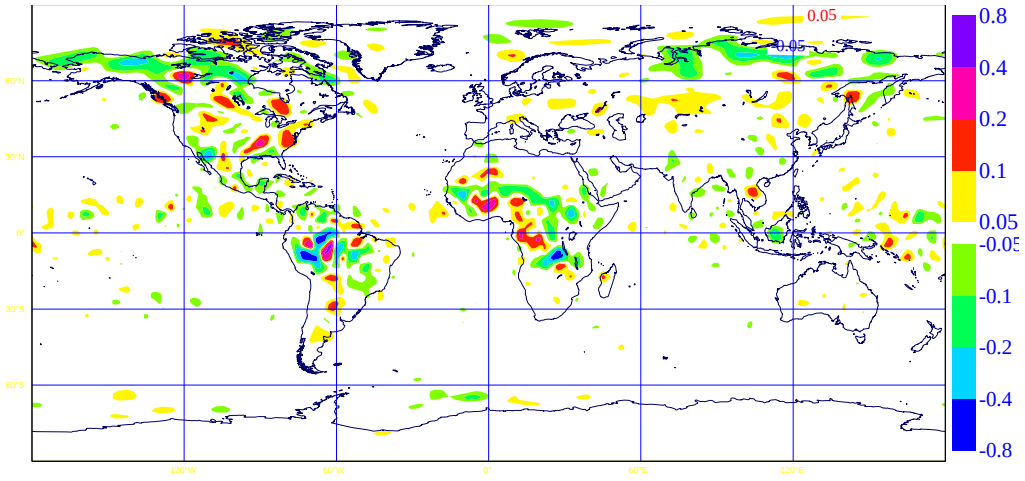

Figure 70: As Figure 68 for mean 24-hour temperature forecast difference.

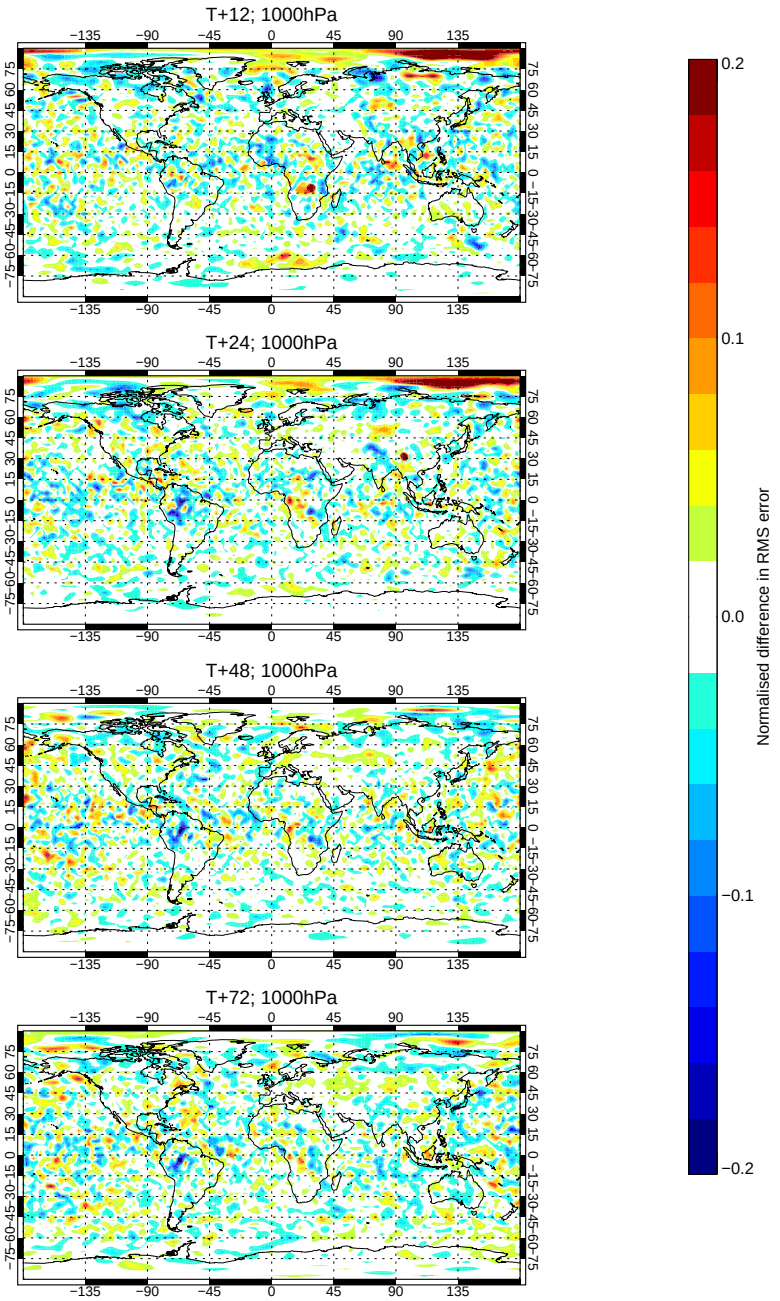

Figure 71: Normalized RMS forecast error difference between experiments with and without ASCAT soil moisture assimilation for 1000 hPa temperature. Negative values indicate positive impact of the assimilated ASCAT data. Panels show forecast range of 12, 24, 48 and 72 hours (from top to bottom). Forecast verification is against operational analysis, verification period is 01/06/2009-30/08/2009.

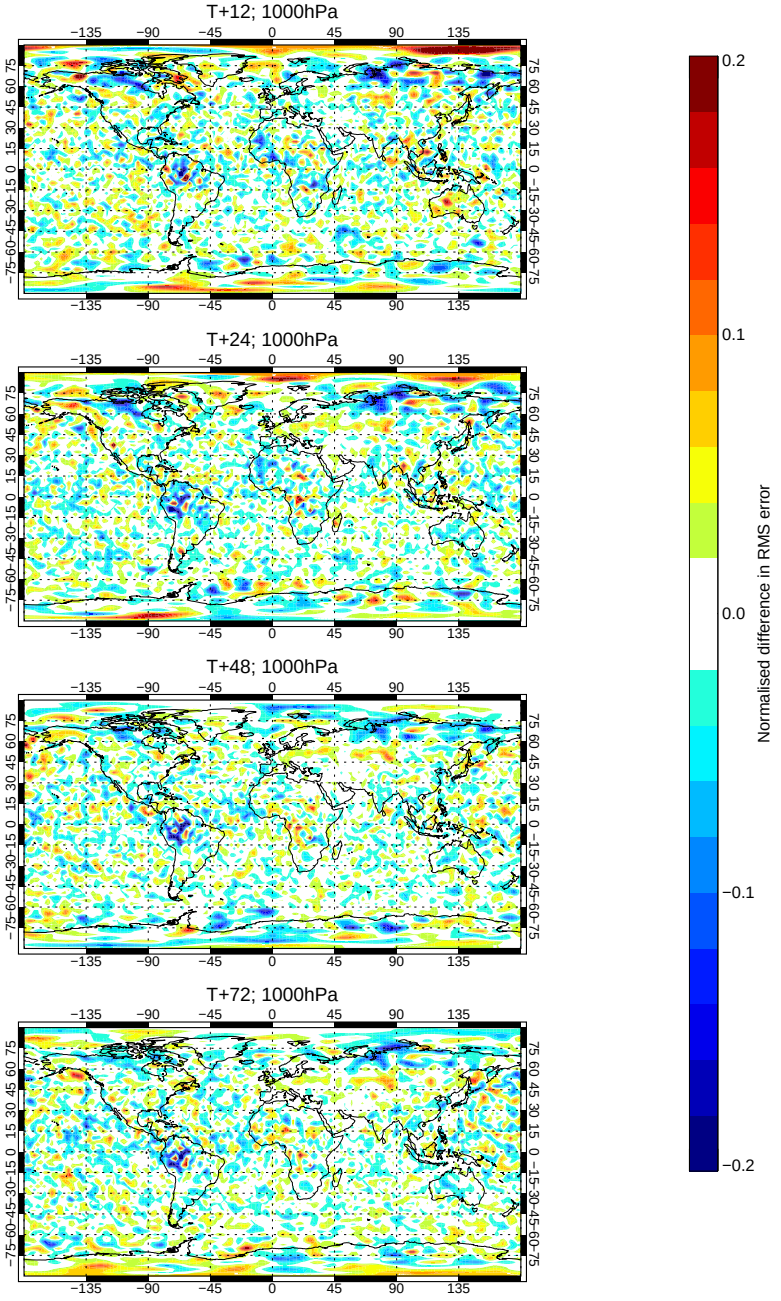

Figure 72: As Figure 71 for relative humidity at 1000 hPa.

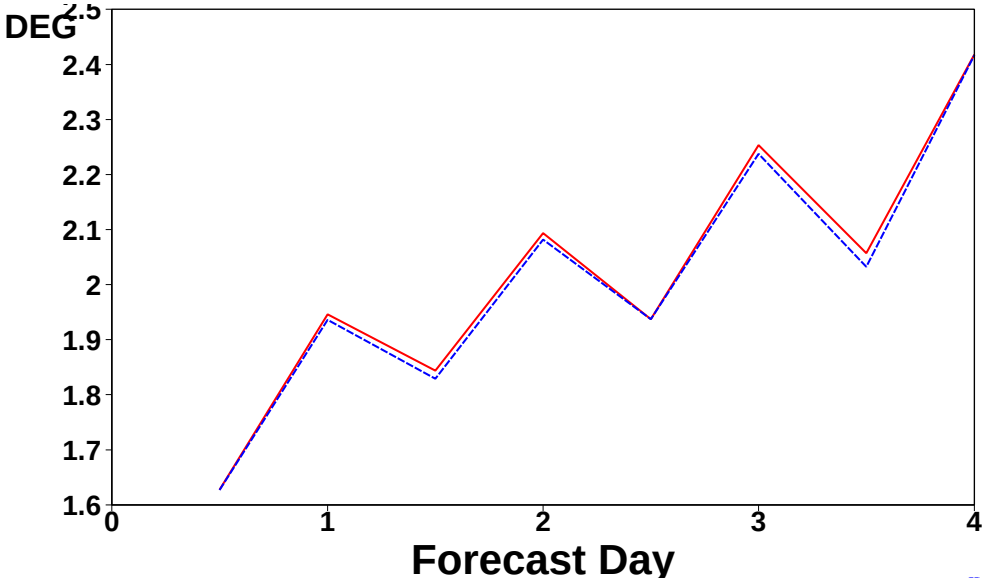

Figure 73: 1000 hPa temperature RMS forecast error for experiments with (red) and without (blue) ASCAT soil moisture assimilation. Forecast scores are computed against radiosonde observations over North America, verification period is 01/06/2009-30/08/2009.

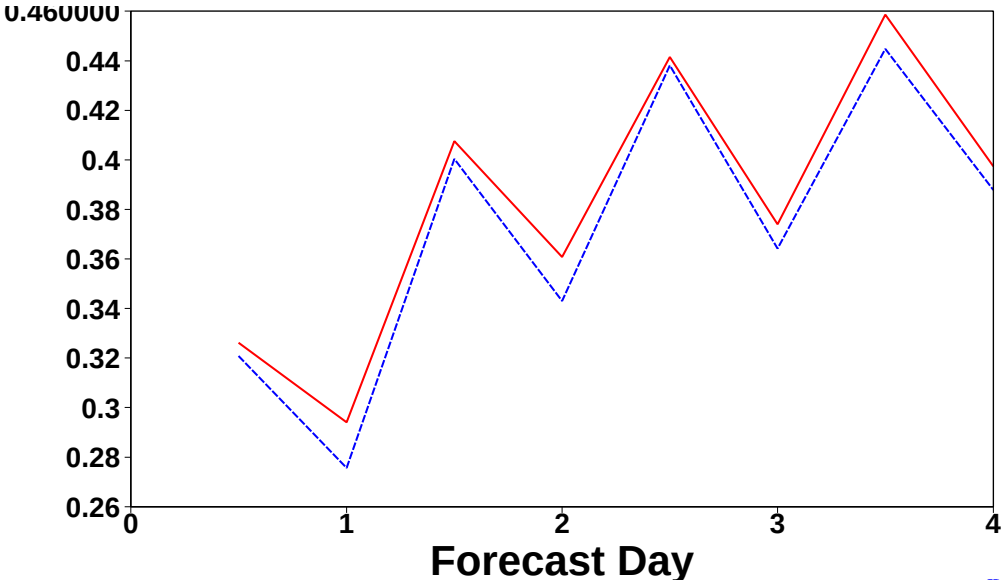

Figure 74: As Figure 73 for 1000 hPa temperature biases.

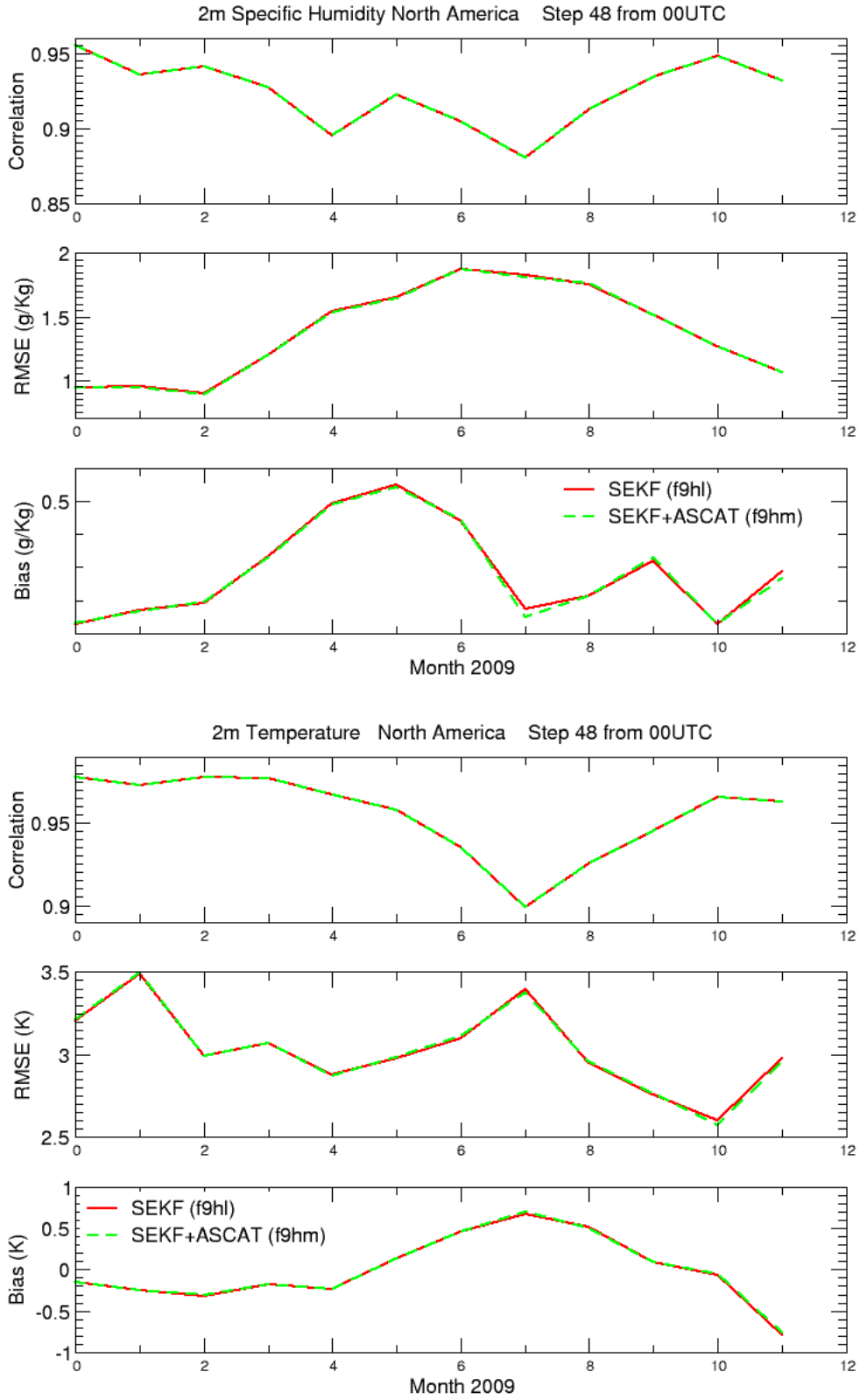

Figure 75: 12 month time evolution of 48 hour forecast scores for 2m specific humidity (top three blocks) and for 2m temperature (bottom three blocks). Verification has been performed against SYNOP measurements over North-America. Both panels show scores in terms of correlation (top), root-mean-square error (middle) and bias (bottom). Green curves belong to the experiment with and red without ASCAT soil moisture data.

6 Appendix: Analysis and forecast observational influence

6.1 Linear statistical estimation in NWP

Data assimilation systems for NWP provide estimates of the atmospheric state $\mathbf{x}$ by combining meteorological observations $\mathbf{y}$ with prior (or background) information $\mathbf{x}_b$. A simple Bayesian Normal model provides the solution as the posterior expectation for $\mathbf{x}$ given $\mathbf{y}$ and $\mathbf{x}_b$. The same solution can be achieved from a classical frequentist approach, based on a statistical linear analysis scheme providing the Best Linear Unbiased Estimate (BLUE; Talagrand, 1997) of $\mathbf{x}$ given $\mathbf{y}$ and $\mathbf{x}_b$. The optimal generalized least-squares (GLS) solution of the analysis problem (see Lorenc, 1986) can be written as:

$$\mathbf{x}_a = \mathbf{K}\mathbf{y} + (\mathbf{I}_n - \mathbf{K}\mathbf{H})\mathbf{x}_b \tag{1}$$

The vector $\mathbf{x}_b$ is the 'analysis'. The gain matrix $\mathbf{K}$ (nxp) takes into account the respective uncertainties of the background vector $\mathbf{x}_b$ and the observation vector $\mathbf{y}$ as defined by the (nxn) error covariance matrix $\mathbf{B}$ and the (pxp) error covariance matrix $\mathbf{R}$, with:

$$\mathbf{K} = (\mathbf{B}^{-1} + (\mathbf{H}^T\mathbf{R}^{-1}\mathbf{H})^{-1}\mathbf{H}^T\mathbf{R} \tag{2}$$

Here, $\mathbf{H}$ (pxn) is a matrix interpolating the background fields to the observation locations, and transforming the model variables to observed quantities (e.g. radiative transfer calculations transforming the model temperature, humidity etc. into brightness temperatures as observed by satellite radiometers). In the 4D-Var context introduced below, $\mathbf{H}$ is defined to include also the propagation in time of the atmospheric state vector to the observation times using a forecast model.

Substituting Eq. 2 into Eq. 1 and projecting the analysis estimate onto the observation space, the estimate becomes:

$$\hat{\mathbf{y}} = \mathbf{H}\mathbf{x}_a = \mathbf{H}\mathbf{K}\mathbf{y} + (\mathbf{I}_p - \mathbf{H}\mathbf{K})\mathbf{H}\mathbf{x}_b \tag{3}$$

It can be seen that the analysis state in observation space ($\mathbf{H}\mathbf{x}_b$) is defined as the sum of the background (in observation space, $\mathbf{H}\mathbf{x}_b$) and the observations $\mathbf{y}$, weighted by the pxp square matrices **I-HK** and **HK**, respectively. In this case, for each unknown component of $\mathbf{H}\mathbf{x}$, there are two data values: a real and a 'pseudo' observation. The additional term in (2.3) includes these pseudo-observations, representing prior knowledge provided by the observation-space background $\mathbf{H}\mathbf{x}_b$).

6.2 Analysis sensitivity to observations, OIA

The analysis sensitivity with respect to the observations is obtained (Cardinali et al. 2004) from:

$$\mathbf{S} = \frac{\partial \hat{\mathbf{y}}}{\partial \mathbf{y}} = \mathbf{K}^T\mathbf{H}^T \tag{4}$$

Similarly, the analysis sensitivity with respect to the background (in observation space) is given by:

$$\frac{\partial \hat{\mathbf{y}}}{\partial(\mathbf{H}\mathbf{x}_b)} = \mathbf{I} - \mathbf{K}^T\mathbf{H}^T = \mathbf{I}_p - \mathbf{S} \tag{5}$$

Here, the (projected) background influence is complementary to the observation influence. For example, if the self-sensitivity with respect to the i-th observation is S_{ii}, the sensitivity with respect the background projected at the same variable, location and time will be simply $1 - S_{ii}$. In particular, the observation

influence $S_{ii} \in [0,1]$ where $S_{ii} = 0$ means that the i-th observation has had no influence at all in the analysis (only the background counted) and $S_{ii} = 1$ indicates that an entire degree of freedom has been devoted to fit that data point (the background has had no influence). The $tr(\mathbf{S})$ can be interpreted as a measure of the amount of information extracted from the observation or 'degree of freedom for signal' (DFS) whilst it follows that the complementary trace is $tr(\mathbf{I}-\mathbf{S}) = p - tr(\mathbf{S})$ This is the DFS from the background that is the weight given to prior information and is to be compared to the observational weight $tr(\mathbf{S})$.

Inserting Eq. 2 into Eq. 4, we obtain:

$$\mathbf{S} = \mathbf{R}^{-1}\mathbf{H}(\mathbf{B}^{-1} + \mathbf{H}^T\mathbf{R}^{-1}\mathbf{H})^{-1}\mathbf{H}^T \tag{6}$$

As $(\mathbf{B}^{-1} + \mathbf{H}^T\mathbf{R}-1\mathbf{H})^{-1}$ is equal to the analysis error covariance matrix $\mathbf{B}^{-1}$.

6.3 Forecast error contribution of observations, FEC

Baker and Daley (2000) derived the forecast sensitivity equation with respect to the observations in the context of variational data assimilation. If we consider a scalar J-function that is the forecast error. Then, the sensitivity of J with respect to the observations can be written using a simple derivative chain as:

$$\frac{\partial J}{\partial \mathbf{y}} = \frac{\partial J}{\partial \mathbf{x}_a}\frac{\partial \mathbf{x}_a}{\partial \mathbf{y}} \tag{7}$$

$\partial J/\partial \mathbf{x}_a$ is the sensitivity of forecast error to the initial condition $\mathbf{x}_a$ (Rabier et al. 1996, Gelaro et al., 1998). From (2.1) the sensitivity of the analysis system with respect to the observations and the background can be derived from:

$$\frac{\partial \mathbf{x}_a}{\partial \mathbf{y}} = \mathbf{K}^T, \frac{\partial \mathbf{x}_a}{\partial \mathbf{x}_b} = \mathbf{I} - \mathbf{H}^T\mathbf{K}^T \tag{8}$$

By using Eq. 8 and Eq. 2 the forecast sensitivity to the observations becomes:

$$\frac{\partial J}{\partial \mathbf{y}} = \mathbf{K}^T\frac{\partial J}{\partial \mathbf{x}_a} = \mathbf{R}^{-1}\mathbf{H}(\mathbf{B}^{-1} + \mathbf{H}^T\mathbf{R}^{-1}\mathbf{H})^{-1}\frac{\partial J}{\partial \mathbf{x}_a} \tag{9}$$

A second order sensitivity gradient needs to be known in Eq. 16 because only orders above the first contain the information related to the forecast error. In fact, the first order only contains information on the sub-optimality of the assimilation system (Cardinali 2009). To compute the second order sensitivity gradient, two forecasts of length f starting from $\mathbf{x}_a$ and length g starting from $\mathbf{x}_b$ have to be produced. Both forecasts verify at time t. Following Langland and Baker (2004) and Errico (2007) the second order sensitivity gradient is then defined as:

$$\frac{\partial J}{\partial \mathbf{x}_a} = \frac{\partial J_f}{\partial \mathbf{x}_a} + \frac{\partial J_g}{\partial \mathbf{x}_b} \tag{10}$$

where J_f and J_g are a quadratic measure of the two forecast errors (x_t the verifying analysis, taken here as the truth). It is clear from (3.4) that the adjoint model maps the sensitivity (with respect to the forecast) of J_f along the trajectory f and the sensitivity of J_g along the trajectory g.

Once the forecast sensitivity is computed (see Cardinali 2009 for details), the variation δJ of the forecast error expressed by J can be found by rearranging Eq. 7 and by using the adjoint property for the linear

operator:

$$\delta J = \langle \frac{\partial J}{\partial \mathbf{x}_a}, \mathbf{x}_a \rangle \quad (11)$$

$$= \langle \frac{\partial J}{\partial \mathbf{x}_a}, \mathbf{K}(\mathbf{y} - \mathbf{H}\mathbf{x}_b) \rangle \quad (12)$$

$$= \langle \mathbf{K}^T \frac{\partial J}{\partial \mathbf{x}_a}, \mathbf{y} - \mathbf{H}\mathbf{x}_b \rangle \quad (13)$$

$$= \langle \mathbf{K}^T \frac{\partial J}{\partial \mathbf{x}_a}, \delta\mathbf{y} \rangle \quad (14)$$

$$= \langle \frac{\partial J}{\partial \mathbf{y}}, \delta\mathbf{y} \rangle \quad (15)$$

where $\delta\mathbf{x}_a = \mathbf{x}_a - \mathbf{x}_b$ are the analysis increments and $\delta\mathbf{y} = \mathbf{y} - \mathbf{H}\mathbf{x}_b$ is the innovation vector. The sensitivity gradient $\partial J/\partial \mathbf{x}_a$ is valid at the starting time of the 4D-Var window (typically 09 and 21 UTC for the 12h 4D-Var set-up used at ECMWF). As for $\mathbf{K}$, its adjoint $\mathbf{K}^T$ incorporates the temporal dimension, and the $\delta\mathbf{y}$ innovations are distributed over the 12-hour window. The variation of the forecast error due to a specific measurement can be summed up over time and space in different subsets to compute the average contribution of different component of the observing system to the forecast error. For example, the contribution of all AMSU-A satellite instrument observations, N, channels, S, over time T will be:

$$\delta J^{AMSU-A} = \sum_{n=1}^{N} \sum_{s=1}^{S} \sum_{t=1}^{T} \delta J_{n,s,t}^{AMSU-A} \quad (16)$$

The forecast error contribution can be gathered over different subsets that can represent a specific observation type, a specific vertical or horizontal domain, or a particular meteorological variable.

7 Acknowledgements

Present study has been funded by EUMETSAT (Project Reference EUM/CO/07/4600000454/PS). The authors wish to thank Rosemary Munro, Jean-Noël Thépaut and Lars Isaksen for comments and many discussions throughout the study. In this report the results of the GPSRO study funded by EUMETSAT GRAS SAF have been used. The GPSRO impact studies have been carried out using the RO data reprocessed by UCAR. We wish to thank UCAR for providing us with the dataset.

8 List of figures and tables

List of Figures

List of Tables

9 References

Baker, N. L. and R. Daley, 2000: Observation and background adjoint sensitivity in the adaptive observation targeting problem. *Q. J. Roy. Meteor. Soc.*, **126**, 1431-1454.

Bauer, P., P. Lopez, A. Benedetti, D. Salmond, and E. Moreau, 2006a: Implementation of 1D+4D-Var

assimilation of precipitation affected microwave radiances at ECMWF, Part I: 1D-Var. *Q. J. Roy. Meteor. Soc.*, **132**, 2277-2306.

Bauer, P., P. Lopez, A. Benedetti, D. Salmond, S. Saarinen and M. Bonazzola, 2006b: Implementation of 1D+4D-Var assimilation of precipitation affected microwave radiances at ECMWF, Part II: 4D-Var. *Q. J. Roy. Meteor. Soc.*, **132**, 2307-2332.

Bauer, P. and G. Radnóti, 2009: Study on Observing System Experiments (OSEs) for the evaluation of degraded EPS/Post-EPS instrument scenarios. Report available from ECMWF, Reading, UK, 99pp.

Bauer, P., 2009: 4D-Var assimilation of MERIS total column water vapour retrievals over land. *Q. J. Roy. Meteor. Soc.*, **135**, 1852-1862.

Bauer, P., A. Geer, P. Lopez and D. Salmond, 2010: Direct 4D-Var assimilation of all-sky radiances. Part I: Implementation. *Q. J. Roy. Meteorol. Soc.*, accepted.

Geer, A., P. Bauer, P. Lopez and D. Salmond, 2010: Direct 4D-Var assimilation of all-sky radiances. Part II: Assessment. *Q. J. Roy. Meteorol. Soc.*, accepted.

Cardinali, C., S. Pezzulli, and E. Andersson, 2004: Influence-matrix diagnostic of a data assimilation system. *Q. J. Roy. Meteor. Soc.*, **130**, 2767-2786.

Cardinali, C., 2009: Monitoring the observation impact on the short-range forecast. *Q. J. Roy. Meteor. Soc.*, **135**, 239-250.

Collard, A.D. and A.P. McNally, 2009a: Monitoring and assimilation of IASI radiances at ECMWF. Tech. Proc. Sixteenth International TOVS Study Conference, Angra dos Reis, Brazil. 7-13 May 2008. Available from http://cimss.ssec.wisc.edu/itwg/itsc/.

Collard, A.D. and A.P. McNally, 2009b: The assimilation of Infrared Atmospheric Sounding Interferometer radiances at ECMWF. *Q. J. Roy. Meteor. Soc.*, DOI: 10.1002/qj.410.

Dee, D.P., 2005: Bias and data assimilation, *Q. J. Roy. Meteor. Soc.*, **131**, 3323-3343.

de Rosnay P., Drusch M., Balsamo G., Beljaars A., Isaksen L., Vasiljevic D., Albergel C., Scipal K., 2009: Advances in land data assimilation at ECMWF. ECMWF/GLASS workshop proceedings, http://www.ecmwf.int/publications/library/do/references/list/200911 9-12 November 2009, ECMWF, 8pp.

de Rosnay, 2009: Sensitivity of ASCAT soil moisture first guess departure to incidence angle. ECMWF research memorandum R48.3/PR/0953, http://www.ecmwf.int/research/EUMETSAT_projects/SAF/HSAF/ecmwf-hsaf/files/derosnay_ecmwf_resememo0953_2009.pdf

de Rosnay, 2010: http://www.ecmwf.int/research/EUMETSAT_projects/SAF/HSAF/ecmwf-hsaf/files/derosnay_ECWMF_ASCAT_SAG_Oct_2010.pdf.

Errico, R., 2007: Interpretation of an adjoint-derived observational impact measure. *Tellus*, **59A**, 273-276

Geer, A.J., P. Bauer and P. Lopez, 2008: Lessons learnt from the operational 1D+4D-Var assimilation of rain- and cloud-affected SSM/I observations at ECMWF. *Q. J. Roy. Meteor. Soc.*,**134**, 1513-1525.

Haseler, J., 2004: The early-delivery suite. ECMWF Technical Memorandum, No. 454, 35 pp. Available from European Centre for Medium-Range Weather Forecasts, Shinfield Park, Reading RG2 9AX, United Kingdom.

IPF, 2009: ERS-ASCAT Backscatter and soil moisture Intercomparison first results. Technical report, http://www.ipf.tuwien.ac.at/radar/ascat_ers_intercomparison.pdf, June 2009.

Kelly, G. and J.-N. Thépaut, 2007: Evalkuation of the impact of the space component of the Global Observing System through Observing System Experiments. *ECMWF Newsletter*, No. 113, 16-28.

Kelly, G., P. Bauer, A.J. Geer, P. Lopez, and J.-N. Thépaut, 2007: Impact of SSM/I observations related to moisture, clouds and precipitation on global NWP forecast skill. *Mon. Wea. Rev.*, **136**, 2713-2726.

McNally, A.P., 2002: A note on the occurrence of cloud in meteorologically sensitive areas and the implications for advanced infrared sounders. *Q. J. Roy. Meteorol Soc.*, **128**, 2551-2556. A. P. McNally

Langland, R. and N.L. Baker, 2004: Estimation of observation impact using the NRL atmospheric variational data assimilation adjoint system. *Tellus*, **56A**, 189-201

McNally, A.P., P.D. Watts, J.A. Smith, R.Engelen, G. Kelly, J.-N. Thépaut and M. Matricardi 2006, The assimilation of AIRS radiance data at ECMWF *Q. J. Roy. Meteorol Soc.*, **132**, 935-957.

McNally, A.P, 2009: The direct assimilation of cloud-affected satellite infrared radiances in the ECMWF 4D-Var.*Q. J. Roy. Meteor. Soc.*, accepted.

Peubey, C. and A.P. McNally, 2009: Characterization of the impact of geostationary clear-sky radiances on wind analyses in a 4D-Var context.*Q. J. Roy. Meteor. Soc.*, submitted.

Scipal, K., M. Drusch, and W. Wagner, 2008: Assimilation of a ERS scatterometer derived soil moisture index in the ECMWF numerical weather prediction system. *Adv. Water Res.*, doi:10.1016/j.advwatres.2008.04013.

WMO, 2008: Evolution of the global observing system. Final report by commission for basic systems OPAG on integrated observing systems. Fourth Session Geneva, Switzerland, 7-11 July 2008. Available from http://www.wmo.int/pages/prog/www/CBS-Reports/IOS-index.html.